2016

The effect of time on soil development: study of a soil chronosequence from Reunion Island, Indian Ocean

Alex Hannan-Joyner

The effect of time on soil development: study of a soil chronosequence from Reunion Island, Indian Ocean

Abstract

Here, presented for the first time, are the results of a geochemical analysis on a soil chronosequence from Reunion Island, Indian Ocean. The soils are defined by three profiles of ages 20 ka, 70 ka and 2 Ma, but all have evolved from the same basaltic parent material, climate, biota and topography, and so form a chronosequence. Using X-Ray Diffraction (XRD), we observe the rapid depletion of the major rock forming minerals – olivine, pyroxene, plagioclase – during the first 70 ka of soil formation. Conversely, there is rapid formation of secondary minerals over the same period, here defined as gibbsite, halloysite and goethite. Interestingly, halloysite, rather than gibbsite, is the dominant phase in the 2 Ma profile, and suggests Si is being conserved at the expense of Al. Additionally, Quadrupole Inductively Coupled Plasma Mass-Spectrometry (Q-ICP-MS) has enabled the concentrations of 19 elements to be measured with remarkable precision. By computing mass-transfer coefficients, identifying elements that are depleted and enriched throughout the profile can be achieved. At Reunion Island, niobium (Nb) is chosen as the index element for these mass-transfer calculations because it shows the greatest immobility. The alkali and alkaline earths are rapidly lost at the surface during the first 20 ka, mainly as a result of plagioclase dissolution. By 70 ka, however, the elements are gained at the surface, and suggests that marine aerosol and dust are able to contribute to the soil nutrient budget. The extent of these gains increases with increasing ionic radius (or equivalently, with decreasing hydration energy), and hypothesize that the fixation ability of clays, which increases with decreasing hydration energy, is responsible for the progressive enrichment of Mg (least) to Cs (most). After 2 Ma, the elements approach 100% depletion, except for Cs and Ba, and is assumed that these elements become immobile once adsorbed onto the surfaces of clays. It is our understanding this is the first time this has been observed in-situ. Meanwhile, the rare earth elements (REE), Mn, and Cu become progressively depleted with soil age, and hypothesise this is due to declining pH and Eh, both with decreasing depth in the soil profiles and over time across the chronosequence. Uranium and Th remain immobile, but are slightly enriched in the 70 ka soil, further supporting that the addition of dust has measurable effects on soil development. The balance between element gain from atmospheric dust and loss via mineral dissolution may be the main control on the soil nutrient budget at Reunion Island, but further research is needed to quantify the composition of the dust in order to make meaningful estimates of long-term soil sustainability.

Degree Type

Thesis

Degree Name

BSci Hons

Department

School of Earth & Environmental Sciences

Advisor(s)

Anthony Dosseto

Keywords

major trace elements, geochemistry, soil sustainability

The effect of time on soil development: study of a soil chronosequence from Reunion Island, Indian Ocean

Alex Hannan-Joyner

12th October, 2016

Submitted in part fulfilment of the requirements of the Honours degree of Bachelor of Science in the School of Earth and Environmental Sciences, University of Wollongong 2016

The information in this thesis is entirely the result of investigations conducted by the author, unless otherwise acknowledged and has not been submitted in part, or otherwise, for any other degree or qualification.

Alex Hannan-Joyner

12th October 2016

Acknowledgements

I would like to extend my thanks to everyone who has helped me throughout the year; naturally this starts with the main man, Dr. Anthony Dosseto, whose counsel and support was gratefully received. Frankly, I don't understand how one man can know so much, but I guess that comes from having a deep curiosity about nature. Thanks for giving me the geochemistry bug.

I'd also like to thank Lili Yu, whose technical support in the lab was invaluable, and Jose Abrantes for his assistance with sample preparation. I'd also like to give special thanks to Davide Menozzi, whose expertise and pursuit of analytical excellence in the lab has given me a solid foundation. My appreciation also extends to the 2016 Honours cohort; you guys are some of the most friendly and down to earth people I have met – and Holly Taylor, whose humour made long lab days bearable. I'd also like to thank my grandmother, and my parents, for their support and good humour. It goes without saying how lucky I feel to have you as family. I love you so much.

Finally, I'd like to dedicate this thesis to my grandfather, William Hannan. I didn't know him very well. But I would give almost anything to tell him of the things I have learnt during my time at Wollongong.

Abstract

Here, presented for the first time, are the results of a geochemical analysis on a soil chronosequence from Reunion Island, Indian Ocean. The soils are defined by three profiles of ages 20 ka, 70 ka and 2 Ma, but all have evolved from the same basaltic parent material, climate, biota and topography, and so form a chronosequence. Using X-Ray Diffraction (XRD), we observe the rapid depletion of the major rock forming minerals – olivine, pyroxene, plagioclase – during the first 70 ka of soil formation. Conversely, there is rapid formation of secondary minerals over the same period, here defined as gibbsite, halloysite and goethite. Interestingly, halloysite, rather than gibbsite, is the dominant phase in the 2 Ma profile, and suggests Si is being conserved at the expense of Al. Additionally, Quadrupole Inductively Coupled Plasma Mass-Spectrometry (Q-ICP-MS) has enabled the concentrations of 19 elements to be measured with remarkable precision. By computing mass-transfer coefficients, identifying elements that are depleted and enriched throughout the profile can be achieved. At Reunion Island, niobium (Nb) is chosen as the index element for these mass-transfer calculations because it shows the greatest immobility. The alkali and alkaline earths are rapidly lost at the surface during the first 20 ka, mainly as a result of plagioclase dissolution. By 70 ka, however, the elements are gained at the surface, and suggests that marine aerosol and dust are able to contribute to the soil nutrient budget. The extent of these gains increases with increasing ionic radius (or equivalently, with decreasing hydration energy), and hypothesize that the fixation ability of clays, which increases with decreasing hydration energy, is responsible for the progressive enrichment of Mg (least) to Cs (most). After 2 Ma, the elements approach 100% depletion, except for Cs and Ba, and is assumed that these elements become immobile once adsorbed onto the surfaces of clays. It is our understanding this is the first time this has been observed in-situ. Meanwhile, the rare earth elements (REE), Mn, and Cu become progressively depleted with soil age, and hypothesise this is due to declining pH and Eh, both with decreasing depth in the soil profiles and over time across the chronosequence. Uranium and Th remain immobile, but are slightly enriched in the 70 ka soil, further supporting that the addition of dust has measurable effects on soil development. The balance between element gain from atmospheric dust and loss via mineral dissolution may be the main control on the soil nutrient budget at Reunion Island, but further research is needed to quantify the composition of the dust in order to make meaningful estimates of long-term soil sustainability.

Table of Contents

Figure List

Table List

Chapter 1: Introduction

Soil forms from the weathering of bedrock and is a mixture of rock, clay, organic matter and water. Weathering of bedrock occurs because the abundance of water, oxygen and acid at the earth's surface causes the minerals in rock to break down and form new minerals that are more stable (Anderson and White 2007). This drive towards chemical stability is the reason why hard, dense rock can be turned into soft, fertile soil. In the process of turning rock into soil, elements are transferred from unstable primary rock forming minerals into new stable secondary minerals and dissolved ions. These reactions require water and will often release elements into forms that plants can use, replenishing the soil nutrient bank. Some reactions will partially dissolve minerals and in the process, consume carbon-dioxide from the air and lock it up inside new minerals. The dangers of global food security and climate change demand that we understand these processes, not only on the timescale of decades, but thousands of years. How can we study soil evolution if the timescales involved are so far in excess of an average human life? Additionally, how can we be sure that any observed changes in soil are a result of time only, and not from other variables like climate, which would otherwise mask its effects? One way to study how soil evolves over time is to compare soils that differ in age, but share the same climatic, topographic, biogenic and geologic characteristics during formation. Such groups of soils are called chronosequences and are a powerful way to study soil development. Additionally, in landscapes where chemical weathering rates are high, geochemical trends that would otherwise take hundreds of thousands of years to develop in soils can instead be seen on much shorter timescales.

Reunion Island, in the south-west Indian Ocean, is an ideal environment to study soil evolution because its chemical weathering rates are some of the highest on earth (Louvat and Allegre 1997), and the age of the parent material – which constrains the rate of soil-forming processes - is known. Additionally, the use of Quadrupole Inductively Coupled Plasma Mass Spectrometry (Q-ICP-MS) has enabled a precise characterisation of the chemical changes in three differently aged soils on Reunion Island. Although the results of this project have practical applications in assessing the long-term sustainability of soil nutrition at Reunion Island, they can also be applied more generally to other soils around the world.

Aims and Objectives

Soil chronosequences, i.e. soils that differ in age only, provides one means of studying the effect of time on soil development. For this project, grain size, mineralogy and major and trace elements will be analysed in the soils of three weathering profiles from a Reunion Island chronosequence. Reunion Island has some of the highest chemical and physical weathering rates on the planet because of its tropical climate and young, reactive basaltic geology (Louvat and Allegre 1997). By analysing the mineralogy and major and trace elements of a soil chronosequence on Reunion Island using X-Ray Diffraction (XRD) and Q-ICP-MS, the development of soil over time will be characterised. For the major and trace element component, 19 elements have been selected that respond differently to changing soil condition. By measuring the concentration of these elements vertically within each profile, their depletion, enrichment or immobility can be observed over the 2 Ma sequence. If a certain element has been lost or gained throughout the soil profile, the sources and processes that must have occurred during its evolution can be isolated. However, in order to make valid conclusions from these elemental concentrations, two corrections must be applied. Firstly, to know if an element is depleted or enriched, the concentration of each element in the soil must be normalised to its concentration in the bedrock. Secondly, to remove the effects of soil compaction and dilation, these concentrations are normalised by the concentration of an immobile element. Not accounting for changes in soil density would otherwise skew the result. Performing these calculations produces a unitless number, called the mass transfer coefficient, and reveals if an element has been gained, lost or remained unchanged in the soil (Brimhall and Dietrich 1987). If mass transfer coefficients are calculated for each sample within a profile, an element profile is produced, a geochemical signature that reveals how changing soil conditions varies with depth. If the same elemental mass transfer coefficient is calculated for the other soils in the chronosequence, a second dimension, time, to added to the analysis. This provides an opportunity to not only study how soil evolves vertically in space across each soil horizon, but also through time across the chronosequence. Since each element has a unique behaviour in soils, a collection of them spanning the periodic table can reveal the nature of soil evolution.

Chapter 2: Literature Review

2.1 Silicate weathering and the carbon cycle

Weathering is the physical and chemical alteration of rocks and minerals at or near earth's surface that tend towards a new equilibrium because of a change in environment (Pope *et al.* 2002). Chemical weathering, i.e. the breakdown of rock by chemical reactions is the central driver of soil evolution, and occurs because rocks and magma formed at depth become chemically unstable when they are brought to the surface by tectonic uplift or volcanic eruption. Primary minerals, i.e. those formed at depth as part of a crystallising melt, begin to transform into secondary minerals that are much more chemically stable when extruded to the surface of the earth. The abundance of water, oxygen and carbonic acid in surface environments are much higher than those at depth, so primary minerals will tend towards a new thermodynamic equilibrium with the surface environment and begin to weather. This drive towards equilibrium gradually removes the most unstable elements in the mineral, and will usually involve some combination of dissolution, hydration, hydrolysis or oxidation (Ryan 2014). The ability of a mineral to weather fast or slow depends on if and how well the oxygen and silicon atoms of the mineral are linked together, with more linking resulting in greater weathering resistance. This weathering sequence is called the Goldich dissolution series and was formalised in 1938 by S. S Goldich (Goldich 1938).

The Goldich dissolution series is controlled by the degree of linking, or polymerisation, between the silica tetrahedral (SiO_4) in each mineral. One of the minerals most susceptible to weathering, olivine $(Mg,Fe)_2SiO_4$, has isolated SiO_4 tetrahedra and will readily decompose in the presence of a weakly acidic solution. This happens because the oxygen bonds form weak ionic bonds with the Mg and Fe atoms, and in the presence of water, these bonds can be broken with relative ease (Ryan 2014). On the other hand, a mineral that is resistant to chemical weathering, such as zircon ($ZrSiO_4$) has oxygen atoms that are covalently bonded to each other in a framework structure, and are very difficult to break apart (White and Brantley 1995). The strength of this covalent bond is mainly controlled by the size and charge of the ion, with small, highly charged ions such as Zr^{4+} forming the strongest bonds with oxygen.

However, no mineral is completely resistant to chemical weathering over geological time. This implies that every mineral has a specific dissolution rate that dictates its longevity in the environment. These dissolution rate constants are generally determined in the laboratory by dissolving a 1mm grain in dilute acid, and vary by orders of magnitude (Figure 1):

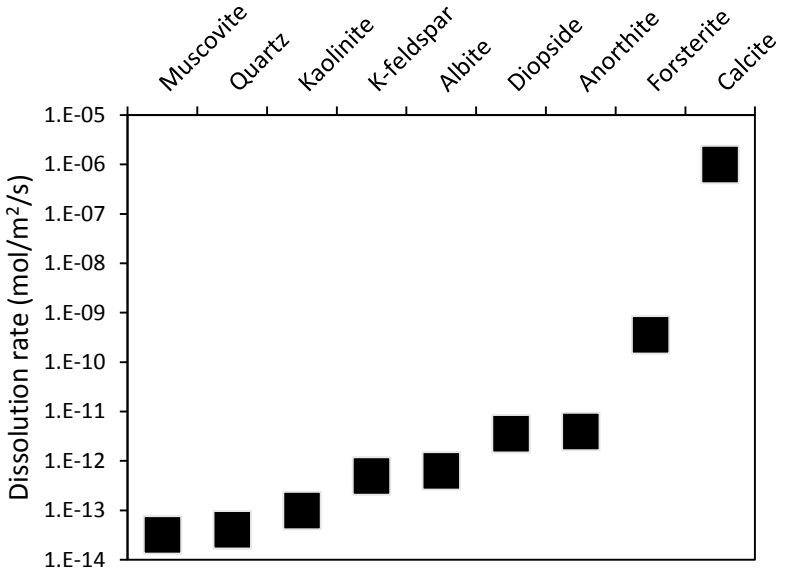

Figure 1*: Disolution rates of common rock-forming minerals. The dossolution rate is calculated using a hypothetical 1mm sphere of each mineral in a solution of pH = 5. Data from Chou et al. (1989) and Brantley (2008).*

Interestingly, many lab-derived results of mineral and rock weathering rates differ by orders of magnitude to weathering rates determined in the field (White and Brantley 2003). Navarre-Sitchler and Brantley (2007) hypothesise this lab-field discrepancy is caused by the inability to measure comparable surface areas across different scales, which result in large errors being extrapolated. In order to correct for this scaling error, they propose a fractal coefficient be applied when calculating weathering rates. In any case, the dissolution rates above in Figure 1 are still useful for comparing the weathering rates of rock-forming and secondary minerals. It is evident from Figure 1 that the proportion of covalent bonds in a mineral does indeed affect its dissolution rate. The two end-members, muscovite and calcite have the lowest and highest weathering rate respectively. This can be explained in terms of the main bond type in each mineral; muscovite is dominated by strong covalent bonds between the silica tetrahedra, while calcite is dominated by weak ionic bonds between the calcium and carbonate ions.

Minerals that have both ionic and covalent bonds between member atoms, such as plagioclase, weather at intermediate rates. Purely ionic bonds allow all of the ions to be dissolved during chemical weathering, while a mix of ionic and covalent bonds will result in the partial dissolution of that mineral.

If a mineral dissolves completely or partially during chemical weathering, it can be described as congruent or incongruent dissolution, respectively (Ryan 2014). Most silicate minerals weather incongruently because the solubility of cations typically associated with silicates (Si^{4+}, Al^{3+}, $Fe^{2+,3+}$ etc.) is relatively low (Figure 2). However, their solubilities can be affected by the pH, redox potential, ionic strength and presence of complexing agents in solution (White and Brantley 1995). Whether or not a reaction proceeds congruently or incongruently depends not only on the ionic-covalent makeup of a mineral but also on the acidity and amount of dissolved oxygen in the solution. Additionally, the abundance of other dissolved ions in solution may change the stoichiometric-favourability of certain dissolution reactions. Mineral dissolution typically occurs as a result of the hydrolysis reaction and given its importance in soil formation, is briefly outlined below.

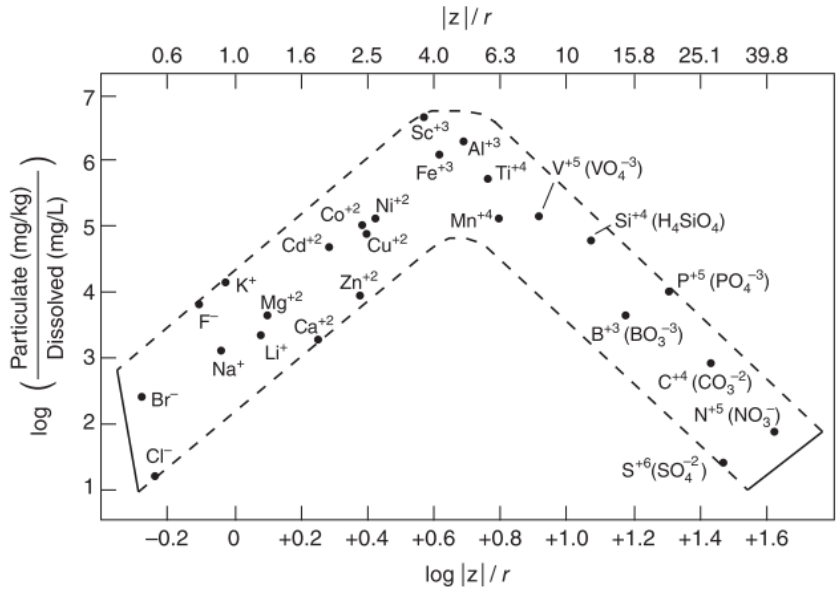

***Figure 2**: Predicted solubilities of common aqueous ions based on ionic potentials, i.e. the ratio of the ionic charge (z) to ionic radius (r, in angstroms) (Ryan, 2014).*

Hydrolysis reactions occur because the bonds between the alkali and alkaline earth metals (e.g. Na, Mg) and the silicate tetrahedra in the mineral are mainly ionic and therefore vulnerable to breaking in the presence of carbonic acid. The products of a hydrolysis reaction are a clay, dissolved cations and silica, and bicarbonate. A typical example is the decomposition of Albite (Ab) by carbonic acid, forming Kaolinite (Kln) plus bicarbonate (Equation 1) (Ryan 2014):

$$2NaAlSi_3O_8\ (Ab) + 2H_2CO_3 + 9H_2O \leftrightarrow 2Na^+ + 2HCO_3^- + Al_2Si_2O_5(OH)_4\ (Kln) \quad \textit{Equation 1}$$

Because carbonic acid can be introduced into soils by rain and plants, it is a major control on chemical weathering rates and it is also the main regulator of mineralising atmospheric CO_2 into its highly soluble form bicarbonate. The transformation of carbon dioxide as carbonic acid to bicarbonate (Equation 2) is a critical process in the carbon cycle because the carbonate ion can bond to Ca^{2+} ions in the ocean and form calcium carbonate ($CaCO_3$), sequestering carbon in limestone for geological timescales.

$$CO_2 + H_2O \leftrightarrow H_2CO_3 \leftrightarrow CO_3^{2-} + 2H^+ \leftrightarrow CO_3^{2-} + Ca^{2+} \leftrightarrow CaCO_3 \quad \textit{Equation 2}$$

The strong covalent bond between the carbon and oxygen atoms in the carbonate ion means that even if calcium carbonate is dissolved, the carbon is still locked up as the carbonate ion.

Although hydrolysis reactions play a major role in chemical weathering, other reactions, such as redox and hydration reactions also contribute to the formation of important soil-forming minerals such as goethite (FeOOH). Goethite is an important soil mineral because it often controls the mobility, and therefore the plant availability of trace elements such as Mn and Cu. Goethite can be formed either by the oxidation of Fe^{2+} ions in solution:

$$Fe^{2+} + 2H_2O \leftrightarrow FeOOH + 3H^+ + e^- \quad \textit{Equation 3}$$

Or by the hydration of the mineral hematite (Fe_2O_3):

$$Fe_2O_3 + H_2O \leftrightarrow 2FeOOH \qquad \textit{Equation 4}$$

Whether goethite, or any other secondary mineral forms via oxidation or hydration reactions depends on the abundance of water and oxygen in the soil (Schwertmann and Murad 1983).

From this brief overview of chemical weathering, soil can be viewed as a dynamic environment that is affected by chemical, physical and biological agents. By integrating these processes into a unit called the ‘critical zone’, the impact they have on soil development can be understood.

2.2 The Critical Zone

Soil is formed at the interface between the atmosphere, lithosphere and biosphere, i.e. the 'Critical Zone'. The Critical Zone (CZ) is defined as the region between vegetation and the lower limits of groundwater and forms a mixture of minerals, organic matter, air, water and biota (Brantley *et al*. 2007; Figure 3). Each of these factors influences one another to varying degrees; for instance, the chemical breakdown of primary minerals, aided by physical weathering, provides energy gradients for plants to exploit. Upon respiration, plant roots emit CO_2 which accelerate chemical weathering. This coupling of physical, chemical and biological factors controls the rate at which soil develops and regulates the cycling of chemicals in the environment.

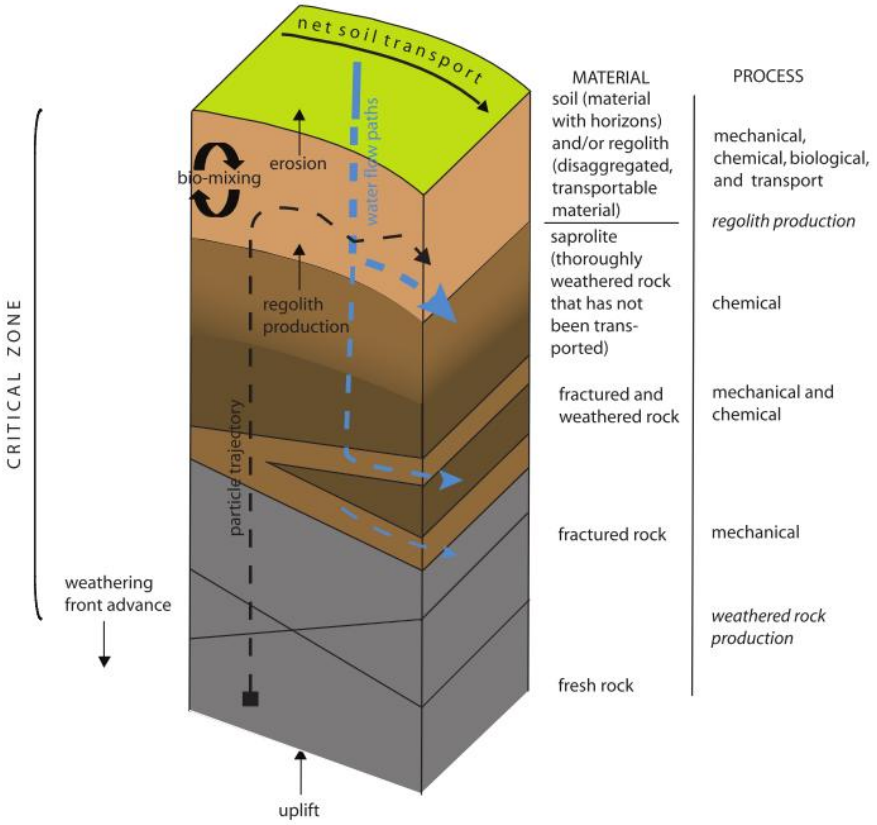

***Figure 3**: A vertical slice of the CZ. As the weathering front advances through the parent material, a particle (black dashed line) will approach the surface due to surface erosion. On approach it will be exposed to various weathering processes, from mostly mechanical at the bottom, to mechanical, chemical and biological processes at the surface. (Anderson et al. 2007).*

The interface between the unconsolidated material at the bottom of the CZ and the solid bedrock is termed the 'weathering front', and moves downwards as the bedrock is progressively weathered. The volume between the fresh bedrock and the surface of the soil has been described by Brantley *et al.* (2007) and Anderson *et al.* (2007) as a 'weathering engine' that is continually reacting with its surrounding via chemical, biological and physical weathering. Biological weathering is mainly caused by respiration of plant roots which increases the amount of CO_2 in the soil by several orders of magnitude, forming carbonic acid that breaks down silicate minerals (Amundson *et al.* 2007). Physical weathering on the other hand aids both chemical and biological weathering because of its ability to increase the surface area of rocks. In a soil profile, the weathering of bedrock ultimately results in its disintegration because internal stresses overcome the strength of the rock. Stresses occur as a result of thermal contraction and expansion and salt, ice or root growth in rock that creates cracks and joints (Schaetzl and Thompson 2015). Although soil can form by the weathering of bedrock, it can also form from the weathering of loose, unconsolidated rock, i.e. alluvium. Compared to bedrock, alluvium may experience a wider range of mechanical weathering mechanisms including glacial grinding, fluvial corrosion and eolian abrasion and under some conditions may form soil faster (Schaetzl and Thompson 2015). Regardless of whether the parent material is bedrock or alluvium, physical weathering is essential in the formation of soil because it rapidly increases the surface area of the rock and therefore accelerates chemical reactions. In increasing the surface area, rocks, by definition, must break down into smaller grains. Silt sized particles (< 63 um) are usually the smallest grains made by physical weathering and requires chemical weathering to form smaller clay sized particles (< 2 um) (Anderson *et al.* 2007).

The end result of bedrock being continuously fractured, ground and dissolved by water, ice, rocks and plants is the production of soil. The thickness of soil is dynamic and determining if the CZ is thickening, thinning or in equilibrium is a key component in assessing soil sustainability (Montgomery 2007).

The rate at which weathering of bedrock (essentially a biogeochemical process) and erosion (a physical process) of regolith operate defines whether the CZ is thickening, thinning, or at equilibrium (White 1995). The conversion of bedrock into regolith occurs at the weathering front and the rate at which it propagates downwards is controlled mainly by the bedrock lithology and the thickness of the overburden. However, early results do seem to indicate the importance of lithology in bedrock weathering. For example, Dosseto *et al.* (2012) calculated a regolith production rate for a volcaniclastic profile five times faster than for a quartz-diorite, despite both being subjected to similar climates. This dependence on lithology can be linked back to the mineralogy of the rock, with mafic minerals weathering orders of magnitude faster than intermediate or felsic minerals. Calculating rates of bedrock weathering (e.g. by using U-Th isotopes) is a relatively new development and there is considerable uncertainty regarding the validity of the method. However, it provides a powerful tool for constraining rates of soil formation.

In a similar way to lithology, soil profile thickness is recognised as a major constraint to regolith production rates. Ahnert (1967) and Heimsath *et al.* (1997) suggest that the rate of soil production decreases exponentially with soil thickness because water infiltration and soil temperature, major controls on chemical kinetics, decrease with depth. However, Humphreys and Wilkinson (2007) propose that there is an optimum soil thickness that allows for the fastest possible soil production rate. Since water is the main agent of weathering, soils that are too thick or thin will either stop it from reaching bedrock or will cause it to runoff the surface without penetrating into the soil.

Although these weathering processes persist inside the critical zone so long as there is some kind of disequilibrium (e.g. fresh bedrock in contact with water), changes in climate, tectonics and human activity can alter the ‘weathering engine’ such that its sustainability is affected. By developing models to describe how the CZ changes over time, we can assess soil sustainability on a quantitative basis. These models have evolved as our understanding of soils have improved, but generally describe soil as a product of energy transformation, continuous processes or external factors (Minasny *et al.* 2008).

2.3 Models of Critical Zone development

Attempts to model pedogenesis (i.e. soil formation) has existed since Charles Lyells publication of 'Principals of geology' in the early nineteenth century (Lyell 1837). The difficulty in modelling soil formation stems from the existence of processes and features in soil that vary in both space and time by many orders of magnitude. For example, soil is studied on the spatial scale of atoms (trillionths of a meter), minerals (thousandths of a meter), soil profiles (centimetres to metres) or on the watershed scale (kilometres to hundreds of kilometres). Temporally, soils are studied through the lens of chemical or mechanical kinetics, which operate on the scale from microseconds to millions of years. Over time, the product of these processes are ultimately expressed in soil as horizons, i.e. layers in the soil profile that are defined by certain properties. Since Jenny's 1941 publication 'Factors of soil formation' (Jenny 1941), models attempting to unify these processes have appeared throughout the literature. These models tend to integrate one of three concepts used to quantify their results: the flow of energy in soil systems, environmental factors, or soil formation processes (Minasny *et al.* 2008; Figure 4). A brief overview of these models is discussed below.

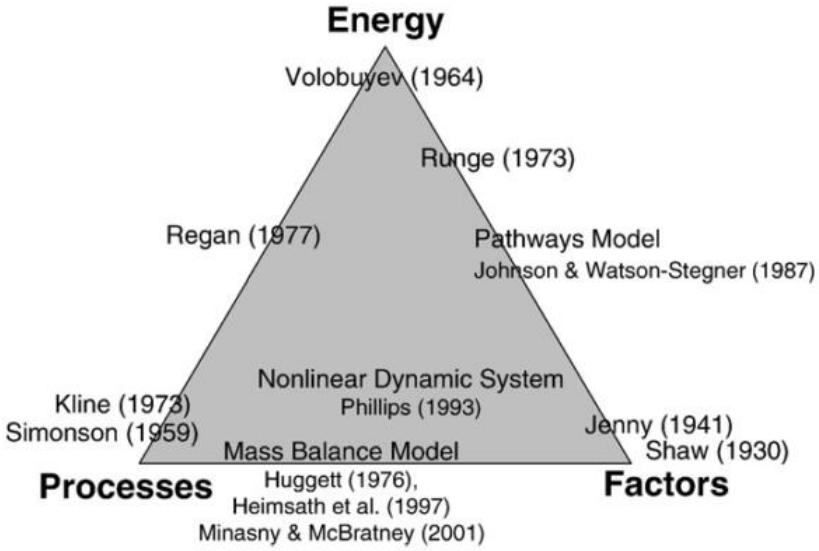

Figure 4*: Concepts used to explain soil formation. (Minasny et al. 2008).*

Jenny (1941) was the first to articulate a quantitative model of soil formation using the factor based approach:

$$s = f(cl, o, r, p, t) \qquad \textit{Equation 5}$$

where *s* is soil properties, *cl* is climate, *o* is biota, *r* is relief, *p* is parent material and *t* is time.

In this model, soil properties are described as a function of these five variables. The equation can solved theoretically, or empirically by holding four of the five factors constant and solving for the variable. If it is solved empirically, the effect the variable factor has on soil development can then be described. For example, if a sequence of soils experiences the same climate, biota, relief and parent material but differ in age, we can evaluate how time affects soil development. Such sequences are called chronosequences and together with climosequences, biosequences, toposequences and lithosequences, offer a practical basis for assessing the effect that each factor has on soil evolution. Chronosequences, for example, are useful in evaluating soil evolution because any compositional difference between two or more soil profiles is likely to be the result of time-dependent processes only, such as chemical weathering (Huggett 1998). This makes them useful for investigating the magnitude and direction of kinetic processes in the soil, and provides a baseline for testing theories of soil formation (Huggett 1998). Chronosequences have been used to study how changes in soil nitrogen and phosphorus (Piccolo *et al* .1994, Crews *et al.* 1995; Chadwick *et al.* 1999), horizon thickness (Ampe and Langohr 1993), clay mineralogy (Reheis 1990), primary silicate reaction rates (White *et al.* 1996) and exchangeable cations (Bain *et al.* 1993; Porder *et al.* 2004) change over time..

Objections to Jenny's factorial model have been made on grounds of oversimplification (e.g. Runge 1973). Runge (1973) for instance proposed that energy, rather than environmental factors, is the key to understanding soil formation. In this model, gravitation is the key driver of soil processes in soil, controlling the flow of water and therefore the rate of chemical weathering. Conceptually, the model could be useful but it fails to quantify the energy actually required for soil forming processes.

Quantification of the energy used and given by soil forming processes was first developed by Volobuyev (1964) who based his model on the first law of thermodynamics (i.e. that energy cannot be created or destroyed, only transferred to one form to another). Specifically, the model states that the energy involved in soil formation is the sum of the energy required for evapotranspiration, biomass production and mineral weathering. The overwhelming majority of the energy budget is spent on evapotranspiration (>95%), while biomass production requires less than 5% and mineral weathering less that 0.01%.

Volobuyev and Ponomarev (1977) later expressed different soil types in terms of its free energy (ΔG) and entropy:

$$\Delta G = \Delta H - T\,\Delta S \qquad \textit{Equation 6}$$

where ΔH is the heat of reaction (enthalpy) involved in the making and breaking of bonds and TΔS is the heat that the systems gives or takes to its surroundings. Within the context of soil formation, the entropy of a soil is defined by the extent of mineral weathering, with highly weathered soils attaining high entropy. Volobuyev and Ponomarev (1977) were able to quantify a positive correlation between progressively weathered soils and increased entropy. This contrasts to Smeck *et al.* (1983) interpretation of entropy who considered not only disorder on the atomic scale, but also on the profile scale. Although mineral dissolution increases entropy at the atomic scale, Smeck *et al.* (1983) suggests that it actually increases the entropy on the profile scale due to the formation of soil horizons and the precipitation of secondary minerals. In this case, highly weathered soils such as ferrosols that lack obvious horizon development would have low entropy, rather than high entropy as Volobuyev and Ponomarev (1977) would interpret. Although these energy-based models have occasionally been used to explain soil evolution successfully (e.g. Regan 1977), the models are rarely used today with process-based models of soil development, particularly mass balance, becoming the dominant technique.

The premise of the geochemical mass balance is to compare the mass, or ratio of two or more elements in a system. A difference between the two masses means that one part of the system has been lost or gained, an inference that may otherwise be difficult to find. Mass balance has been used to constrain rates of chemical weathering on both the watershed scale (e.g. Louvat and Allegre 1997, Anderson *et al.* 2002) and at the soil profile scale (e.g. Chabaux *et al.* 2003). At the scale of the soil profile, geochemical mass balance can be effectively used to study its chemical evolution. This is achieved by comparing the concentration of an element of interest in the soil (normalised to an immobile element) against the concentration of the same element in the parent material (also normalised to an immobile element). This produces an element profile, or 'geochemical fingerprint' that can tell us whether an element has been gained, lost or remained immobile in the soil.

Knowing whether an element has been gained, lost or remained immobile can reveal information about the sources and intensity of processes affecting soil development. For example, Brantley *et al.* (2007) outlines a geochemical mass balance method derived from Brimhall and Dietrich (1987). In this model, the concentration of an element in the soil, such as Na, is normalised against the concentration of an immobile element in the unweathered bedrock; immobile elements typically used are Ti, Zr or Nb because they generally form stable, refractory oxides such as rutile and zircon that are highly resistant to weathering and leaching. The concentrations of the element in the regolith is normalised against the concentration of the corresponding immobile element so that the effect of soil contraction and expansion (i.e. element enrichment and dilution) is accounted for. The calculation produces a unitless number called the mass transfer coefficient (tau) that reveals whether an element has been gained or lost in the soil. The equation for calculating this coefficient is shown below:

$$\tau = \frac{C_{j,w}\, C_{i,p}}{C_{j,p}\, C_{i,w}} - 1 \qquad \textit{Equation 7}$$

where τ is the mass transfer coefficient of the required element and C is the concentration of the required element (j) or immobile (i) element in weathered (w) or parent (p) material.

A mass transfer coefficient equal to zero means the element has been neither lost nor gained in the soil. Positive values indicate elemental gain while negative values indicate loss. While there is no theoretical upper limit for the mass transfer coefficient, it cannot be less than -1 because not more than 100% of an element can be lost from regolith in relation to its concentration in bedrock.

When the mass transfer coefficient is calculated for each soil sample throughout a profile and plotted against depth, the behaviour of the element of interest throughout the regolith can be observed. Brantley (2007) identified that for a given element, a weathering profile will approach one of five elemental end members: immobile, depleted, depleted-enriched, addition or biogenic. By definition, these end-members are idealized outcomes and will not always be observed in nature. The five end-members are outlined below in Figure 5.

Elemental profile	Plot
Immobile profiles form when elements are neither gained nor lost from the soil profile because of their association with weathering-resistant minerals (e.g. Zr in zircon). Immobile elements tend to remain at a concentration in the soil similar to the parent material.	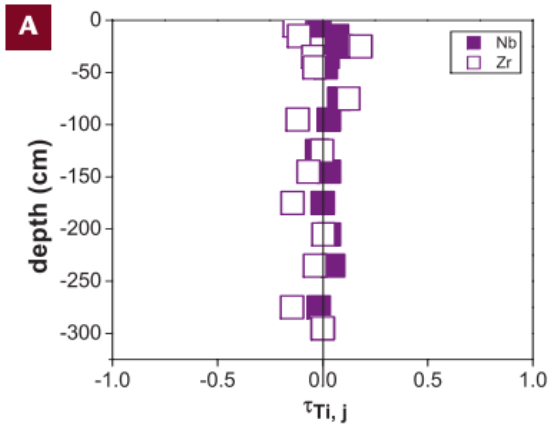
Depletion profiles form when relatively mobile elements are leached from the upper soil profile because the pH or Eh conditions are conducive to their mobilization. Copper for example is mobilised under acidic conditions which may be caused by the formation of organic acids at the surface.	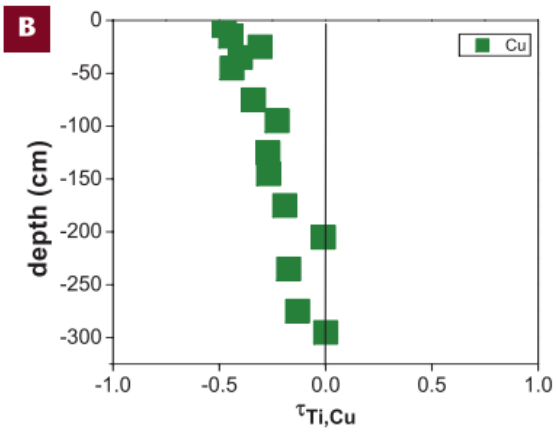

Depletion-enrichment profiles form when elements that become depleted at the surface are enriched further down the profile because of a change in pH or Eh. Aluminium for example is often depleted at the surface because of acidic conditions; when the Al leaches towards the bottom of the profile, conditions may become more alkaline and immobilise it at depth.

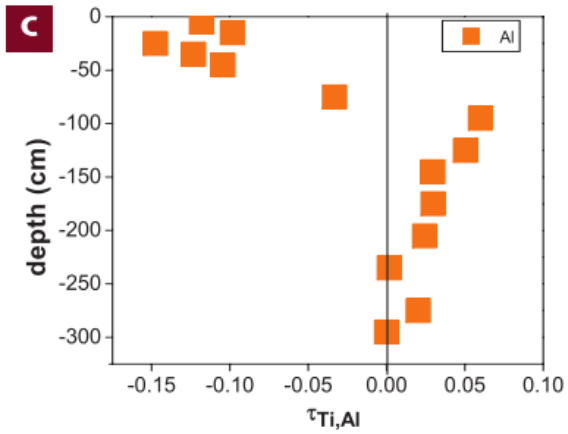

Addition profiles can be formed if there is an external input of an element into the regolith. Manganese and Fe for example can be added to soils via dust deposition, or fixated by biological processes, as in the case for C.

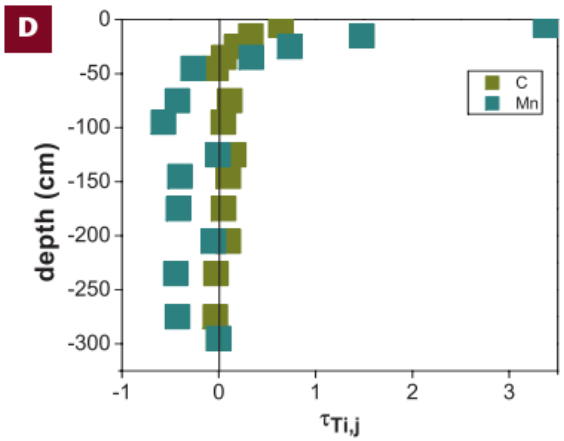

Biogenic profiles are generally enriched in a certain element at the surface and depleted at depth. Potassium for example, is an important macronutrient for plants and will be taken up at depth (becoming relatively depleted) and become recycled at shallow depths where biomass will decay.

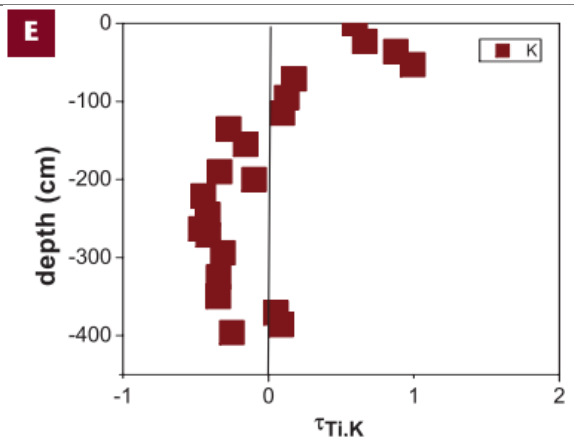

***Figure 5**: Element profile end-members. Collated from Brantley et al. (2007)*

2.4 Geochemistry as a tool for studying soil evolution

Soil can be analysed on the basis of grain size distribution, mineralogy, major and trace elements and how they vary with depth within the profile. If these results are compared across a chronosequence, the nature of soil evolution can be quantified. Mineralogy, for instance can be used as a proxy for soil weathering intensity because the proportion of secondary minerals throughout a soil profile, such as clays, can reveal how much a soil has weathered. Almost all primary silicate phases form secondary silicate phases (e.g. clays) because clays are more thermodynamically stable at the earth's surface than primary phases. Many authors have observed primary phases weathering in the order of the Goldich solubility series. For example, White *et al.* (1996) noted that the relative weight percent of plagioclase and hornblende in a granitic soil decreased consistently with age (200 yr – 3 Ma; Figure 6). In the same study, the proportion of K-feldspar increased in the soils for the first 600 ka and then decreased in the 3 Ma soil, likely as a result of other more soluble minerals being weathered first, increasing the relative concentration of K-feldspars during the first 600 ka. The 3 Ma soil was dominated by clay (kaolinite) and quartz and was essentially free of primary phases. The progressive evolution of soils to tend towards a clay dominated groundmass over time has been confirmed by similar studies by Van Dooremolen *et al.* (1990), Burkins *et al.* (1999) and Vitousek *et al.* (1997).

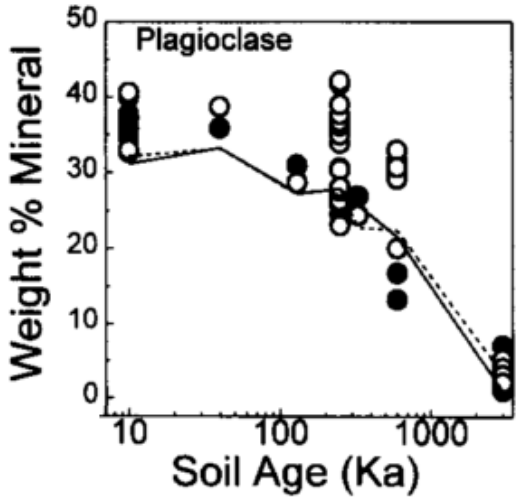

Figure 6*: weight % plagioclase as a function of age in samples from the A horizon (black dots) and B+C horizons (white dots) of a granitic alluvium (White et al. 1996).*

Similarly, the variation in major and trace elements along a chronosequence can also be used as tracers for soil evolution. Major elements (i.e. those that have a concentration in soil > 0.1%) typically studied in soils include the alkali and alkaline earths (e.g. Na, K, Mg, Ca), transition metals (Ti, Mn and Fe) and the post-transition metal Al. Trace elements generally analysed in soils again include the alkali and alkaline earths (e.g. Rb, Sr, Ba), transition metals (e.g. Zr and Nb), the rare earth elements (REE) (e.g. Nd, Eu) and the actinides (typically U and Th). By calculating mass transfer coefficients for a suite of elements in a given soil profile, soil forming processes can be identified vertically through each horizon. If the process is repeated for a chronosequence, soils evolution can be studied within the context of mineral dissolution, dust deposition and organic matter formation.

The use of the alkali and alkaline earth elements in chronosequence studies have been used, among others, to quantify rates of mineral dissolution (e.g. White *et al.* 1996), atmospheric CO_2 drawdown (e.g. Taylor and Blum 1995) and the sustainability of soil fertility (e.g. Vitousek *et al.* 1997; Chadwick *et al.* 1999), and so constitute an important geochemical tool for studying soil evolution. Their versatility as useful chemical weathering proxies stems less from their widespread abundance than their behaviour in the environment. Since they only exist in a single oxidation state, their behaviour in soil can be attributed to mineral dissolution with greater certainty (Nesbitt and Markovics 1980). Additionally, since the elements have large ionic radii and low charge, they are soluble in solution and their concentration in rivers and streams are often used to quantify the extent of chemical weathering in a catchment. Therefore in most soils, the distribution of these cations is mainly controlled by 1. mineral dissolution, because they are major constituents of primary phases and 2. leaching because their low charge and large radius makes them soluble. For example by using the alkali and alkaline earths, Bain *et al.* (1992), Taylor and Blum (1995), White *et al.* (1995) and Vitousek *et al.* (1997) all observed their rapid depletion in soil with increasing age throughout various chronosequences (with typically <10% of the initial base cations remaining after several tens of thousands of years; Figure 7). Some studies, (e.g. Taylor and Blum 1995) have used the mass-balanced concentrations of the cations to calculate weathering rates as a function of soil age. In these studies, the mobile element is normalised against an immobile element (e.g. Ti) to see how the mobility of the element changes over time. Such studies show that chemical weathering rates typically decrease logarithmically over time as a result of decreased mineral surface reactivity caused by dissolution (e.g. White *et al.* 1996; Figure 8).

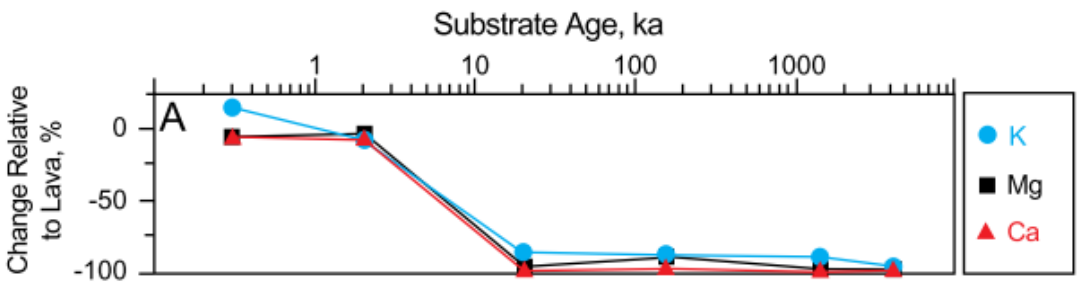

***Figure 7**: The remaining fraction of parent material-derived K, Mg and Ca across a Hawaiian soil chronosequence (Vitousek et al. 1997)*

Since elements of the same periodic group generally display similar geochemical behaviour, the alkali and alkaline-earth trace elements (e.g. Sr, Rb) have also been used successfully as proxies to determine geochemical behaviour in chronosequence studies. For example, Huang *et al.* (2004) used the Ba/Nb ratio as a proxy for rock weathering intensity and determined that the rate that Ba is leached from soil decreases logarithmically over time. The similarity in behaviour to the major cations was attributed to the ability of Ba to replace Ca in plagioclase, and hence leached from the mineral to a similar rate.

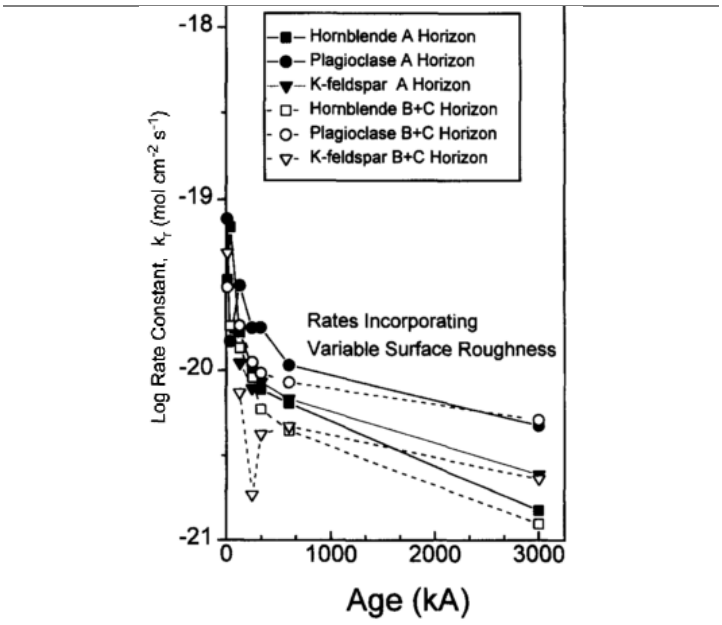

***Figure 8**: Calculated dissolution rate constants for primary minerals as a function of soil age. Rates incorporate grain surface area. (White et al. 1996).*

The behaviour of the transition metals are somewhat more complex. Unlike the alkali and alkaline earths, most of the transition metals are sensitive to changes in soil redox, pH and readily form complexes with ligands, all of which greatly affect cation mobility (Ryan 2014). Some cations, particularly those belonging to groups 4 and 5 of the periodic table (Ti, Zr, Nb, Ta), display remarkable immobility in soil, even under conditions most conducive for enhanced cation mobility (e.g. relatively acidic and oxidising). Chronosequences have been used to verify that their immobility extends into geological time (> 1 Ma). Kurtz *et al.* (2000) for example used a basaltic chronosequence on Hawaii to assess the mobility of commonly used immobile elements used in mass transfer equations (Nb, Ta, Zr, Hf and Th). The study concluded that the Nb/Ta ratio remained essentially constant both vertically in the soils and across the chronosequence, suggesting Nb/Ta is not fractionated during bedrock weathering and implies that both elements are immobile (Figure 9). Other ratios, such as Zr/Hf, remained constant throughout the 20 ka profile, but in the 150 ka profile, Zr and Hf were depleted by about 25% relative to Nb. This is a significant finding considering both Zr and Hf are commonly assumed to be immobile.

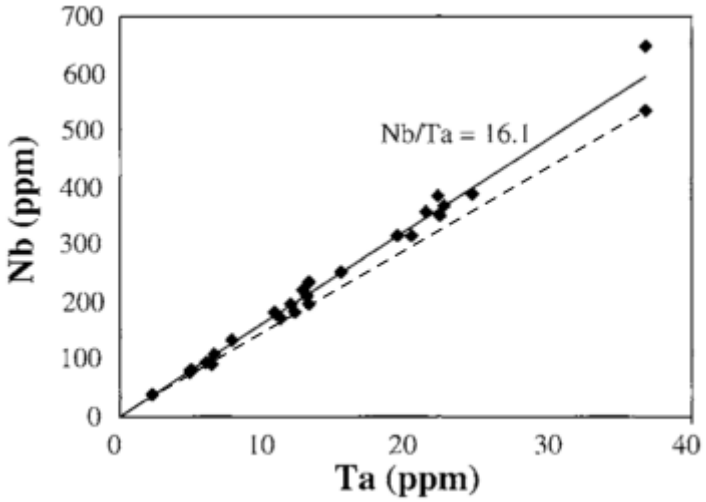

***Figure 9**: Niobium vs. Ta concentrations for chronosequence soil horizons. Dashed line shows model Nb/Ta ratio of atmospheric dust. (Kurtz et. al 2000).*

The other transition metals commonly studied in chronosequences, Mn, Fe, Cu and Al, can be useful traces in tracking changes in soil pH and Eh. Their usefulness as recorders of geochemical change stems from the fact that they exist as different species in soil depending on the amount of acid and oxygen in the soil (Schaetzl and Thompson 2015). The mobility of certain elements can either be enhanced or degraded mobility, so their absence or presence in soils can infers us about their past or present conditions. Similarly, one member of the REE can serve as a recorder of soil redox: Ce. The REE are defined as the 14 elements that span the lanthanide series of the periodic table, from La to Lu. They share similar geochemical behaviour due to their single 3+ oxidation state, except for Ce. Depending on the redox of the soil, Ce can exist as either Ce^{3+} in its free state or as Ce^{4+} as the oxide CeO_2 (Laveuf *et al.* 2009). Since Ce^{3+} and the other REE are much more mobile than CeO_2, a soil enriched in Ce relative to the other REE indicates the soil has been oxidised. This is called the cerium anomaly and is a user tracer for tracking changes in soil redox.

By analysing a variety of elements in the soil and performing mass transfer calculations, the chemical signature of the soil is revealed. When analysing the soils from a chronosequence, these chemical signatures reveal how fast elements are lost and gained from the soil, both through space and time.

Chapter 3: Regional Setting

Reunion Island is located in the southwest Indian Ocean, 750 kilometres east of Madagascar and 180 kilometres southwest of Mauritius, the closest island (Figure 10). Since soil is a product of various environmental factors, the following section outlines Reunion Island's geology, geomorphology and climate. Following this, details on site selection and sampling are outlined.

***Figure 10**: Yellow star marks location of Reunion Island*

3.1 Geology

The island lies above the Reunion hotspot which has been active for 66 Ma and extends back to the Deccan Traps of eastern India (Morgan 1981). Reunion Island itself was formed by the eruption of two volcanoes: Piton des Neiges, which first erupted 2 Ma ago is extinct and forms the north-western two-thirds of the island; Piton de la Fournaise is active and first erupted 530 ka ago forming the south-eastern part of the island (Louvat and Allegre 1997; Figure 11). There are three main geological formations on the island - Upton and Wadsworth (1965) classified the majority of Piton des Neiges under the Oceanite Series and the late stage

capping lavas (olivine basalt to trachyte) were termed the Differentiated Series. The shields of both volcanoes consist entirely of olivine basalts and their intrusive equivalents. McDougall (1971) determined that the olivine basalts of Piton des Neiges erupted over three stages, beginning 2 Ma, then later at 1.2 to 1 Ma and then 600 ka to 400 ka ago. The youngest lavas which cap the volcano formed between 70 and 350 ka (McDougall 1971). Piton de la Fournaise started to erupt 530 ka ago (McDougall 1971) and continues to be active. Like Piton des Neiges, it is composed almost entirely of olivine basalts, with minor hawaiites, feldparphyric basalts and ankaramites (Upton and Wadsworth 1965).

***Figure 11**: Piton des Neiges, at the north-west of the island and Piton de la Fournaise at the south-eastern part of the island. Profile locations marked by yellow stars.*

The chemical nature of the three formations have been studied in detail using a variety of geochemical signatures. Fisk *et al.* (1988) analysed the Sr and Nd isotopes for a suite of Reunion Island lavas and determined they were of the oceanic basalt group. The chemical signature of these basalts and volcanic intrusives using Sr/Nd ratios and immobile trace element ratios determined by Fisk *et al.* (1988) suggest that the source of the melts from both Piton des Neiges and Piton de la Fournaise is chemically homogenous. This aligns with the results of McDougall and Comston (1965) who used strontium isotopes to conclude there was no isotopic difference between the two volcanic magmas from Piton des Neiges and Piton de

la Fournaise. Although a single homogenous magmatic source is likely to be responsible for melts of both volcanoes, the lavas of Piton des Fournaise are enriched in alkali elements and incompatible elements such as Zr and Nb compared to Piton des Neiges. Therefore, the lavas of Piton des Fournaise requires a process that enriches the melt in alkali elements while at the same time also enriching high field-strength elements (e.g. REE, U, Th, Zr etc). Fisk *et al.* (1988) suggest that a shallow level process is responsible for this anomalous enrichment of alkalis and most of this variability can be explained by crystal fractionation at depths of 2 to 20km.

The Piton des Neiges Oceanite Series lava and Piton de la Fournaise lavas are chemically different (Figure 12) and Fisk *et al.* (1988) calculated the latter experienced 10% more fractionation than the former to explain its slightly higher aluminium, titanium and iron oxide concentrations. However this model cannot explain the variation in incompatible trace element concentration between the two lavas. Fisk *et al.* (1988) proposed the 'steady state magma chamber model', to account for this variation i.e. that small differences in magma chamber geometry can increase the cooling rate of magma, yielding magma that is enriched in trace elements relative to a chamber that cools more slowly. Like the fractionation model though, this explanation is incomplete because it cannot simultaneously account for the enrichment of alkali elements at Piton de la Fournaise.

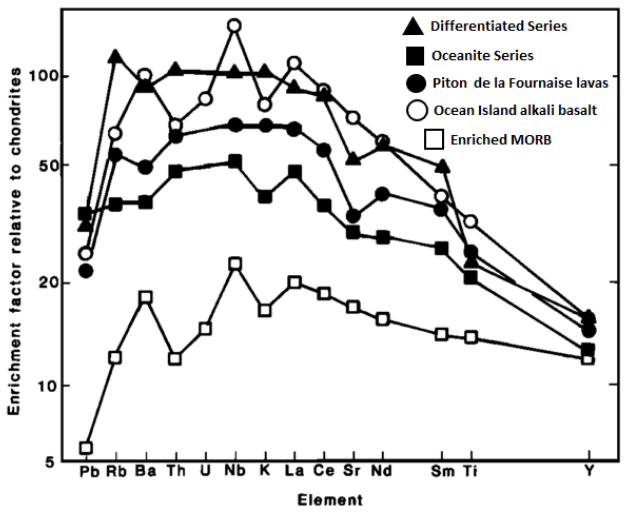

***Figure 12**: Enrichment factors of average incompatible element concentrations in Reunion Island basalts relative to chondrites (solid symbols). For comparison, the average concentrations of alkaline ocean island basalts and MORBs are included (open symbols) (Fisk et al. 1980).*

Unlike the Piton des Neiges Oceanite Series, the Differentiated Series are chemically similar to the basalts of Piton de la Fournaise, being relatively elevated in alkali and incompatible elements. The Differentiated Series are unlikely to have formed by fractionation of magmas similar to those of the Oceanite Series from the primitive volcanic shield because of their poor abundance in incompatible trace elements such as Ti and REE (Zielinski 1975). Fisk *et al.* (1988) suggest that the parent melt of the Differentiated Series may have initially been enriched in incompatible elements and therefore more evolved than the parent melt of the Oceanite Series. This could have occurred if the initial primitive melt became enriched in immobile elements through a single episode of fractional crystallisation. Since the Piton des Neiges Differentiated Series and Piton de la Fournaise are likely to be closely related, the onset of volcanism on Piton des Fournaise (360 ka) probably supplied the magma that formed the Differentiated Series lavas on Piton des Neiges (Fisk *et al.* 1988).

3.2 Geomorphology

Reunion Island extends from the ocean floor exceeding depths of 4000m, is elliptical in shape, an area of 2500 km^2 and a coastline 200 km long (Join *et al.* 2005; Figure 11). The island strikes NW-SE and is topographically defined by the two volcanic massifs, with Piton des Neiges 3070m and Piton de la Fournaise 2630m above sea level. The two volcanoes are heavily eroded, with valleys and chasms incising both structures (Figure 13). The caldera of Piton des Neiges has been damaged by massive landslides to its south, west and northern flanks (Oehler 2003), while Piton de la Fournaise is characterised by three sub-concentric nested calderas opening out to the sea on their eastern side (Chavallier and Bachelery, 1981). The island has three major depressions, believed to be caused by tropical erosion and tectonic events; the steep sided valleys of Cilaos, Mafate and Salazie. They are hypothesised to be the products of mass wasting events that have occurred over the last 2 Ma (Join *et al.* 2005).

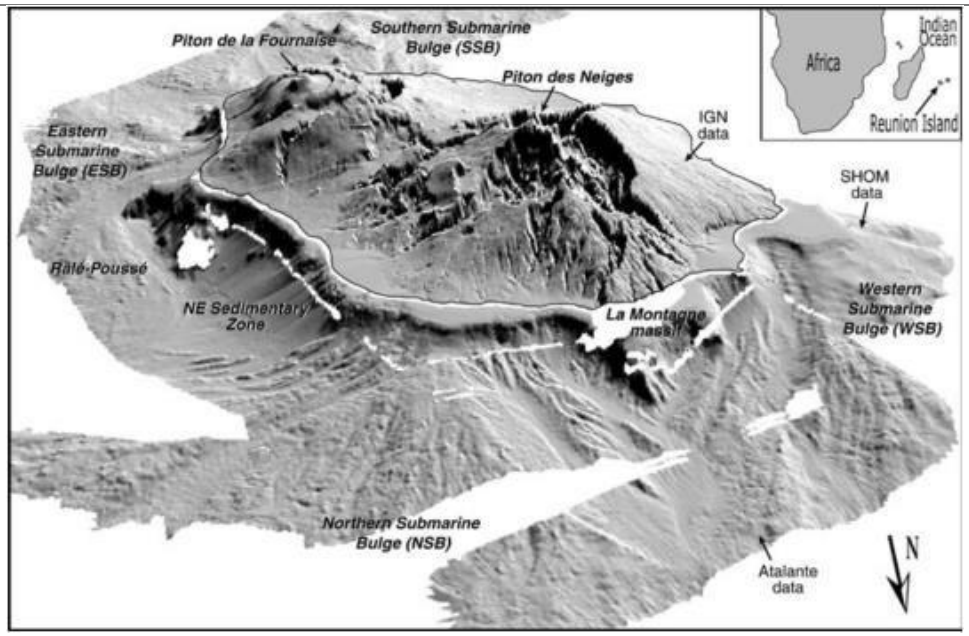

***Figure 13**: Surface and submarine topography of Reunion Island. Vertical scale is exaggerated 4 times (Oehler et al. 2004).*

The magnitude of these mass wasting events are expressed in submarine bulges, fan-shaped underwater debris mounds that are form when masses of sediment are displaced from land to water during an avalanche. An understanding of how these volcano-flanked massive slumps occur is essential because they can affect the volcanoes construction, evolution and eruptive dynamics (Oehler *et al.* 2003). Oehler *et al.* (2003), using multi-beam swathe bathymetry, identified four large submarine bulges that flank the island to the north, south, east and west (Figure 14); the Northern Submarine Bulge (NSB), Southern (SSB) Eastern (ESB) and Western (WSB) respectively (Figure 14). The NSB, SSB and WSB are the product of landslides that have occurred on Piton des Neiges before the last 1 Ma, with another landslide occurring around 430 near the NSB. Labazuy (1996) interprets the ESB as a product of recurrent collapse of the eastern flank of Piton de la Fournaise.

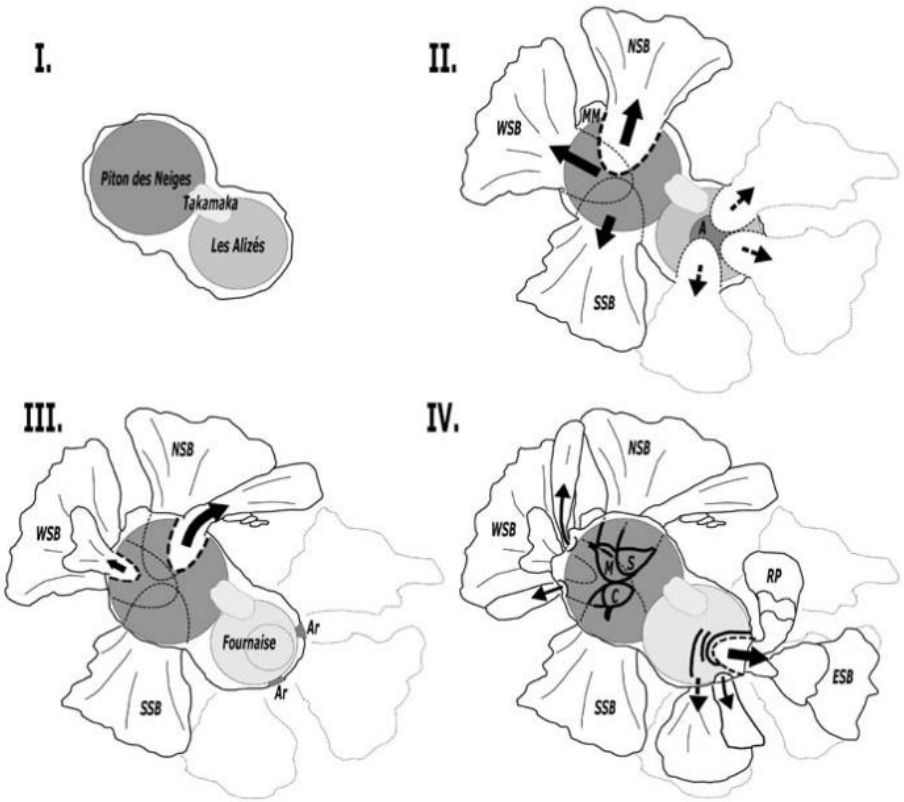

***Figure 14**: Geomorphic evolution of Reunion during the last 2 Ma. NSB: Northern Submarine Bulge, WSB: Western Submarine Bulge, SSB: Southern Submarine Bulge, ESB: Eastern Submarine Bulge. Stage I occurred 2 Ma years ago with the eruption of the Reunion hotspot. Stage II occurred around 1 Ma and had already started mass-wasting events. Stage III landslides occurred around 430 ka ag, around the end of the Oceanite Series. Stage IV occurred 300 ka ago and is responsible for the most eastern submarine deposit. (Oehler* et al. *(2003))*

It is unusual that Reunion Island has experienced such large and pervasive mass flows considering the volcanic shields are gently sloping. However, dyke intrusions, caldera collapse, seismicity, coastal erosion and the over-steepening of slopes by new lava flows may all trigger mass wasting events (Oehler *et al.* (2003). For Reunion Island, Oehler *et al.* (2003) considers the presence of low-strength layers such as hot and ductile cumulates of olivine, hydrothermally altered zones or hyaloclastites within the structure of Piton des Neiges to be the cause of flank landslides.

3.3 Climate

The two volcanoes impart strong climatic and erosional constraints on the local geology due to their high relief and proportionally large surface area. This is apparent when contrasting the annual rainfall (Figure 15) for the eastern and western sides of the island – as much as 6 metres can fall annually on the eastern side, and less than 1 metre on the western side, due to the rain shadow caused by Piton des Neiges.

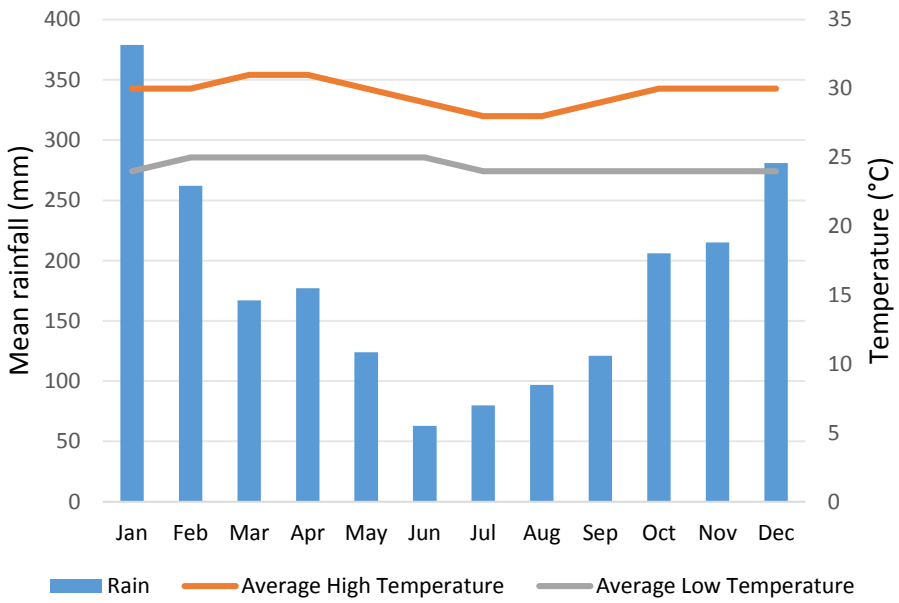

***Figure 15**: Average monthly rainfall and temperatures. Compiled from Meteo France.*

The island experiences wet and dry seasons in summer and winter respectively, and the average high and low monthly temperatures generally stay within 20 to 30°C.

Additionally, the runoff that Reunion Island experiences is as high as 650 to 7000 mm/yr, with large variation caused by the rain-shadow effect that Piton des Neige generates by blocking the easterly trade winds (Louvat and Allegre 1997).

3.4 Chemical weathering at Reunion Island

Louvat and Allegre (1997) investigated weathering rates on Reunion by analysing the chemistry and abundance of dissolved solids in rivers. They found that the dissolved solids were geologically immature and therefore implied that mechanical erosion was the dominant weathering regime at Reunion Island. By solving a mass balance equation for suspended load particles in the rivers of Reunion, the study estimated mechanical erosion rates of 1100-2850 $t/km^2/yr$. This is about 19-54 times higher than the calculated chemical weathering rates of 63-170 $t/km^2/yr$. Since the mechanical weathering rate is far greater than the chemical weathering rate, the erosion regime at Reunion Island is weathering limited. This contrasts to transport-limited regimes where erosion is slow and chemical weathering is controlled by the chemical disequilibrium generated by the sediment flux of rivers and streams. A product of these two weathering regimes is the dramatic difference in CO_2 mineralisation. For weathering-limited regimes like Reunion Island, CO_2 consumption rates are generally much higher than for transport-limited regimes because silicate weathering rates are also increased proportionally in a weathering-limited regime. Interestingly, the calculated CO_2 consumption rate for Hawaii, another weathering-limited regime, is almost three times lower than Reunion Island (Dessert *et al.* 2003). Additionally, on a per square kilometre basis, the CO_2 consumption rate is unusually high for Reunion Island compared to both Hawaii and Iceland (Table 1). One factor that could account for this discrepancy is subsurface chemical weathering (Rad *et al.* 2007).

Rad *et al.* (2007) suggested that the chemical weathering rates determined by Louvat and Allegre were grossly underestimated because chemical weathering caused by subsurface waters was not considered. For basaltic islands, Rad *et el.* (2007) estimate these subsurface chemical weathering rates to be two to five times higher than for rates for surface waters (Table 2). This is particularly evident for Reunion Island, which is estimated to have a subsurface chemical weathering rate three times its surface chemical weathering rate Rad *et el.* (2007). When compared to other basaltic islands such as Hawaii and Iceland, a similar multiple is observed. Rad *et al.* (2007) hypothesise that the cause of this subsurface weathering is debris flows, which form porous surfaces and induce massive water infiltration accelerating the chemical weathering of the subsurface. Since CO_2 consumption increases

with chemical weathering, the total carbon-sequestering ability of basaltic islands has been underestimated by at least two to five times.

***Table 1**: Chemical weathering & CO2 fluxes for basaltic islands*

	Surface area (km^2)	**Surface chemical weathering ($t\ km^{-2}\ yr^{-1}$)**	**Subsurface chemical weathering ($t\ km^{-2}\ yr^{-1}$)**	**Total weathering ($t\ km^{-2}\ yr^{-1}$)**	**CO_2 consumption ($10^6\ mol\ km^{-2}\ yr^{-1}$)**
Reunion	2500	100	295	400	2.26
Hawaii	16700	35	95	130	0.66
Iceland	103000	40	115	160	1.11

Data from Rad *et al.* (2007) and Dessert *et al.* (2003).

Correcting for this 'hidden' chemical weathering, Rad *et al*. (2007) estimate that despite representing only 9% of the total silicate rock area on earth, basaltic islands generate 23 to 31% of the global flux of dissolved silicate rock load in rivers draining to the ocean. This approximation fits well with Desert *et al.* (2003) who attributes one third of the total CO_2 sequestered by silicate weathering to basalt dissolution. Additionally, despite Reunion Island covering <0.002% of the earth's surface area, it is able to sequester 0.09% of the total CO_2 mineralised by silicate weathering. This highlights the importance of climate on the rate of basalt weathering and its role as a carbon sink.

Although the studies of Dessert *et al.* (2003), Louvat and Allegre (1997) and Rad *et al.* (2007) show a strong positive correlation between runoff and weathering rates, other climatic controls such as temperature also need to be considered when studying chemical weathering. In the study by Dessert *et al.* (2003), increasing mean surface temperatures were able to explain 71% of the increase in dissolved bicarbonate in the rivers of basaltic provinces such as Reunion, Java, Iceland, Hawaii and the Deccan Traps. Additionally, increasing runoff rates were again correlated with increasing rates of silicate weathering and CO_2 consumption rates.

In summary, it becomes evident why Reunion Island experiences such high rates of weathering: the ease at which young basalt fractures, the chemical instability of volcanic glass at surface conditions, steep terrain and high annual runoff (Table 2). This results in Reunion Island experiencing surface erosion rates of 470 – 3430 mm/kyr, which are among the highest in the world (Louvat and Allegre 1997).

***Table 2**: Reunion Island Data*

Area	2500 km^2
Climate	Tropical / Oceanic
Average monthly rainfall/temperature (January)	289 mm / 3°C
Average monthly rainfall/temperature (July)	110 mm / 17˚C
Tectonism	Hotspot
Dominant Geology	Tholeiitic to alkaline basalts
Oldest recorded rocks	2 Ma
Topography	Two shield volcanoes; Piton de la Fournaise at 2630m (active) and Piton des Neige at 3070m (extinct)
River discharge rates (rainy season)	10-2500 $m^3 s^{-1}$
Physical erosion rate	1200-9100 t $km^{-2} yr^{-1}$
Chemical erosion rate	400 t $km^{-2} yr^{-1}$
CO_2 consumption rate	1.3-4.4 x 10^6 mol $km^{-2} yr^{-1}$

Data from Louvat and Allegre (1997) and Rad *et al*. (2007)

3.5 Site selection and sampling

Field work and sample collection was conducted by Anthony Dosseto in November 2015. Three weathering profiles were selected (Figure 11) with parent material of different ages in order to establish a chronosequence, and samples were taken throughout each soil horizon. For profile 203 no bedrock was observed and the deepest sample taken is from the C2 horizon. All retrieved samples are listed below in Table 3.

***Table 3**: Soil sample depths, locations and elevations*

Location	*Sample ID*	*Depth in profile (cm)*	*Latitude (S)*	*Longitude (E)*	*Elevation (m)*
Grand Coude	201A	220	21° 03’ 09’’	55° 13’ 26’’	40
	201B	175			
	201C	160			
	201D	135			
	201Dbis	120			
	201E	110			
	201F	100			
	201G	90			
	201H	75			
	201I	53			
	201J	35			
	201K	12			
	201L	0			
Plaine des Fougères	202B	395	21° 00’ 24’’	55° 16’ 44’’	1320
	202C	375			
	202D	305			
	202E	265			
	202F	220			
	202G	140			
	202H	95			
	202I	65			
	202J	0			
Ravine à Malheur	203A	430	20° 55’ 30’’	55° 22’ 50’’	595
	203B	325			
	203C	270			
	203D	190			
	203E	145			
	203F	70			
	203G	0			

Profile 201 is the second oldest soil in the sequence at 70 ka and formed from a basaltic lava flow.

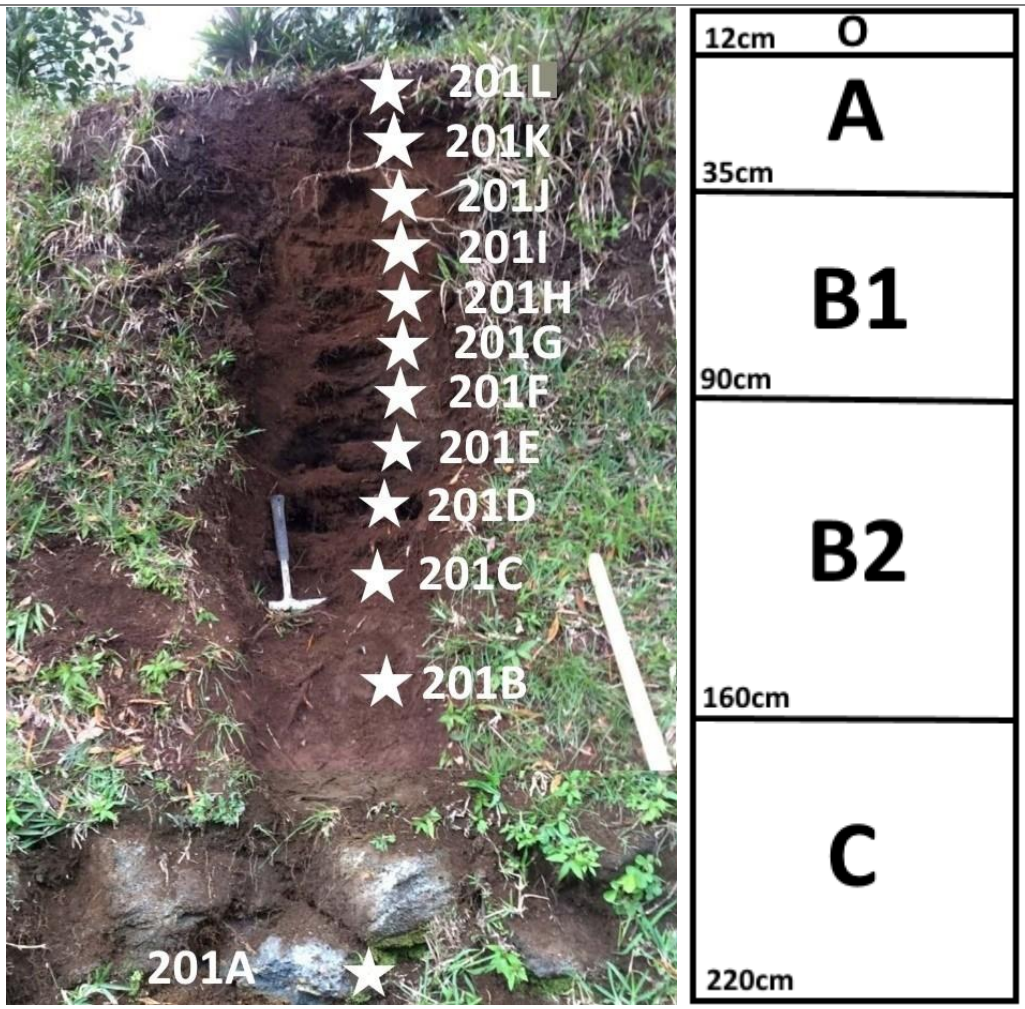

***Figure 16**: Profile 201. Photo taken by A. Dosseto (2015).*

***Table 4**: Horizons descriptions for Profile 201*

Horizon	Soil description
O	Granular structure.
A	Granular structure.
B1	Blocky texture.
B2	Saprolite. Clasts still present.
C	Fresh basaltic rock.

Profile 202 is the youngest soil of the chrononosequence at 20 ka.

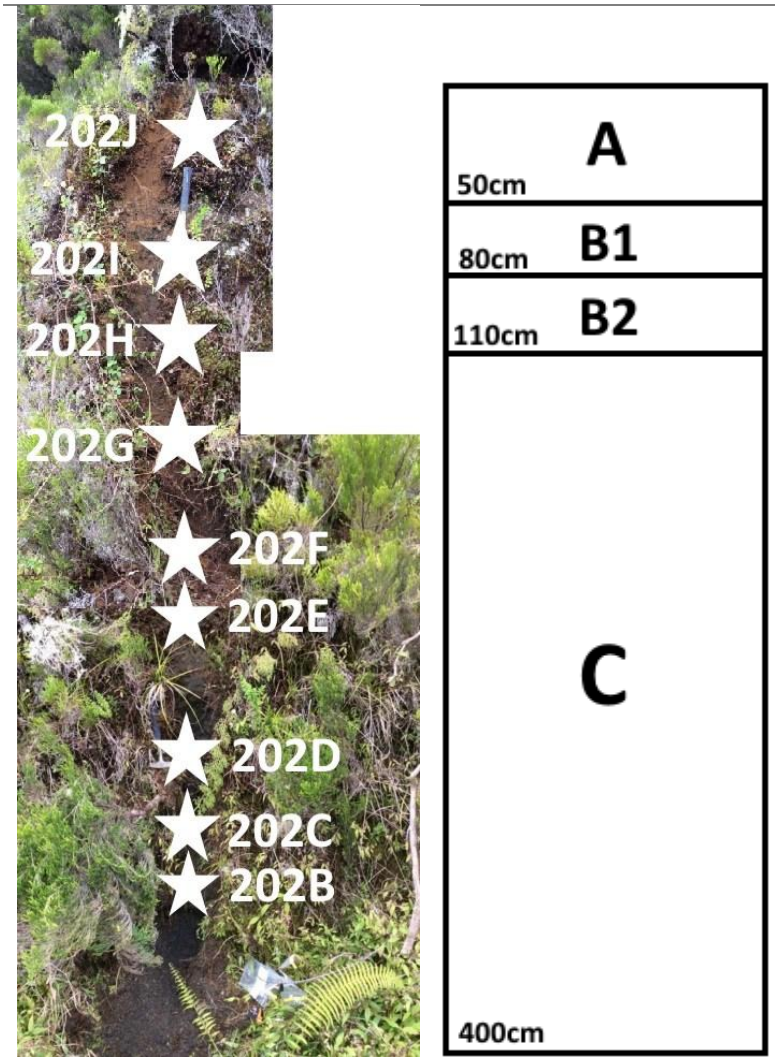

***Figure 17**: Profile 202. Photo taken by A. Dosseto (2015).*

***Table 5**: Horizons descriptions for Profile 202*

Horizon	Description
A	Light brown. Blocky structure.
B1	Light brown to orange.
B2	Clay rich. Red suggests increasing oxidation.
C	Scoria-like material at base of profile. Mottled reds and browns suggests varying oxidation levels.

Profile 203 formed from a basaltic flow and is the oldest profile at 2 Ma.

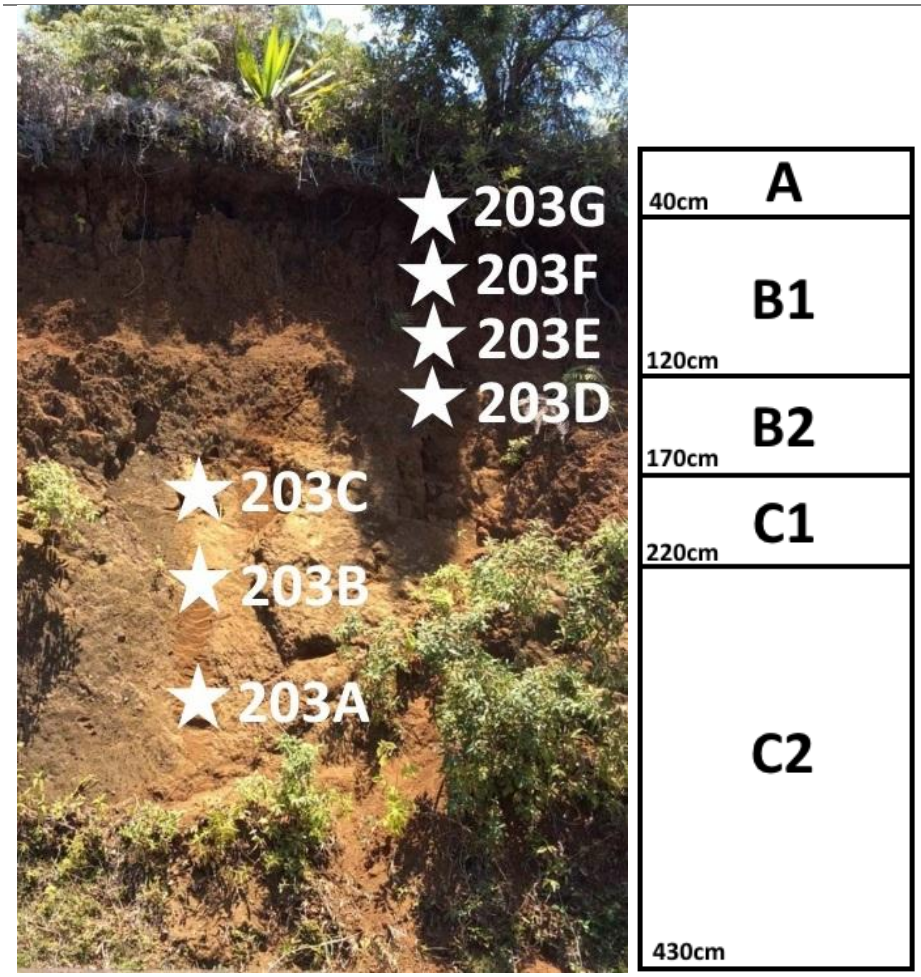

***Figure 18**: Profile 203. Photo taken by A. Dosseto (2015).*

***Table 6**: Horizons descriptions for Profile 203*

Horizon	Description
A	Granular structure.
B1	Blocky structure.
B2	Blocky structure. Absence of roots.
C1	Blocky structure.
C2	Deeply weathered saprolite. Massive structure.

Chapter 4: Methodology

4.1 Sample pre-processing

Thirty samples were dried at 160°C for 2 hours in order to destroy biological contaminants as required by quarantine protocol. A 200g aliquot was taken from each sample and gently crushed using a pestle and mortar to homogenize the soil. Each aliquot was then divided three times using a splitter, with one half of each split fraction used for the subsequent splitting. The final split sample (between 20 – 30g) was then ground into a fine powder using a ring-grinder. The samples were then placed into ceramic crucibles and left in a furnace for 5 hours at 550°C to oxidise organic matter to carbon dioxide.

After the samples cooled, they were placed into individual 50 mL centrifuge tubes and approximately 20 mL of 1M magnesium nitrate was added to each sample. This removed residual exchangeable and non-volatile elements that were bound to organic matter but remained in the soil after combustion. The centrifuge tubes were places on an orbital shaker for 50 minutes and then centrifuged for 20 minutes. The supernatant was then discarded and 14 mL of 18.2M water was placed in each tube and centrifuged for 30 minutes. The previous step was repeated. The centrifuge tubes were then placed into an oven and dried for four days at 60°C. Sample were then individually homogenised using an agate pestle and mortar and stored in individual 15 mL centrifuge tubes.

4.2 Sample digestion

Approximately 30 mg of sample were taken from each centrifuge tube and placed into individual 30 mL PFA vials, weighed and spiked. One mL of trace-grade 48% HF and 0.5 mL of trace-grade 65% HNO_3 were added to each PFA vial and left on a hotplate at 100°C for 18h with the vials closed. The evaporation of HF inside each closed vial ensured complete dissolution of silicate minerals. Once dissolution was complete, the caps were taken off the vials and the samples left on the hotplate to dry down. Upon dry down, each sample was treated with 1.5mL of 30% trace- grade HCl and 0.5 mL of 65% trace-grade HNO_3 (i.e. aqua

regia) and left on the hotplate at 100°C with the vials closed for a further 18h. This ensured complete dissolution of base metals.

Once dissolution was complete, the caps were taken off each of the vials and the samples were dried down. Each sample was then treated with 0.5mL of trace-grade 65% HNO_3 and left to evaporate on the hotplate at 80°C. This was repeated upon dry down. All samples were then treated with 2 mL of 1.5M trace-grade HNO_3 and left on the hotplate at 100°C for 2h with the caps on the vials. The solutions were then weighed and placed in clean 15 mL centrifuge tubes and were centrifuged for 5 minutes at 4000 rpm.

4.3 Petrography

Mineralogy was visually identified using petrographic microscopes using both polar and cross polar filters. Thin sections of the soil samples were prepared by placing the soil into an epoxy resin which was allowed to harden and then ground to a thickness of 30 μm. The thin sections were then mounted onto a microscopic slide for observation. Interference colours were used in conjunction with other optical diagnostic properties such as cleavage and twinning, to identify minerals.

4.4 Grain size analysis

The distribution of grain sizes in each sample was measured using a Malvern Mastersizer 2000. Approximately 10 g of sediment was sonicated for 20 seconds before analysis to break up clasts. The average of three measurements of grain size distribution was then calculated and produced as a proportion of sand (2000 – 63 μm), silt (63 – 4 μm) and clay (< 4 μm) clasts.

4.5 Mineralogy

Abundances of minerals in each sample was measured quantitatively using X-Ray Diffraction (XRD). XRD exploits the similar wavelength of X-rays with the spacing of atoms in minerals (1-2 angstroms) to identify minerals. Therefore, when incident X-ray radiation interacts with a crystal such that it produces constructive interference, the diffracted radiation can be detected. The weight proportion of each mineral is then calculated by the size and location of the produced peaks. Since the reflection of X-rays is possible only if the crystal is oriented such that constructive interference is produced, samples are ground into a powder so that a wide range of orientations are sampled. The samples from Reunion Island were analysed using the powder method. Results were processed using Siroquant XRD software with Chi-squared (i.e. goodness of fit) values < 5. Three samples were replicated in order to assess reproducibility:

***Table 7**: XRD replicate reproducibility*

	Olivine (wt%)	**Plagioclase (wt%)**	**Gibbsite (wt%)**
201B #1	24.7	14.4	4.3
201B #2	22.6	14.2	4.8
Abs Difference	**8.5%**	**1.4%**	**11.6%**
202C #1	6.1	38.2	0
202C #2	5.3	47.4	0.2
Abs Difference	**13%**	**24%**	**13%**
203A #1	3.5	1.0	1.5
203A #2	0.9	1.3	1.7
Abs Difference	**74%**	**74%**	**74%**

The absolute difference between samples is defined as:

$$\left|\frac{sample\ \#1 - sample\ \#2}{sample\ \#1}\right| \ x\ 100\%$$

Reproducibility is acceptable. The low values of 203A (<5%) minimise the effect of the large absolute difference.

4.6 Major and trace elements

Major and trace element concentrations were determined using quadrupole inductively coupled plasma mass spectrometry (Q-ICP-MS). Aliquots of 0.1 mL and 0.001mL were extracted from each centrifuge tube and diluted to 10 mL with 0.3M trace-grade HNO_3 for major and trace element analysis, respectively. Major elements were analysed on the 1:10,000 dilutions and trace elements on the 1:100 dilutions in order to constrain the concentrations to the technical limits of the Q-ICP-MS.

Quality assurance measures included the use of an internal standard to account for instrument drift, synthetic standards with known concentrations of the analytes (71A+B) (tested every 10^{th} sample) and rock standards (QLO-1) to assess the accuracy of the dissolution and analysis protocol (Table 9) and blanks (tested every 10^{th} sample) to assess contamination during sample preparation and analysis (Table 8). Total procedure blanks were prepared but could not be quantified since the concentrations for all elements were below the detection limit of the Q-ICP-MS. This occurred because the blanks were diluted to a 1:100 solution by mistake.

***Table 8**: Q-ICP-MS quality assurance parameters*

Major elements	Na, Mg, Ti, Mn
Trace elements	Sr, Rb, Ba, Cs, Nb, Ta, Zr, Cu, La, Ce, Nd, Sm, Eu, Yb, U, Th
Solution matrix	0.3M trace-grade HNO_3
Internal standard	50 ppb In, Sc, Bi
Calibration standards	0.05, 0.1, 0.5, 1, 5, 10, 50, 100, 200, 500 ppb 71A+B
Synthetic standard	10 ppb 71A+B (containing the major and trace elements listed above)
Rock standard	USGS Quartz Latite, QLO-1

***Table 9**: Q-ICP-MS rock standard results*

Element	Recommended value (ug/g) (QLO-1)	Recorded value (ug/g) QLO-1 #1	Recorded value (ug/g) QLO-1 #2
Na_2O	4.20 ± 0.13 %	4.39 ± 0.20 %	3.80 ± 0.07 %
Ba	1370 ± 80	1410 ± 64	976 ± 41
Ce	54 ± 6	61 ± 2.1	53 ± 2.2
Cs	1.8 ± 0.2	1.4 ± 0.05	0.97 ± 0.05
Cu	29 ± 3	25 ± 0.8	25 ± 1.3
Eu	1.43 ± 0.12	1.53 ± 0.1	1.34 ± 0.1
La	27 ± 2	27 ± 0.5	25 ± 1.4
Nb	10 ± 1.3	8.5 ± 0.3	8.7 ± 0.4
Nd	26	23 ± 1.0	21 ± 0.4
Rb	74 ± 3	64 ± 2.2	62 ± 2.0
Sm	4.9 ± 0.2	4.6 ± 0.1	4.1 ± 0.2
Sr	340 ± 12	342 ± 14	289 ± 14
Ta	0.82 ± 0.1	0.74 ± 0.1	0.73 ± 0.1
Th	4.5 ± 0.5	4.3 ± 0.2	3.6 ± 0.1
U	1.9 ± 0.12	1.68 ± 0.12	1.72 ± 0.1
Yb	2.3 ± 0.2	2.3 ± 0.1	2.1 ± 0.1
Zr	185 ± 16	187 ± 9.1	189 ± 8.1

Green = within recommended value, Red = outside recommended value

The majority of the elements pass for QLO-1 #1, but fail for QLO-1 #2. Of those that have failed, most are within 20% of the recommended value. This is a poor result, and may reflect that material was not completely dissolved during the dissolution protocol.

Replicates were analysed for three samples and to check for reproducibility. Replicate analysis for rock standard QLO-1 is included for comparison.

***Table 10**: Q-ICP-MS replicate results*

Lab number	Rb	Ba	Cu	Eu	Th
201B #1	2.00 ± 0.13	28.5 ± 1.48	69.0 ± 4.34	1.52 ± 0.06	1.62 ± 0.09
201B #2	2.91 ± 0.06	40 ± 1.20	98.1 ± 2.51	2.11 ± 0.06	1.74 ± 0.05
Abs difference	**46%**	**40%**	**42%**	**39%**	**7.4%**
202C #1	31.3 ± 2.06	458 ± 30.7	16.1 ± 0.95	4.05 ± 0.25	3.81 ± 0.25
202C #2	36.9 ± 1.79	487 ± 39.6	19.5 ± 0.67	4.67 ± 0.12	4.39 ± 0.21
Abs difference	**18%**	**6.3%**	**21%**	**15%**	**15%**
203A #1	0.36 ± 0.01	976 ± 18.1	138 ± 1.86	4.06 ± 0.07	4.20 ± 0.18
203A #2	0.51 ± 0.03	608 ± 25.3	152 ± 6.87	4.51 ± 0.32	4.59 ± 0.24
Abs difference	**42%**	**38%**	**10%**	**11%**	**9.3%**
QLO-1 #1	64.0 ± 2.2	1410 ± 64.3	24.6 ± 0.79	1.53 ± 0.06	4.28 ± 0.19
QLO-1 #2	62.0 ± 2.0	976 ± 40.7	25.4 ± 1.25	1.34 ± 0.03	3.60 ± 0.10
Abs difference	**15%**	**31%**	**3.3%**	**12%**	**16%**

Reproducibility is poor, with an average absolute difference between results of 34.9% for Profile 201, 15.2% for Profile 202 and 22% for Profile 203.

Except for the rock standard (QLO-1), batch #2 has concentrations that are systematically higher than batch #1 for the three samples. This may indicate that batch #1 was incompletely dissolved during the dissolution protocol.

Chapter 5 - Results

5.1 Characterisation of the Reunion Island basalts

Considering the central importance of parent material lithology on soil evolution, it is worth defining the characteristics of the three basalts that make up the Reunion chronosequence. Using the Th/Nb proxy devised by Pearce (2008), the basalts can be 'fingerprinted' and check whther they have been derived not only from a common mantle source, but also the previously analysed basalts on Reunion Island (Figure 19). Basalts that plot at high Th/Yb and Nb/Yb ratios indicate they contain a recycled crustal component (because Th is enriched in the continental crust).

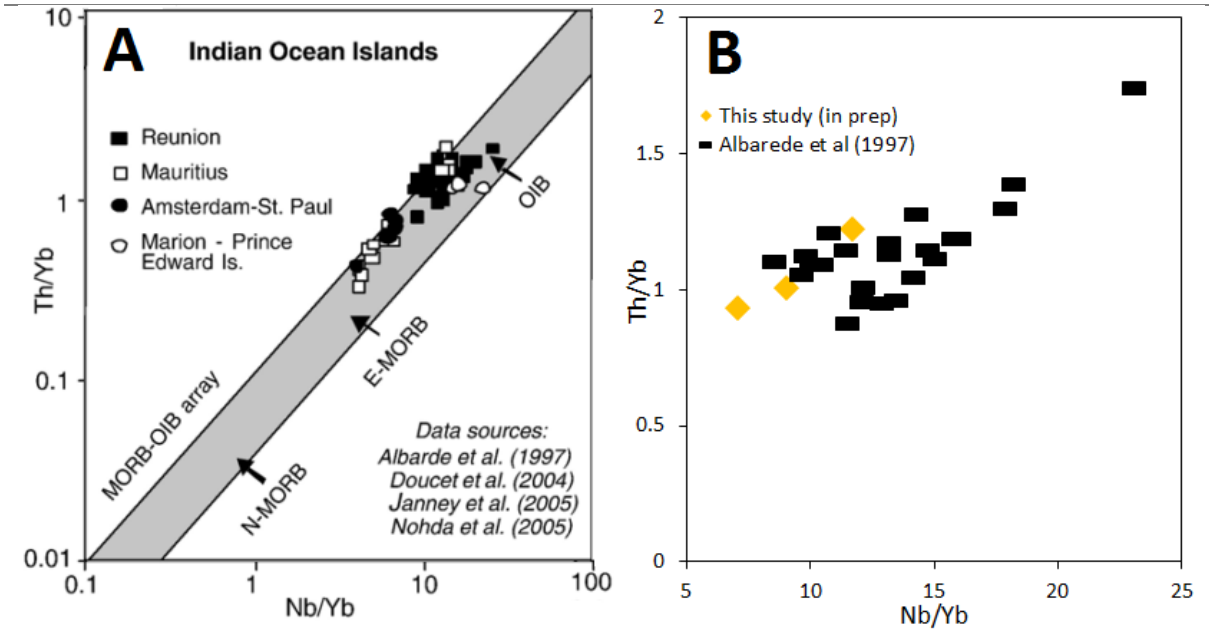

Figure 19: *Inset A: Characterisation of the Reunion basalts using Th/Yb and Nb/Yb ratios developed by Pearce (2008). Inset B: Our results fall within the intraplate ocean island basalt (OIB) region. Results are similar to those derived from Albarede et al (1997) and suggest the basalts on Reunion formed from a common mantle source. The relatively high Th/Yb ratio suggests the melt was located deeper and contains more recycled crustal material compared MORB basalts produced from shallower melts. Adapted from Pearce (2008).*

The three basalts from Profiles 201, 202 and 203 share similar Th/Yb ratios, and plot within the intra-oceanic basalt region. This suggests the magmas formed from a common mantle source and crystallised under similar conditions. Additionally, our results have a smaller range in Nb/Yb ratios compared to the range determined by Albarede *et al.* (1997), which further supports this hypothesis. The implication is that the basalts should be chemically homogenous, even though they differ in age by three orders of magnitude.

5.2 Mineralogy – Thin sections

Thin sections of all samples were prepared and examined under plane polarised light (PPL) and cross-polarised light (XPL). For Profiles 202 (20 ka) and 201 (70 ka) there is a progression from fresh to weathered primary minerals with decreasing soil depth. The main phases observed in these profiles were olivine, pyroxene and plagioclase. Since Profile 203 (2 Ma) is intensely weathered, most of the primary minerals have been lost or altered into secondary phases. This makes determination difficult for the few visible minerals that remain.

In Profile 202 (20 ka) olivine, pyroxene and plagioclase are the main phases observed. In Figure 20, plagioclase has already started to weather in the basaltic parent material. Further up the profile, olivine has started to weather with its cracks filled with a secondary product.

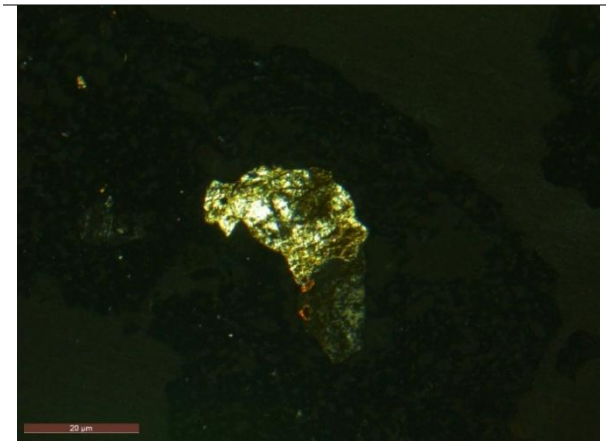

***Figure 20**: Sample 202B under XPL. Plagioclase. Magnification of 10x*

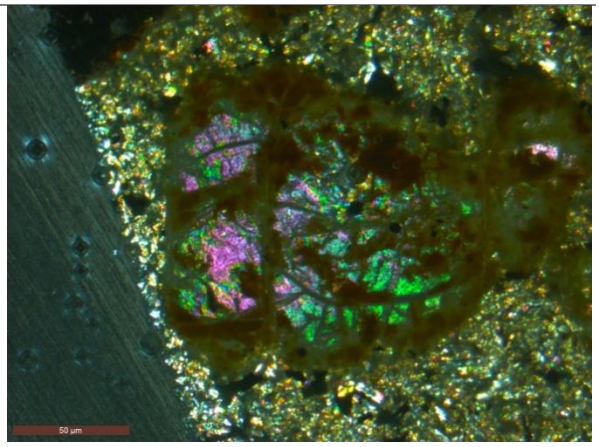

***Figure 21**: Sample 202D under XPL. Olivine. Magnification of 10x*

In Profile 201 (70 ka) olivine and pyroxene are the dominant phases. In Figure 22, fresh, euhedral olivine that forms the basaltic parent material is observed. Up the profile in in Figure 23, olivine is starting to degrade by chemical weathering. In this example, olivine is degrading into a secondary product, possibly goethite.

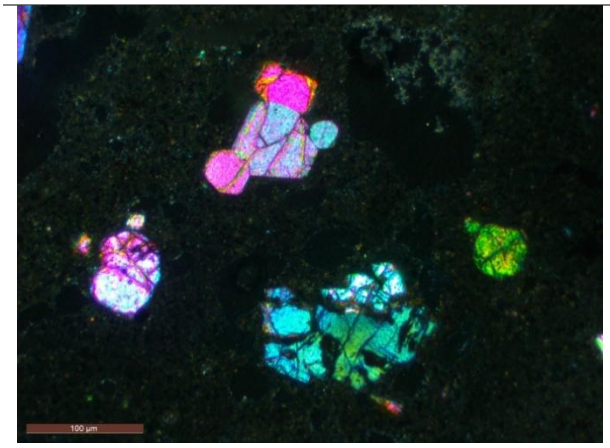

***Figure 22**: Sample 201A under XPL. Fresh olivine Magnification of 4x.*

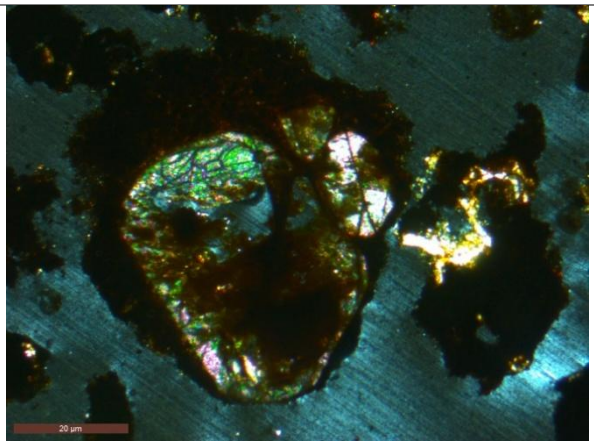

***Figure 23**: Sample 201F under XPL. Weathered olivine. Magnification of 10x*

In Profile 203 (2 Ma), the main primary phase is relict pyroxene. Nearly all of the primary minerals have disappeared, and the soil is dominated by both angular soil aggregates (Figure 24) and fine groundmass (Figure 25). XRD results indicate that secondary phases such as clay dominate the soil, but we cannot identify these minerals under PPL or XPL.

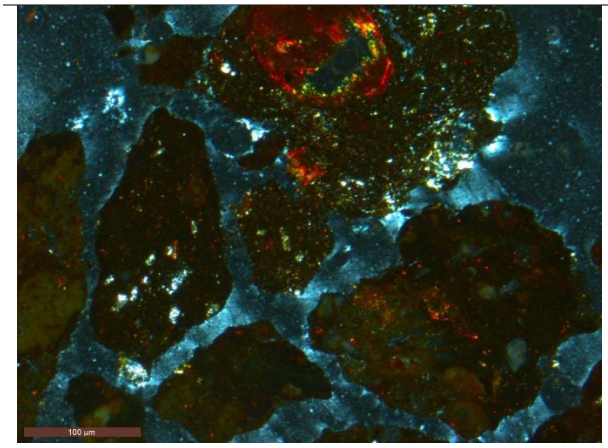

***Figure 24**: Sample 203B under XPL. Soil aggregates. Magnification of 4x*

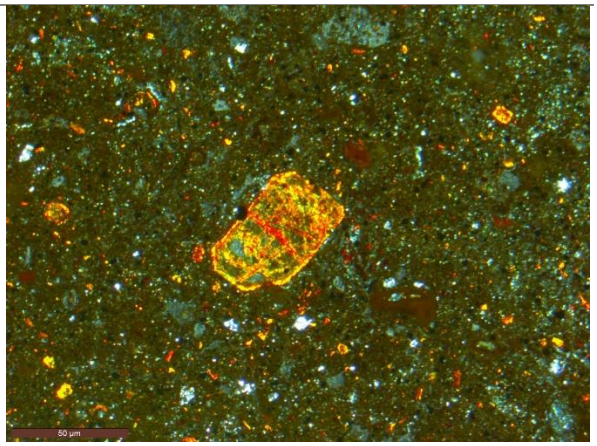

***Figure 25**: Sample 203C under XPL. Pyroxene. Magnification of 20x*

5.3 Grain size analysis

When comparing the profiles developed on the three basalts there is a rapid decrease, then gradual increase in mean grain size over 2 Ma (Figure 26). Within the profiles, the mean particle size decreases with time in the bottom half of the profiles, but increases over time in the top half of the profiles (Figure 27).

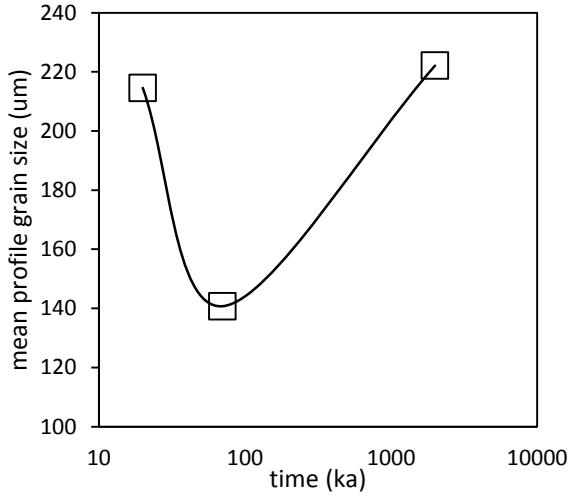

***Figure 26**: Grain size vs. profile age*

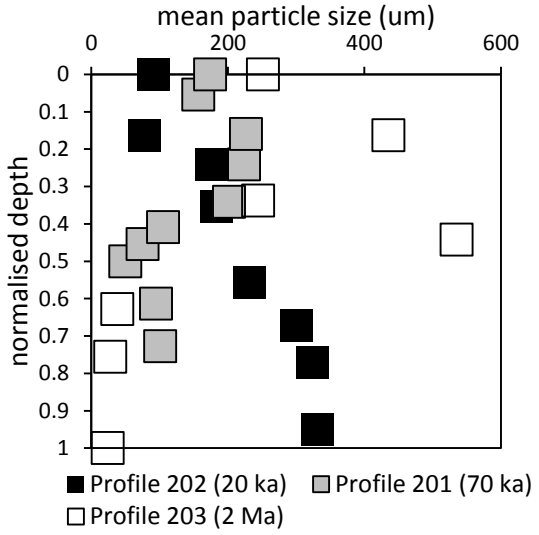

***Figure 27**: Vertical variation in grain size.*

The rapid decline in mean particle size from 220 μm to 140 μm in the 20 and 70 ka profile can be explained by the dual action of mineral dissolution and dust deposition. Since mineral dissolution will reduce the average size of particles as secondary clays are formed, and atmospheric dust is generally no greater than silt size (Simonson 1995), both processes can account for this decline. After 2 Ma, however, the average particle size returns to its initial value of approximately 220 μm. Considering the source of dust could be as far away as Australia, and the average atmospheric lifetime of particles greater than 10 μm is less than a day (Tegen 1996), dust deposition is unlikely to be responsible for this increase in mean grain size between the 70 ka and 2 Ma profiles.

Within the profiles, there is a systematic progression towards clay-sized particles in the bottom half of the profiles over time. Again, this can be explained on account of bedrock weathering, mineral dissolution and the formation of clays which all reduce average particle size. However, in the top half of the profiles, the opposite is observed; mean particle size actually increases over time. If the initial assumption is correct - that dust was partly responsible for the reduction in grain size between the 20 and 70 ka profiles – then there should be a reduction in grain size at the surface. Since atmospheric dust is too fine-grained to account for this increase, there is some process eroding or weathering fine grained material at the expense of larger particles. Dissolution of fine-grained secondary minerals may be able to explain this relative increase in grain size at the surface of the 70 ka and 2 Ma profiles.

5.4 Primary phases

XRD results indicate that the parent material is dominated by olivine, pyroxene, plagioclase and K-feldspar and together make up more than 90% of it by mass. The remaining 10% consists of a mixture of illmenite, magnesite and muscovite and due to their being below detection limit, do not form part of this discussion.

All three profiles show a loss of primary minerals with decreasing depth (Figure 29). This is likely a result of the increasingly acidic, oxic and moist conditions caused by plant respiration, aeration and rain percolation which reach a maximum at the surface. Mineral dissolution is accelerated under such conditions and can account for this loss of primary minerals with decreasing depth. Plagioclase is weathered most rapidly, with 70% lost between the 20 and 70 ka profiles (Figure 28). The other primary minerals are lost more gradually during this time, and by 2 Ma, no more than 5% of the soil mass consists of any one primary phase.

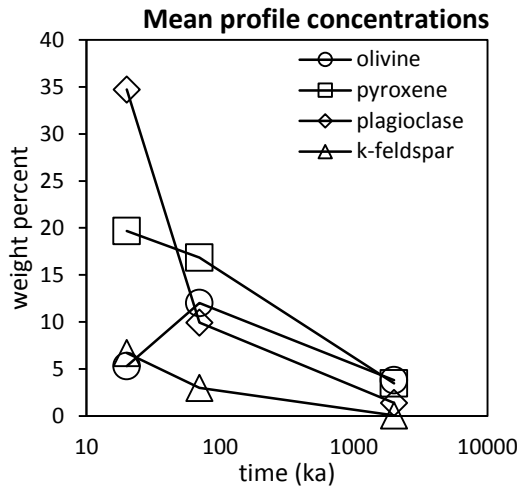

***Figure 28**: Average profile concentrations of primary minerals as a function of soil profile age.*

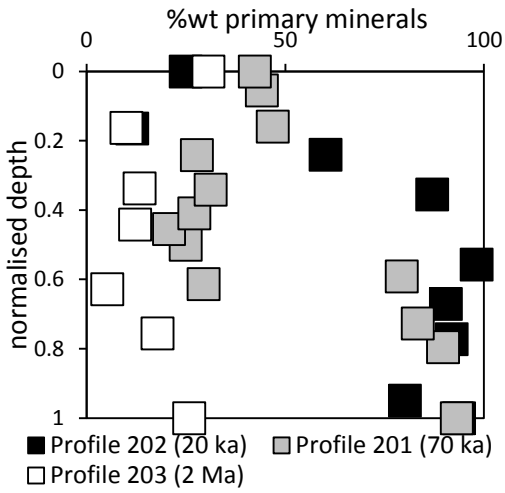

***Figure 29**: Average concentration of primary minerals as a function of normalised soil depth determined by XRD. Here, primary minerals are defined as olivine, pyroxene, plagioclase and K-feldspar.*

Olivine and pyroxene, which are the two most weatherable minerals on account of their unlinked silica tetrahedra (Goldich 1938). Figures 30 and 31 show the loss of these minerals reaches a maximum towards the surface, and by 2 Ma, both of these phases have been completely weathered and lost from the soil profile.

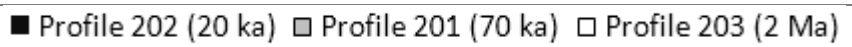

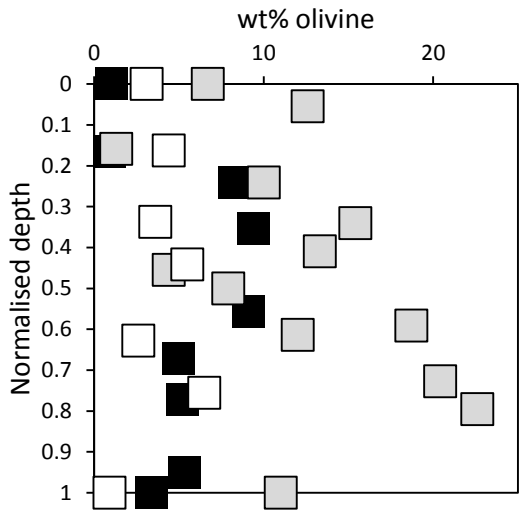

***Figure 30**: Mineral distribution profile for olivine.*

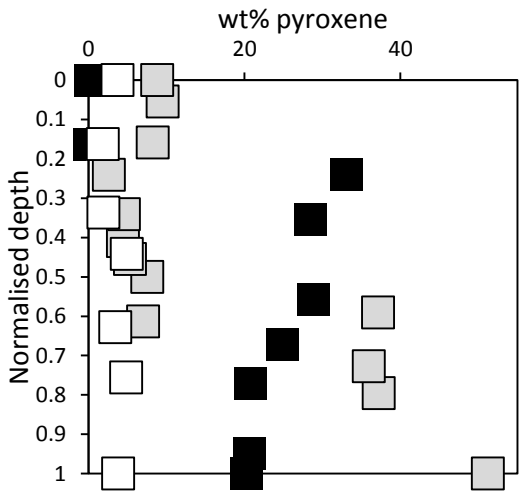

***Figure 31**: Mineral distribution profile for pyroxene.*

Plagioclase and K-feldspar, the other two primary minerals present at Reunion Island, show a similar depth-dependent trend, with maximum loss occurring at the surface. Figure 32 suggests loss of plagioclase is systematic both with decreasing depth and increasing soil age, with the greatest loss occurring between the 20 and 70 ka profiles. This suggests the effects of chemical weathering is most intense during the initial stages of soil development, and gradually reduces over time. The distribution of K-feldspar in Figure 33 on the other hand shows no clear trend with soil depth, and by 2 Ma, is completely lost from the soil profile.

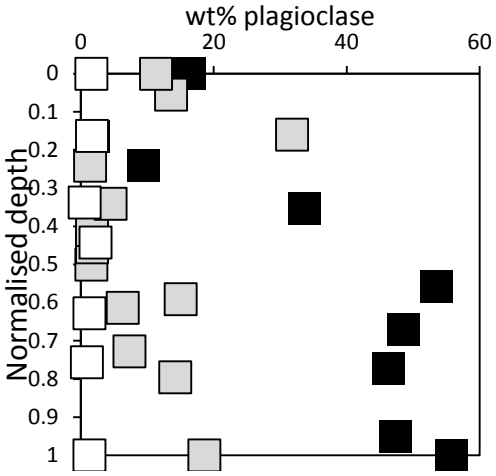

***Figure 32**: Mineral distribution profile of plagioclase.*

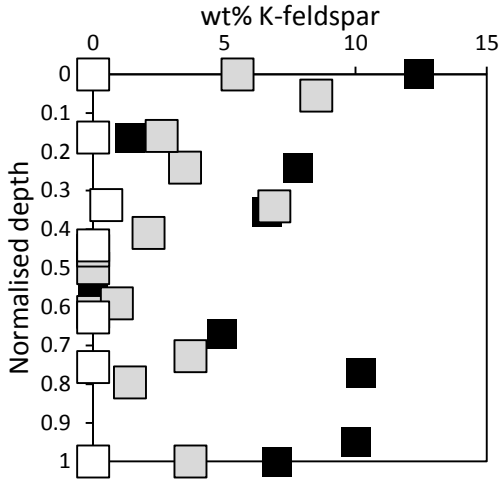

***Figure 33**: Mineral distribution profile of K-feldspar.*

5.5 Secondary phases

The secondary phases detected by XRD include gibbsite, kaolinite, illite, halloysite and goethite. Within the profiles, there are only a few systematic trends. Figure 34 shows that the abundance of goethite, kaolinite and illite all generally increase with decreasing depth, likely as a result of mineral dissolution intensifying here. Of these secondary phases, gibbsite and halloysite dominate the 70 ka and 2 Ma profiles, with halloysite rapidly forming and becoming the dominant phase in the 2 Ma profile (Figure 34).

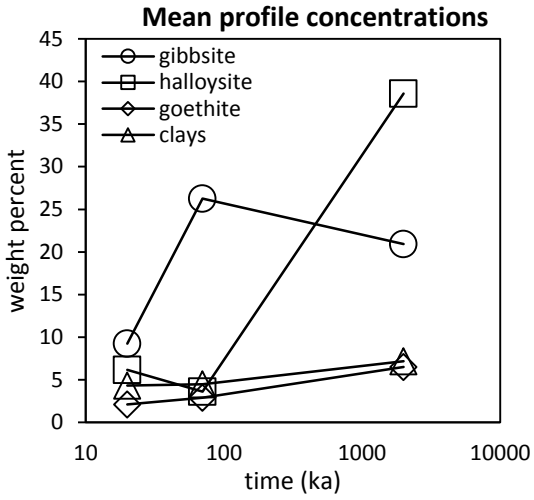

***Figure 34**: Average profile concentrations of secondary minerals as a function of soil profile age.*

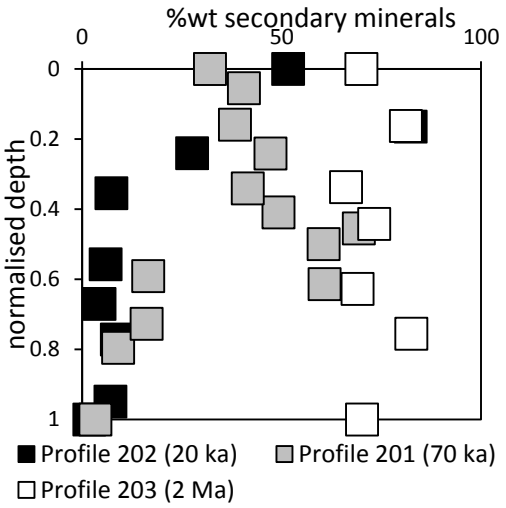

***Figure 35**: Average concentration of secondary minerals throughout the profiles*

Specifically, the 70 ka profile is dominated by gibbsite and forms up to 40% of the soil mass in the B2 horizon, while halloysite is the major phase in the 2 Ma profile and forms up to 60% by mass in the C2 horizon (Figures 36 and 37). In Figure 36 gibbsite does not form in appreciable amounts until at least 70 ka of soil development, where it peaks in the middle of the profile. Meanwhile, in the 2 Ma profile, Figure 37 shows that halloysite peaks in the upper and lower parts of the profile, perhaps because there is an excess of Si over Al in these areas.

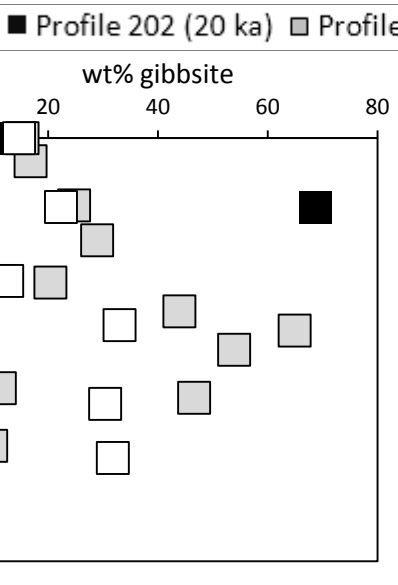

***Figure 36**: Mineral distribution profile of gibbsite.*

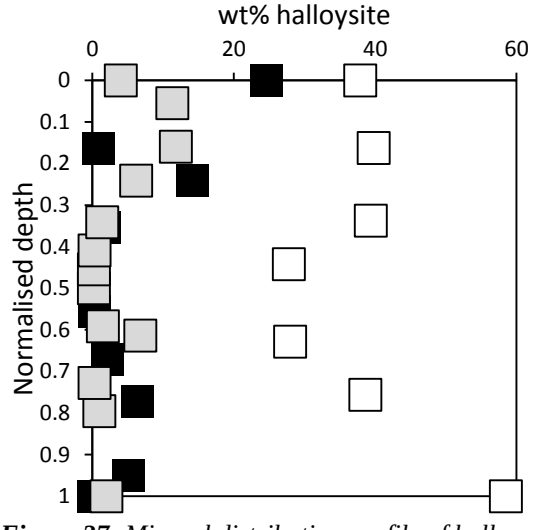

***Figure 37**: Mineral distribution profile of halloysite.*

The preferential formation of halloysite over gibbsite in the 2 Ma profile is unusual because silica is leached fairly quickly, especially in high rainfall environments like Reunion Island. In such an environment it is expected that the aluminium-dominated phase, gibbsite, should dominate the oldest soil as silica is progressively leached away (Kleber *et al.* 2007).

The other secondary phases present at Reunion Island, goethite, kaolinite and illite form only minor components of the soils. The vertical distribution of these phases, particularly goethite, is much more systematic than either gibbsite or halloysite. Figure 38 shows that goethite concentration in particular increases with both decreasing depth and soil age, probably as a result of increasingly oxidising conditions on approach to the surface, the effect of which generally increases over time (Velbel 1993). Like the other secondary phases, Figure 39 shows the abundance of kaolinite and illite increases with decreasing depth and likely reflects enhanced mineral dissolution and secondary mineral precipitation on approach to the surface

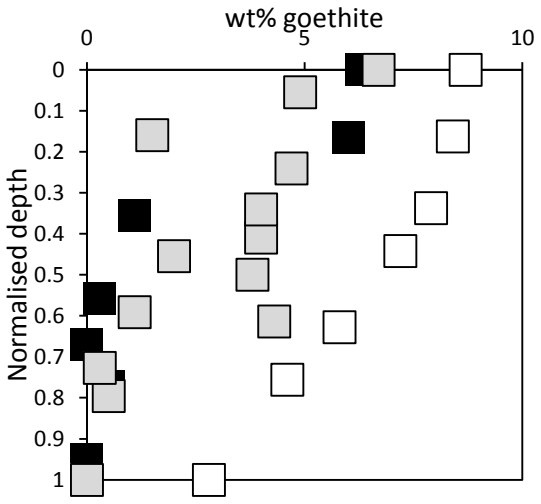

***Figure 38**: Mineral distribution profile of goethite.*

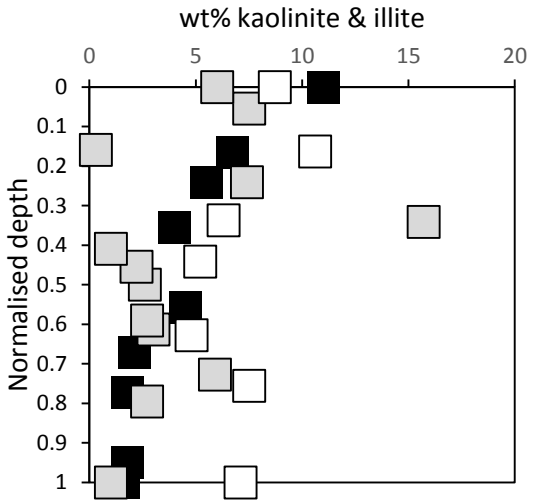

***Figure 39**: Mineral distribution profile of kaolinite and illite.*

5.6 Major and trace elements

Mass transfer coefficients (Brantley *et al.* 2007) were calculated for a suite of elements (Table 11) for each sample across the chronosequence and graphed against normalised soil profile thickness so that profiles of different thickness could be compared. To quantify how changes in element behaviour change over time, mass transfer coefficients for each soil profile for each soil sample. This produces an element profile that can reveal the soil forming factors that affect soil development such as mineral dissolution, dust deposition and organic matter breakdown. Since elements of identical periodic groups tend to show similar geochemical behaviour (Ryan 2014), the element profiles are discussed according to their periodic group. At the start of each section, the average mass transfer coefficient of all samples within a profile is graphed as a function of soil age that changes in element mobility can be generalised for each element in the profile. Before the main results however, a brief overview of how mass transfer coefficients were calculated and the justification for the selection of Nb as the index immobile element will be discussed.

***Table 11**: Selected analytes for major and trace elements*

	Alkalis	**Alkaline Earths**	**Transition metals**	**REE**	**Actinides**
Major elements	Na	Mg	Ti, Mn, Cu	n/a	n/a
Trace elements	Rb, Cs	Sr, Ba	Zr, Ta, Nb	La, Ce, Nd, Sm, Eu, Yb	U, Th

5.6.1 Calculating the mass-transfer coefficient τ

Using the mass transfer equation developed by Brimhall and Dietrich (1987), the mobility of elements in the regolith can be quantified (Equation 8). By normalising the concentration of a given element in the regolith ($C_{j,w}$) against the concentration of that element in the parent material ($C_{j,p}$) a profile of how the given element varies with depth is produced. Therefore, decreases in ($C_{j,w}$)/($C_{j,p}$) indicate loss of that element in the regolith, while increases indicate gains. However, this ratio can vary without the loss or gain of the given element because the

concentration of an element can change as the density of the soil changes. In order to correct for this change in soil density, the concentration of the given element in both the regolith and the parent material must be normalised against an immobile element, ($C_{i,}$). This means that increases in the given element throughout the regolith ($C_{j,w}$) reflect the actual gain of that element, while decreases reflect an actual loss.

$$\tau_{i,j} = \frac{(\frac{C_{j,w}}{C_{i,w}})}{(\frac{C_{j,p}}{C_{i,p}})} - 1 \qquad \textit{Equation 8}$$

For each soil sample, the concentration of each given element is normalised against the concentration of Nb in the parent material of each profile, as Nb is defined as the index immobile element at Reunion Island. The parent material is the deepest sample taken from each profile, i.e. samples 201A, 202B and 203A.

The use of the mass transfer equation requires an immobile element in order to assess the migration of other elements on a quantitative basis. Accordingly, the element must have very low aqueous solubility, occur mainly in weathering-resistant minerals and have a homogenous distribution in the parent rock (Nesbitt 1979). The refractory elements Ti, Zr, Nb and Ta generally show these characteristics, but depending on the climatic regime, can become semi-mobile (e.g. Kurtz *et al.* 2000). In order to assess their mobility, the concentrations of the elements in each of the soil profiles are graphed against each other. For perfectly immobile elements, the ratio of their concentrations should remain constant both throughout space (vertically in the soil profile) and time (across the chronosequence) and so the correlation coefficient for two perfectly immobile elements should approach 1. For the soils at Reunion Island, Ti, Zr, Nb and Ta were analysed. The results indicate that in order of decreasing immobility, Nb = Ta > Zr > Ti (Figures 40-43).

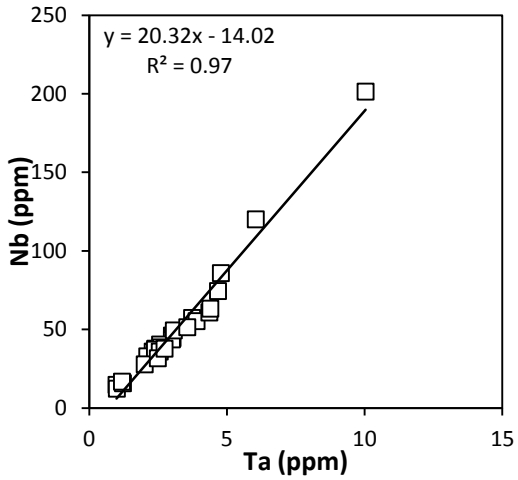

***Figure 40**: Least squares analysis for Nb vs Ta*

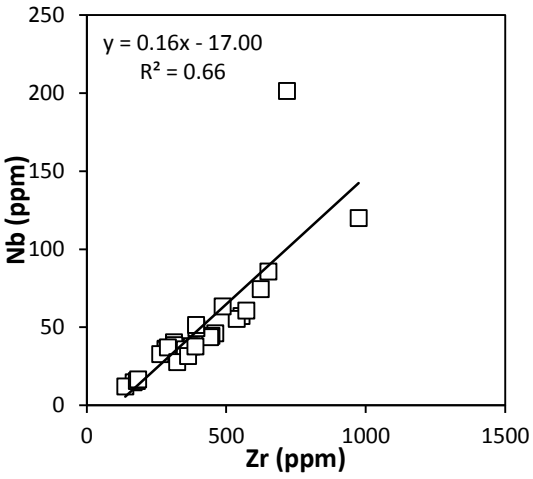

***Figure 41**: Least squares analysis for Nb vs Zr*

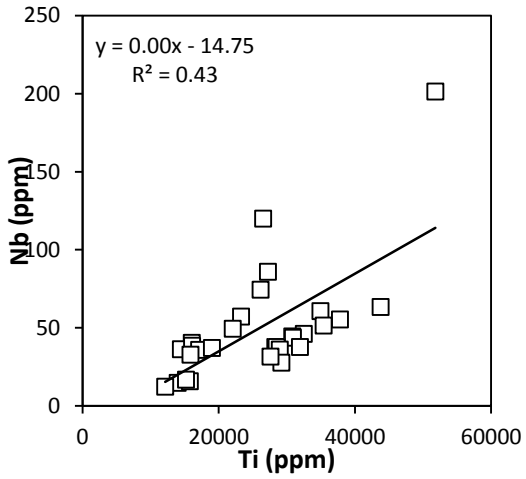

***Figure 42**: Least squares analysis for Nb vs Ti*

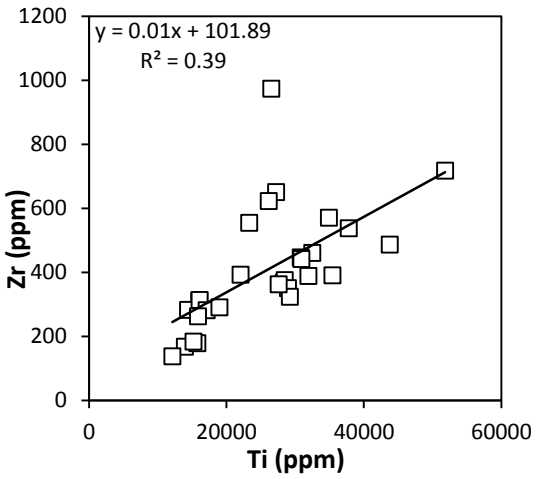

***Figure 43**: Least squares analysis for Zr vs Ti*

Since both Nb and Ta display almost identical immobility, the choice of Nb over Ta as the index immobile element is somewhat arbitrary. For the other candidates, the outlier in Figure 41 is a result of the concentration of Nb being anomalously high in sample 202J. Otherwise, Zr is mostly immobile. The most mobile element of the group, Ti is a surprising result because it is often assumed to be a reliable index immobile element (e.g. Huang *et al.* 2004).

5.6.2 Alkali metals (Na, Rb, Cs)

In the 20 ka profile, Na (Figure 44) remains largely immobile in the bottom half of the profile, but approaches 100% depletion towards the surface. In the 70 ka profile, Na approaches complete loss by the bottom 40% of the profile, but the top 60% shows a relative gain of 15%. In the 2 Ma profile, all of the Na is lost throughout the entire profile. Similarly, Rb (Figure 45) remains largely immobile in the bottom half of the 20 ka profile, but approaches 100% depletion towards the surface. In the 70 ka profile, Rb becomes 100% depleted half way up the profile, but shows a larger relative gain of 70% on approach to the surface. About 90% of the Rb is lost throughout the 2 Ma profile, with slightly less loss occurring in the top 50% of the profile. Meanwhile, Cs (Figure 46) remains immobile in the bottom 60% of the 20 ka profile, but becomes 100% depleted on approach to the surface. In the 70 ka profile, Cs is enriched compared to the parent material, but becomes depleted by 60% half-way up the profile. From here, Cs is progressively added on approach to the surface by 300%. In the 2 Ma profile, about 30% of the Cs is lost in the bottom 40% of the profile, while it remains enriched by about 100% in the top 60%.

Over time, the average concentrations of each element in each of the soil profiles (Figure 47) show that by 20 ka, 40% of the original Na, 30% of the original Rb and 25% of the original Cs is lost. By 70 ka, nearly 80% of Na and 49% of Rb is lost, while Cs experiences a relative gain of 120%. In the 2 Ma profile, 99% of Na and 86% of Rb has been lost, and while Cs experiences a relative loss of 26% during this time, it still enriched by 71% compared to the parent material.

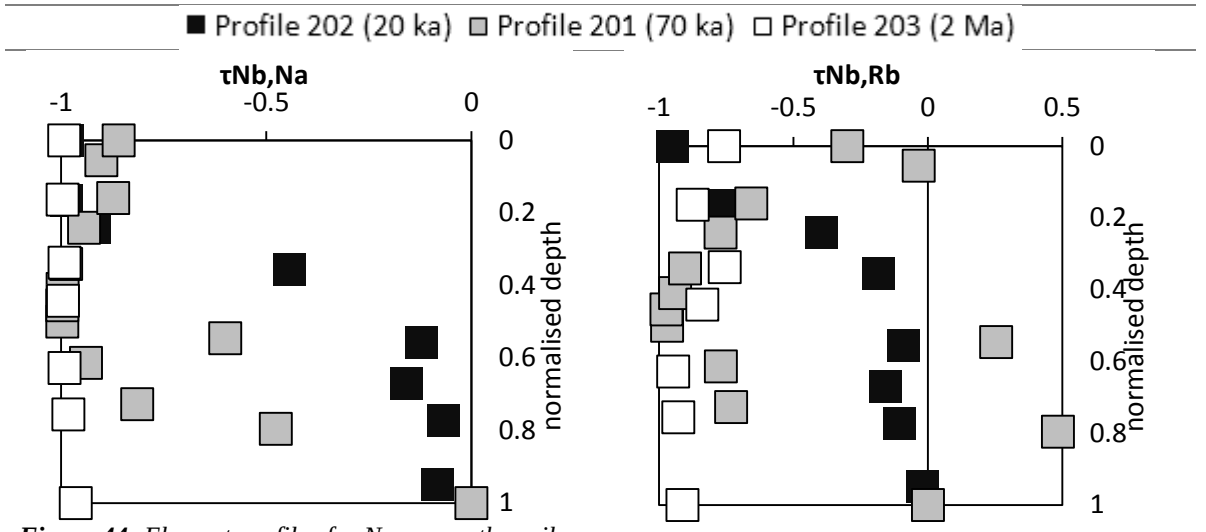

Figure 44: *Element profiles for Na across the soil chronosequence*

Figure 45*: Element profiles for Rb across the soil chronosequence.*

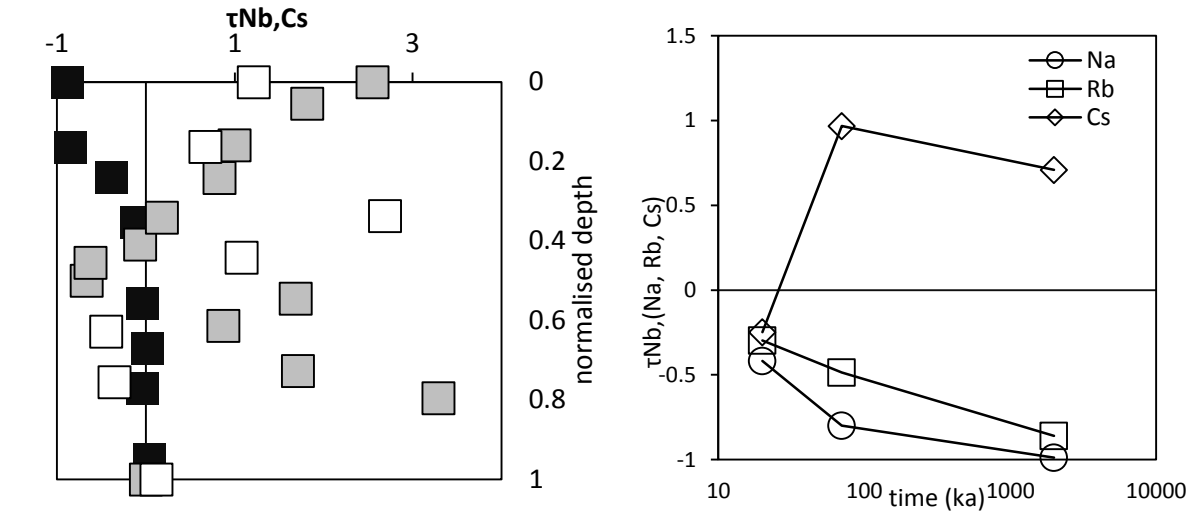

Figure 46*: Element profiles for Cs across the soil chronosequence.*

Figure 47*: Average mass transfer coefficients for Na, Rb and Cs calculated from all samples in each soil profile, as a function of soil age.*

5.6.3 Alkaline earth metals (Mg, Sr, Ba)

In the 20 ka profile, Mg (Figure 48) is depleted in the upper 30% of the profile and enriched in the bottom 70%, suggesting it has been redistributed from higher to lower soil horizons. In the 70 ka profile, this enrichment is completely lost in the top 30% of the profile, and approaches bedrock concentrations on approach to the bottom of the soil profile. In the 2 Ma profile, all of the Mg is lost throughout the entire profile. For Sr (Figure 49), in the 20 ka profile, there is slight loss in the bottom half of the profile which approaches 100% loss at the surface. In the 70 ka profile, Sr becomes systematically depleted half way up the profile, and shows a relative gain of 30% on approach to the surface. However, this gain is completely lost in the 2 Ma profile where total Sr losses approach 95%. Meanwhile, Ba (Figure 50) becomes progressively depleted in the 20 ka profile with decreasing depth and reaches 98% depletion at the surface. In the 70 ka profile, the point of 100% Ba loss is lowered halfway down the soil profile and from this point Ba is added on approach to the surface by 25%. By 2 Ma this additional Ba has been almost completely removed at the surface, but about 50% remains at depth, suggesting Ba has been transported from upper to lower soil horizons.

Over time, the average concentrations of each element in each of the soil profiles (Figure 51) show that by 20 ka, 40% of the original Sr and Ba is lost. Mg has been neither gained nor lost on account of its redistribution from upper to lower horizons. By 70 ka, Sr and Ba are further depleted to 87%, while 66% of the Mg has been lost and represents the fastest loss rate among the three element. In the 2 Ma profile, both Mg and Sr are further leached from the profile and approach 99% depletion, while Ba is relatively enriched by 63%.

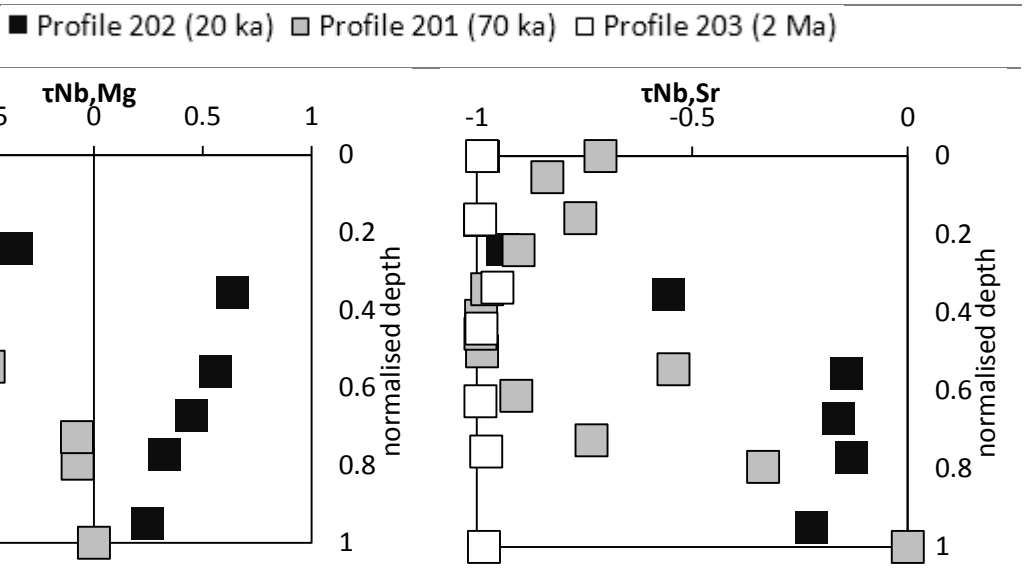

***Figure 48**: Element profiles for Mg across the soil chronosequence.*

***Figure 49**: Element profiles for Sr across the soil chronosequence.*

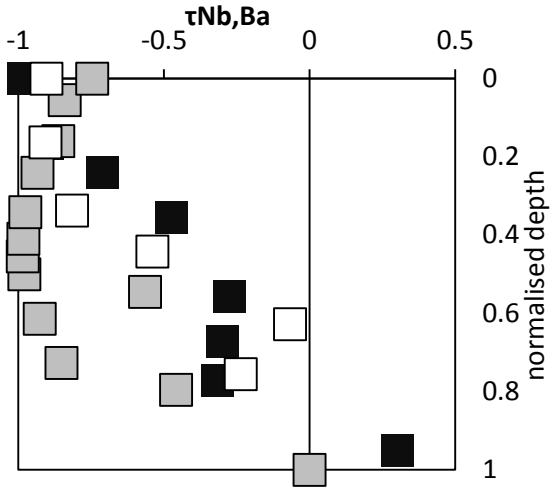

***Figure 50**: Element profiles for Ba across the soil chronosequence.*

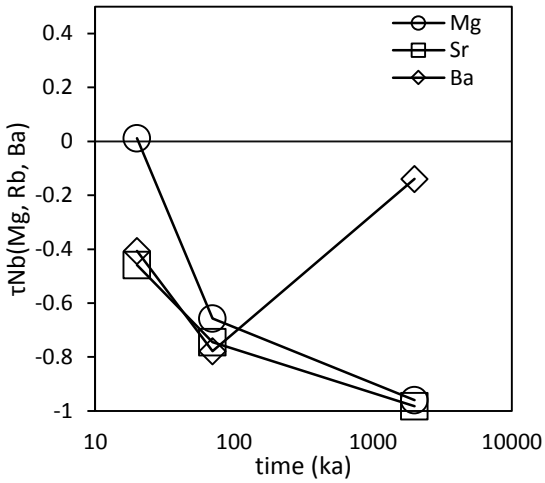

***Figure 51**: Average mass transfer coefficients for Mg, Sr and Ba calculated from all samples in each soil profile, as a function of soil age.*

5.6.4 Transition metals (Ti, Zr, Ta)

In the 20 ka profile (Figure 52), Ti is depleted by as much as 44% in the upper 15% of the soil profile, and enriched by around 20% in the bottom 85% of the soil profile which suggests Ti has been transferred from upper to lower soil horizons. In the 70 ka profile, Ti remains immobile in the bottom half of the profile, but is lost by as much as 62% in the top 15% of the soil profile. In the 2 Ma profile, Ti is lost throughout the entire profile, with 66% loss at the surface. Zr (Figure 53) is essentially immobile throughout the bottom 80% of both the 20 and 70 ka profiles, but is depleted at the surface by about 50%. In the 2 Ma profile, Zr is slightly depleted throughout the entire soil profile, with a 66% loss occurring at the surface. Similarly, Ta (Figure 54) is immobile throughout the lower 80% of the 20 and 70 ka profiles, with only 16% loss at the surface. The 2 Ma profile shows Ta is immobile in the bottom 85% of the profile and approaches 17% loss at the surface.

Over time, the average concentrations of each element in each of the soil profiles (Figure 55) show that by 20 ka, less than 5% of Zr, Ti or Nb has been lost. By 70 ka, Ti and Zr experience losses of 15 and 10%, while Nb experiences a gain of 8%. The loss of Ti during this period is the fastest decline among the three elements at any time. In the 2 Ma profile, over 34% of the original Ti and 16% of the Zr has been lost, while Ta has only lost 3%.

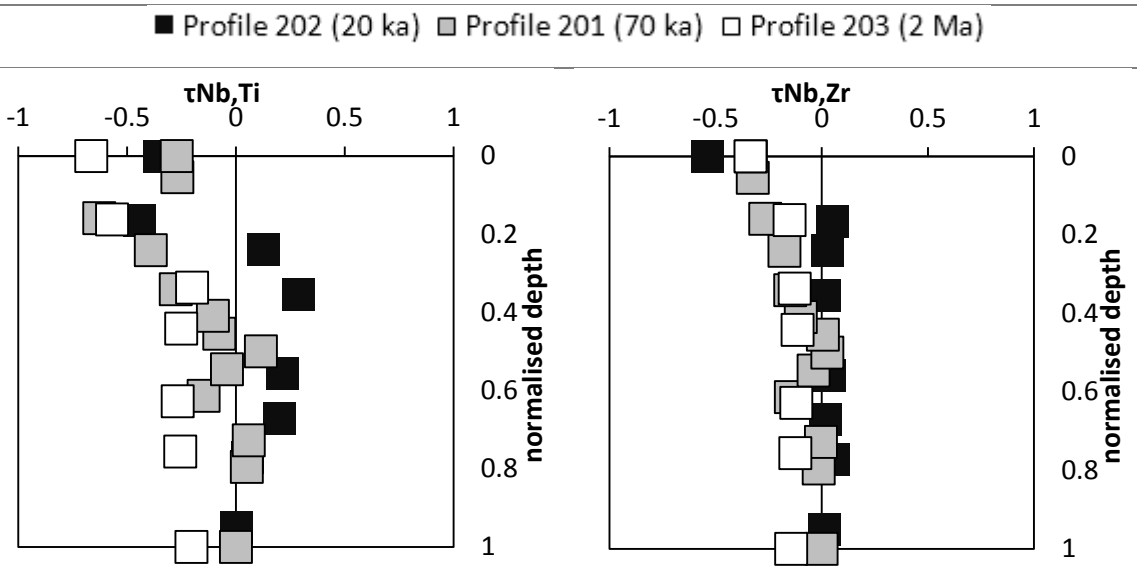

***Figure 52**: Element profiles for Ti across the soil chronosequence.*

***Figure 53**: Element profiles for Zr across the soil chronosequence.*

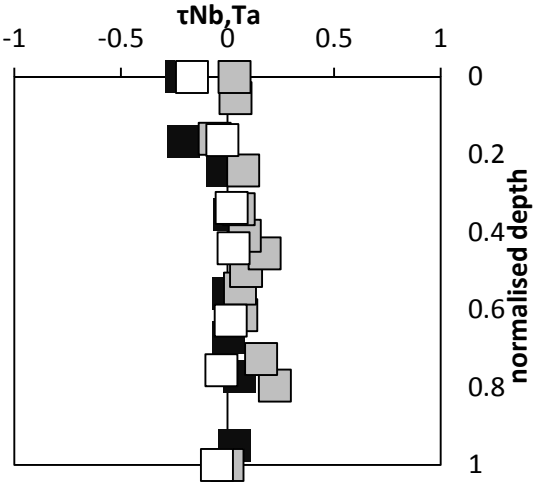

***Figure 54**: Element profiles for Ta across the soil chronosequence.*

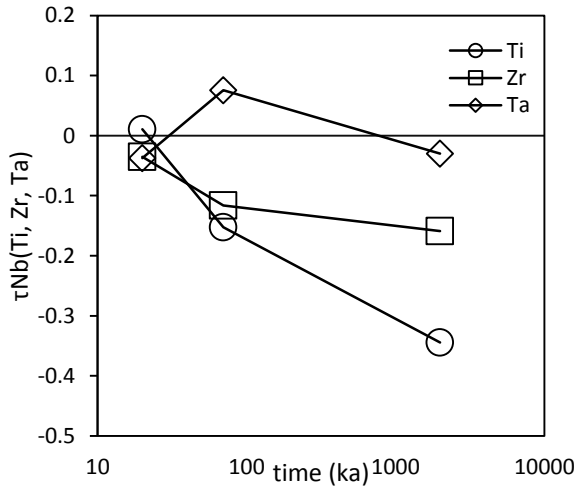

***Figure 55**: Average mass transfer coefficients for Ti, Zr and Ta calculated from all samples in each soil profile, as a function of soil age.*

5.6.5 Transition metals (Cu & Mn)

Mn (Figure 56) is depleted in the upper 20% of the 20 ka profile and enriched in the bottom 80%, suggesting re-distribution of Mn has occurred from upper to lower soil horizons. In the 70 ka profile, Mn is lost in the upper 35% of the profile, while the bottom 65% approaches bedrock concentrations. In the 2 Ma profile, Mn is systematically lost with decreasing depth and approaches 90% depletion at the surface. Similarly, Cu (Figure 57) experiences losses of 50% at the surface of the 20 and 70 ka profiles, and this is redistributed to the bottom 75% of the profile. In the 2 Ma profile, the gain of Cu in the lower 75% that occurred in the 20 and 70 ka profiles is not realized and suggests that the previously accumulated Cu has been leached.

Over time, the average concentrations of each element in each of the soil profiles (Figure 58) declines over time. That Cu experiences the most rapid decline throughout the chronosequence, yet is only depleted by 10% in the 2 Ma profile suggests that element redistribution cannot account for all the Cu gained. Mn is also lost systematically with time, (the most rapid loss occurring during the first 70 ka of soil development) and is depleted by 75% in the 2 Ma profile.

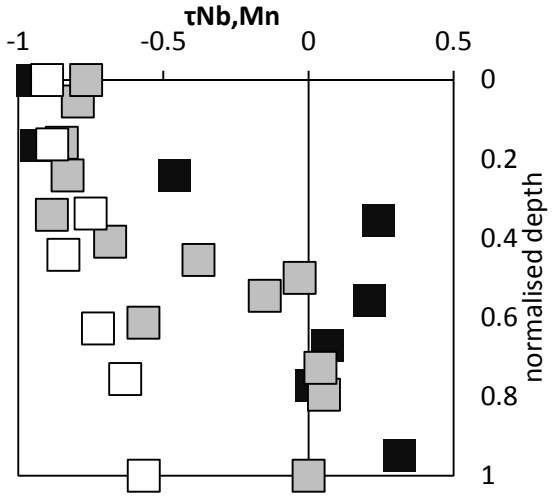

***Figure 56**: Element profiles for Mn across the soil chronosequence.*

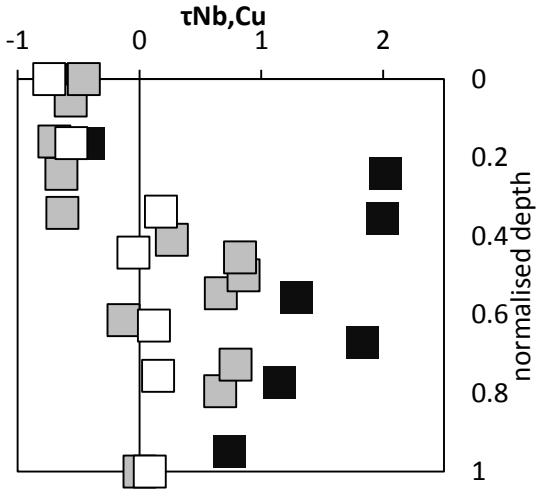

***Figure 57**: Element profiles for Cu across the soil chronosequence.*

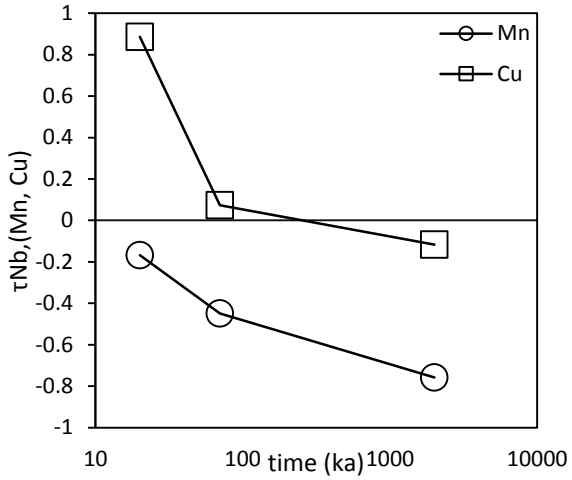

***Figure 58**: Average mass transfer coefficients for Mn and Cu calculated from all samples in each soil profile, as a function of soil age.*

5.6.6 Lanthanides (La & Ce)

With decreasing depth, La (Figure 59) is progressively depleted in the 20 ka profile, and approaches 100% loss at the surface. In the 70 ka profile, maximum La loss occurs half way down the profile, where it then becomes progressively added by 20% on approach to the surface. The 2 Ma profile does not show this addition, indicating this gain of La is lost over time, with maximum depletion occurring at the surface. Cerium (Figure 60) remains essentially immobile in the bottom 75% of the 20 ka profile and is depleted by 95% at the surface. In the 70 ka and 2 Ma profiles, Ce remains essentially immobile but with outliers of 150% and 70% respectively occurring in the middle of the profile.

Over time, the average concentrations of La rapidly decreases in the 20 and 70 ka profiles with essentially no loss or gain occurring in the 2 Ma profile (Figure 61). In the 20 and 70 ka profiles, Ce is rapidly gained, but similarly to La, remains essentially immobile in the 2 Ma profile.

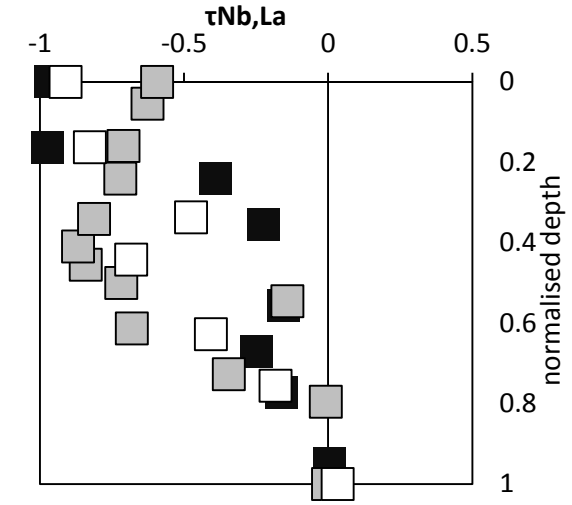

***Figure 59**: Element profiles for La across the soil chronosequence.*

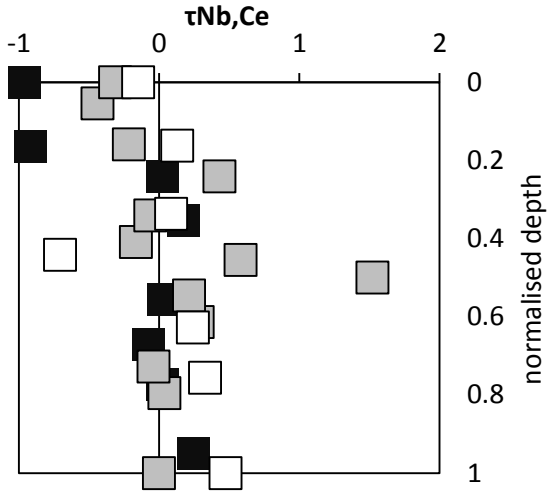

***Figure 60**: Element profiles for Ce across the soil chronosequence.*

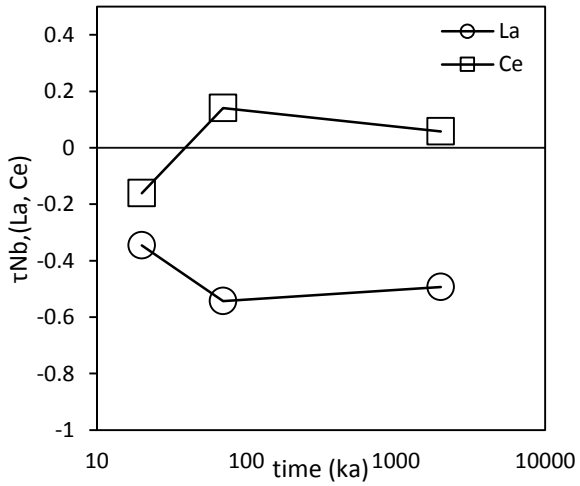

***Figure 61**: Average mass transfer coefficients for La and Ce calculated from all samples in each soil profile, as a function of soil age.*

5.6.7 Lanthanides (Nd, Sm, Eu & Yb)

In the 20 ka profile, loss of Nd, Sm, Eu and Yb (Figures 62-65) only occurs in the top 30% of the profile, with complete loss in the top 20%. In the 70 ka profile, loss of these elements starts deeper, with the top 60% experiences loses in excess of 50%. In the 2 Ma profile, loss of elements starts at the bottom and progressively reaches 90% depletion at the surface.

Over time, these REE show similar behaviour to each other and are progressively lost in soil, with average soil profile concentrations approaching 25% loss during the first 20 ka (Figure 66). After 70 ka, losses approach 35%, and after 2 Ma, losses are in excess of 50%.

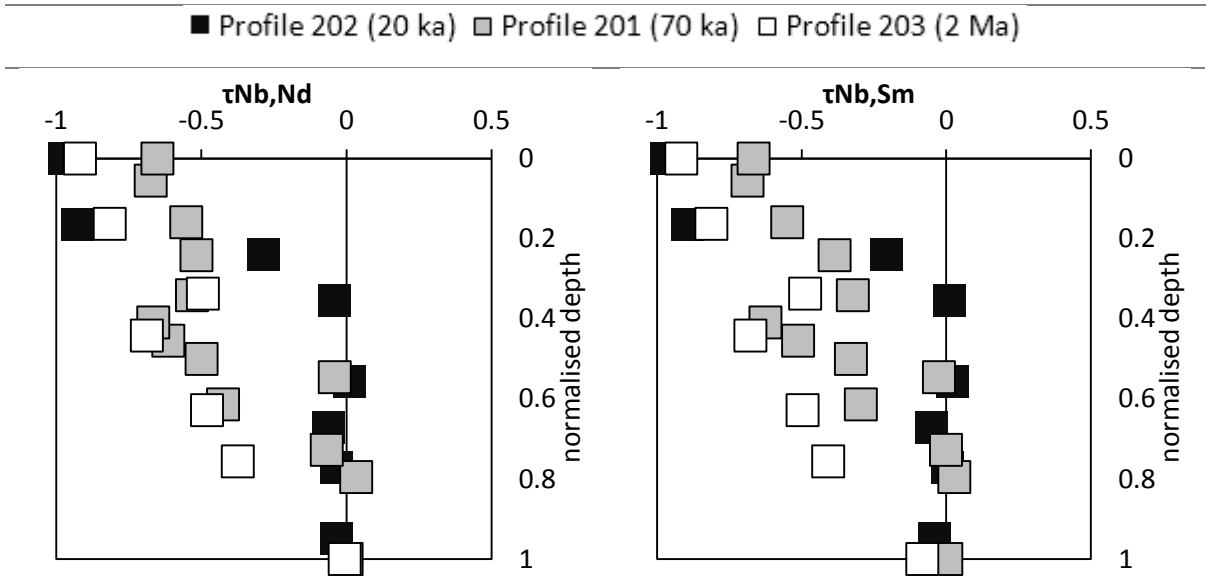

***Figure 62**: Element profiles for Nd across the soil chronosequence.*

***Figure 63**: Element profiles for Sm across the soil chronosequence.*

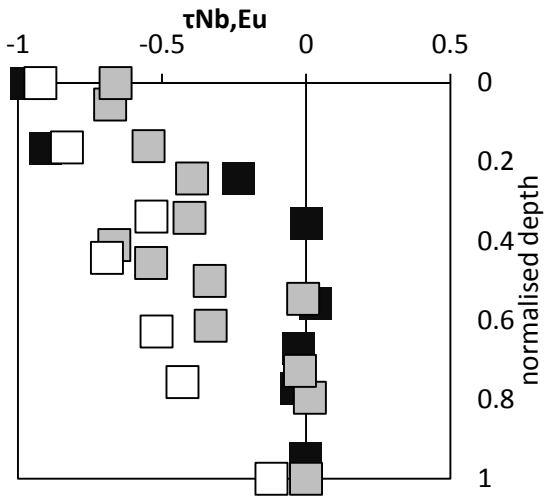

***Figure 64**: Element profiles for Eu across the soil chronosequence.*

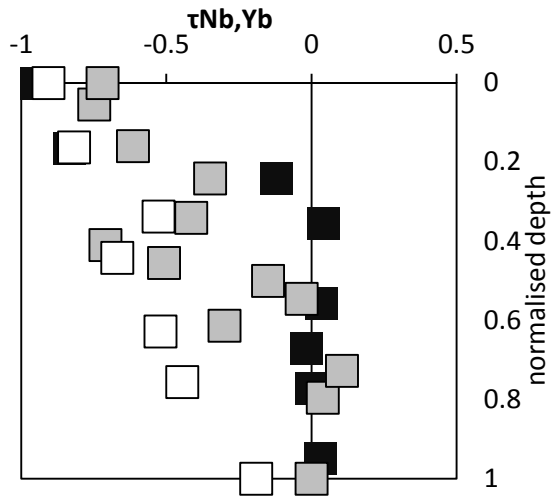

***Figure 65**: Element profiles for Yb across the soil chronosequence.*

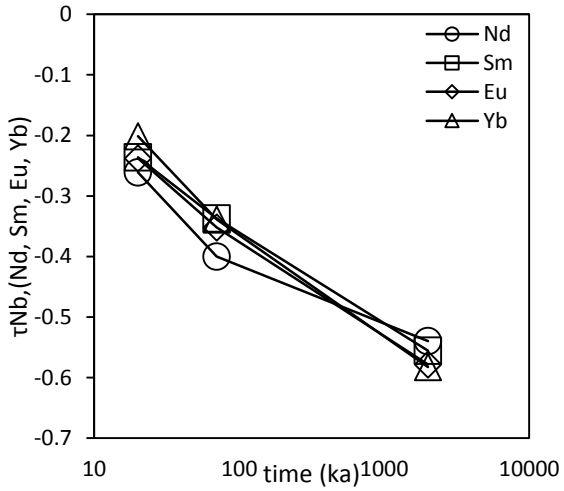

***Figure 66**: Average mass transfer coefficients for Nd, Sm, Eu and Yb calculated from all samples in each soil profile, as a function of soil age.*

5.6.8 Actinides (U & Th)

In the 20 ka profile, both Th and U remain immobile in the bottom 70% of the profile and becomes progressively depleted towards the surface, where about 50% of U and Th is lost (Figures 67 and 68). In the 70 ka profile there is slight enrichment of Th and U in the bottom 85% of the profile by about 15% and 30% respectively, with minor loss occurring at the surface for Th (10%). In the 2 Ma profile, Th remains largely immobile with only minor loss (10%) at the surface. Similarly, U is immobile except for two outliers 40% of the way down the profile, and may reflect redistribution from upper horizons.

Over time, Th is essentially immobile throughout the chronosequence, with gains and losses of less than 20% occurring during the 2 Ma of soil development (Figure 69). Uranium on the other hand becomes progressively enriched throughout the chronosequence, with the most rapid addition of U occurring between 20 and 70ka. By 2 Ma, U is enriched by as much as 40% compared to the parent material.

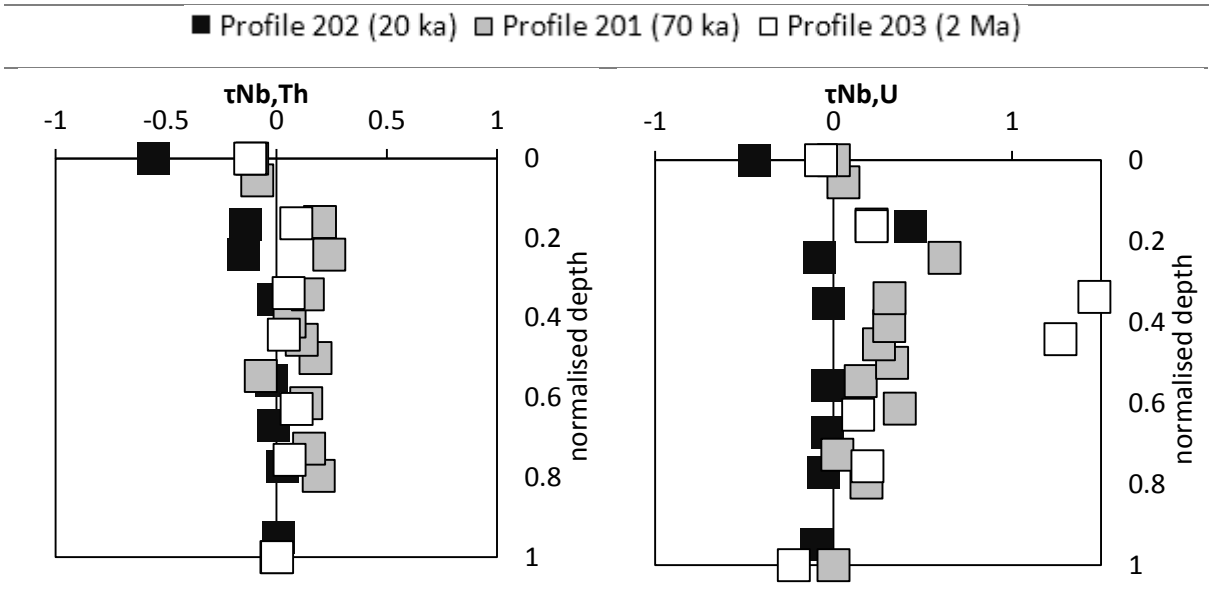

***Figure 67**: Element profiles for Th across the soil chronosequence.*

***Figure 68**: Element profiles for U across the soil chronosequence.*

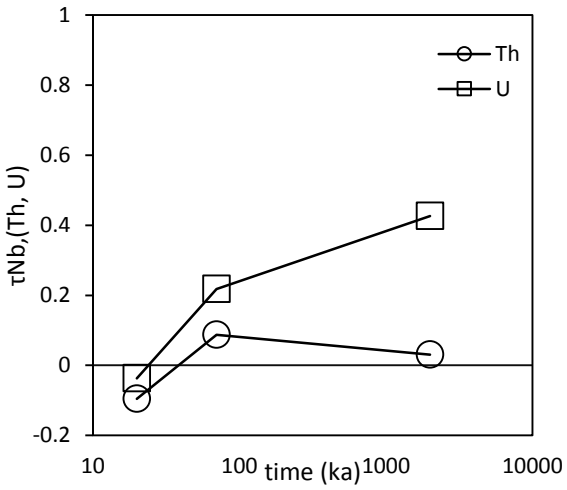

***Figure 69**: Average mass transfer coefficients for U and Th calculated from all samples within each soil profile, as a function of soil age.*

Chapter 6: Discussion

6.1 Mineral dissolution

In this section, the rate of primary mineral dissolution at Reunion Island is quantified and the source of the minerals that participate in these reactions is discussed. Additionally, the factors that affect mineral dissolution and how they vary with time are examined. Finally, the main secondary phases are identified and the factors that control their formation through time is discussed.

Mineral dissolution at Reunion is rapid, with 30% of primary minerals weathered by 20 ka, 60% by 70 ka and 90% by 2 Ma (Figure 70). The nature of the dissolution is logarithmic, i.e. it is most intense during the first 70 ka of soil development but then declines at a reduced rate for the next 2 Ma. Within the profiles themselves, the upper halves are most susceptible to primary mineral loss and are the first to be chemically weathered (Figure 29). Even by 20 ka, 75% of the primary minerals are lost at the surface, and by 70 ka, this loss extends throughout the entire top half of the soil profile (Figure 29).

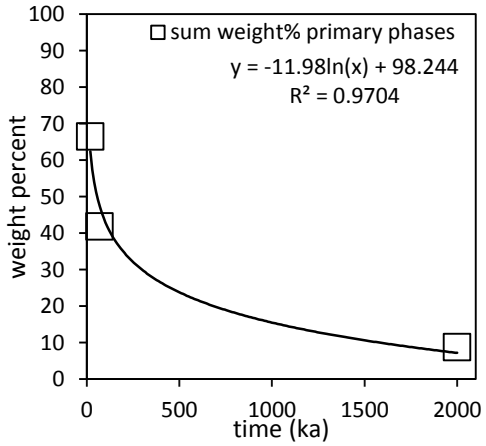

***Figure 70**: The mean concentration of primary minerals (determined by XRD) in each profile as a function of soil profile age. Here, the primary minerals are olivine, pyroxene, plagioclase and K-feldspar.*

Elements that are easily removed from minerals during chemical weathering are useful in constraining the relationship between mineral dissolution and element loss because they are likely to be lost due to dissolution only. The alkali and alkaline earth elements are good candidates because they are abundant in primary minerals such as olivine, plagioclase and pyroxene, and so losses of these minerals in the soil should correspond to losses of the alkali and alkaline earths. If this is true, then the concentrations of primary minerals should correlate positively with the normalised concentrations for that element. In other words, if the main cause of alkali and alkaline earth loss in soil is from the dissolution of primary minerals, then there should be a mathematic relationship between them. This can be tested by calculating the relationship between the change in element concentration and the change in concentration of the primary mineral that hosts that element. For example if primary mineral dissolution is suspected to be the main factor responsible for the loss of Na in the soil, changes in plagioclase concentration should be correlated with changes in Na concentration, since plagioclase is the dominant source of Na in the soil. If this assumption is correct, then there should be a mathematical relationship between the two variables, with stronger relationships identified by higher correlation coefficients.

This method was used to quantify how much primary mineral dissolution contributed to the loss of alkali and alkaline earth elements. This relationship was only quantified for the two younger profiles, 202 (20 ka) and 201 (70 ka) since the oldest profile 203 (2 Ma) was almost totally depleted in the alkali and alkaline earth elements. The results indicate a strong linear relationship between the abundance of olivine and pyroxene, plagioclase and K-feldspar to the mass transfer coefficients of all six alkali and alkaline earth elements (Figures 71-76). The relationship between these minerals and elements in profile 201 is not as strong, but this is mainly due to an outlier (sample 201J) that has an unusually high amount of plagioclase in the B1 horizon.

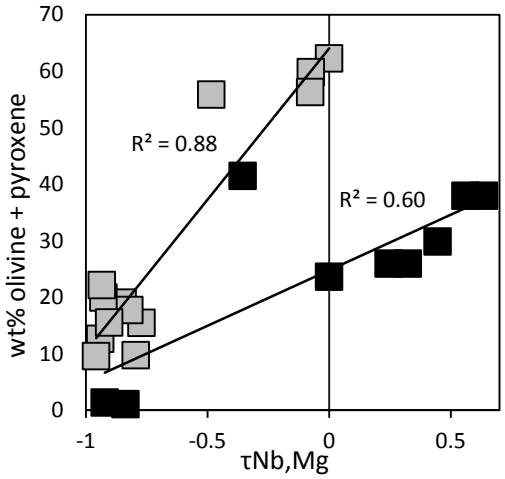

***Figure 71**: Least-squares analysis for Mg loss and changes in olivine and pyroxene concentration.*

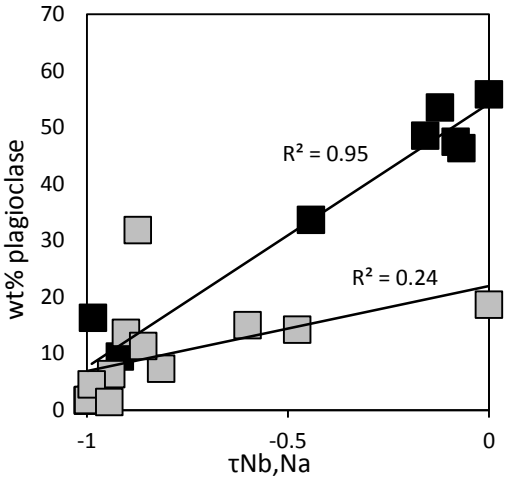

***Figure 72**: Least-squares analysis for Na loss and changes in plagioclase concentration.*

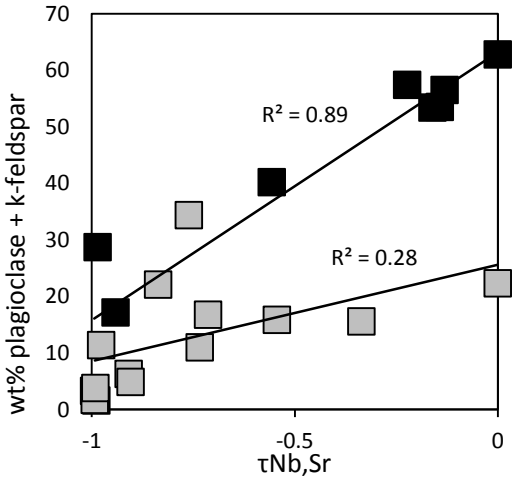

***Figure 73**: Least-squares analysis for Sr loss and changes in plagioclase and K-feldspar concentration.*

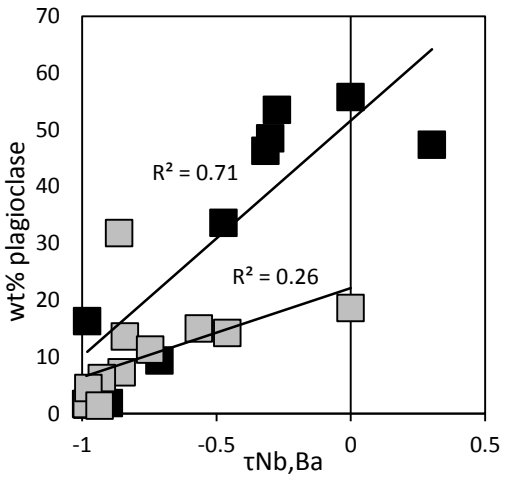

***Figure 74**: Least-squares analysis for Ba loss and changes in plagioclase concentration.*

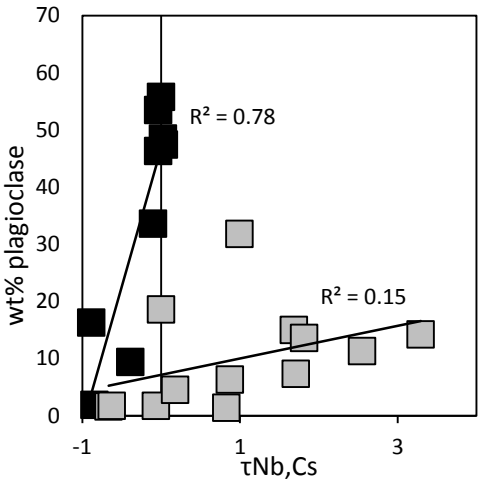

***Figure 75**: Least-squares analysis for Cs loss and changes in plagioclase concentration.*

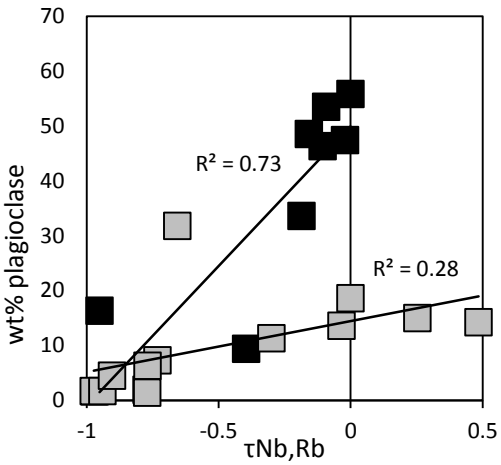

***Figure 76**: Least-squares analysis for Rb loss and changes in plagioclase concentration.*

If the outlier in the 70 ka profile is ignored (sample 201J), the majority of alkali and alkaline earth loss is more than likely caused by the dissolution of primary phases. Of these phases, a single mineral, plagioclase can account for most of the loss of Na, Rb, Cs, Sr and Ba in the soil. This is unsurprising given most of these elements can substitute for Ca or Na in its crystal lattice. Of the elements analysed, only Mg is incompatible in the feldspar framework, due to its ionic potential being too high (Heier 1960). Rather, pyroxene and olivine are the minerals that host the bulk of Mg and is why concentrations of these minerals are instead. Similarly, non-silicate minerals such goethite, manganese dioxide and monazite as can also control the soluble element budget in soil, especially the REE and actinides (Aide *et al.* 2012; Pett-Ridge *et al.* 2007). Although the REE are intrinsically depleted in mafic melts, they can still be useful in constraining rates of primary mineral dissolution.

The REE are generally more resistant to loss in soil compared to the alkali and alkaline earths because of their strong association with organic matter, secondary phosphate minerals and oxyhydroxides (Aide *et al.* 2012). However, their relatively low electronegativity means the REE generally form ionic rather covalent bonds, and can be leached from soil over geological time. Since the REE all display the same 3+ oxidation state (except for Eu which exists as a 2+ cation and Ce which can oxidised to 4+) they tend to act similarly to each other (Laveuf and Cornu 2009). In soil solution, the REE can be derived from either primary or secondary phases. The primary minerals are typically refractory oxide phases or soluble phosphates.

Oxides such as ilmenite, rutile and zircon host the REE as impurities in the crystal lattice formed during crystallisation, while phosphates such as monazite and apatite host the REE as intrinsic members of the crystal (Aide *et al.* 2012). Upon dissolution of these minerals, the REE can be adsorbed onto the surfaces of clays or into the interlayer sites and have the ability to displace alkali and alkaline earth elements during cation exchange (Coppin *et al.* 2002). Since the REE can be scavenged by Fe and Mn oxides (via adsorption or cation exchange), their concentration in soil is affected by redox conditions and so are not as reliable as the alkali and alkaline earths as proxies for chemical weathering.

At Reunion Island, the REE are systematically lost with decreasing depth and increasing soil age (Figures 62-66). For Nd, Sm, Eu and Yb, the element profiles are depleted and behave almost identically to each other within the same profile. However, Ce and La do not share these systematic trends and in the case of Ce, actually shows gain rather than loss over time. For most of the REE, approximately 40% of the original amount is retained in the bottom half of the 2 Ma profile which indicates that although they are mobile, they are more resistant to leaching than the alkali and alkaline earths (Figures 62-66). Additionally, considering that the abundance of illite and goethite increases with increasing age across the chronosequence, it is possible that the formation of these secondary phases is retarding REE loss via adsorption. Interestingly, like the alkali and alkaline earths, there is reduced loss of REE in the top 15% of the 70 ka profile compared to the 20 ka profile, which could suggest gain of elements from atmospheric sources (e.g. aeolian dust). After 2 Ma however, there is no sign of this gain, presumably by the dissolution of these atmospheric additions.

Since the element profiles for Nd, Sm, Eu and Yb differ markedly with those of La and Ce, there must be processes retarding the loss of La and Ce in the soil. Unlike the other REE, Ce is sensitive to changes in soil redox because its ability to oxidise to Ce^{4+} can result in the formation of the refractory oxide CeO_2, the implications of which will be discussed in a later section. Lanthanum on the other hand has the lowest ionic potential of all the REE and therefore can be preferentially adsorbed onto clays at the expense of the other REE (Laveuf and Cornu 2009). In any case, by 70 ka there has been addition of both REE and alkali and alkaline earth elements, and the probable mechanism responsible is dust deposition.

The transition metals Ti, Zr and Ta can also participate in mineral dissolution reactions but due to their refractive nature, leach from the soil much slower than the alkali, alkaline earths and REE. Using XRD, ilmenite ($FeTiO_3$) was detected throughout the soils of Reunion Island and is therefore the main source of Ti. Even though zircon ($ZrSiO_4$) and rutile (TiO_2) were not detected by XRD, they probably exist in the soil in trace amounts and would be the main hosts of Zr and Ta respectively (Middelburg *et al.* 1988). Ilmenite is the most weatherable of the refractory minerals because the Fe in ilmenite can be oxidized and subsequently lost, forming the rutile pseudomorph anatase. If soil conditions are acidic, the anatase can undergo dissolution and in the process leach Ti. Loss of Ti is also accelerated by organic compounds in the soil solution that can complex with Ti and increase its solubility (Cornu *et al.* 1999).

At Reunion Island, Zr and Ta remain immobile in the bottom 80% of the 20, 70ka and 2 Ma profiles, and only slightly depleted at the surface, while Ti is lost at deeper depths in all profiles and this loss increases over time (Figure 52-55). By 2 Ma nearly 70% of the original Ti is lost at the surface, more than three times as much as Ta (Figure 77).

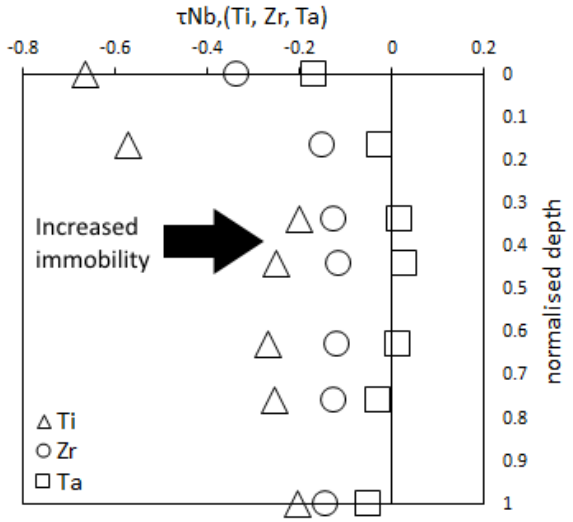

***Figure 77**: Mass-transfer coefficients of Ti, Zr and Ta from Profile 203 (2 Ma).*

These results indicate that the top 20% of the soils become progressively acidic over time and is probably a consequence of humic acids formed at the surface by organic matter breakdown and carbonic acid formed via plant root respiration (Cornu *et al.* 1999). These acidic

conditions cause Ti to be lost more rapidly and completely than Zr, Ta or Nb, and these results agree with the conclusion of Kurtz *et al.* (2000) that Ta and Nb are the most reliable index elements for use in mass transfer calculations.

6.2 Secondary mineral precipitation

The main secondary minerals at Reunion Island are gibbsite ($Al(OH)_3$), halloysite and kaolinite ($Al_2Si_2O_5(OH)_4$), goethite (FeOOH), and illite ($(K,H_3O)(Al,Mg,Fe)_2(Si,Al)_4O_{10}[(OH)_2,(H_2O)]$) and only become a significant proportion of the soil mass after 70 ka. The formation rate of these secondary phases over time is logarithmic (Figure 78).

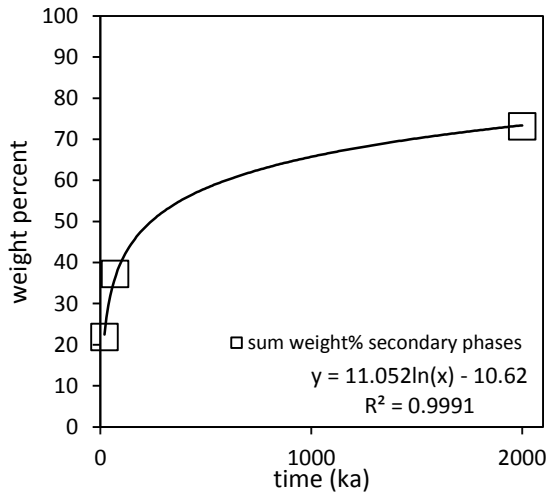

Figure 78*: The mean concentration of secondary minerals in each profile was calculated and plotted as a function of time. Here, the results indicate the gain is logarithmic.*

Gibbsite and halloysite dominate the 2 Ma soil because they are the end-products of a soil subjected to a high-rainfall weathering regime, and will form in silica-poor soils over time. This is because hydrolysis reactions release silica which can be leached, increasing the proportion of Al in the soil to such an extent that clays and hydroxides preferentially incorporate it into their crystal structure (Kleber *et al.* 2007). By 2 Ma, halloysite and gibbsite account for more than 60% of the total soil mass in profile 203 (Figures 36-37). Other non-

silicate secondary phases such as goethite and illite reflect a similar trend, with the 2 Ma profile the most enriched in these phases.

Interestingly, halloysite is the dominant secondary mineral in the 2 Ma soil, but there are also considerable amounts of gibbsite, particularly in the C1 and C2 horizons (Figure 79). Although this mixture of secondary phases in soil has been observed before (e.g. Jongmans *et al.* 1994), it is unusual to observe the preferential formation of halloysite over gibbsite at Reunion Island. Most of the silica should have been leached away from the topsoil after 2 Ma, especially considering the intense chemical weathering conditions at Reunion Island, and implies that there is some process that is conserving Si.

If the formation of one phase controls the formation of the other, there should be a mathematical relationship between the two mineral abundances. This was tested for the 2 Ma profile only, where halloysite is formed in appreciable amounts (Figure 80).

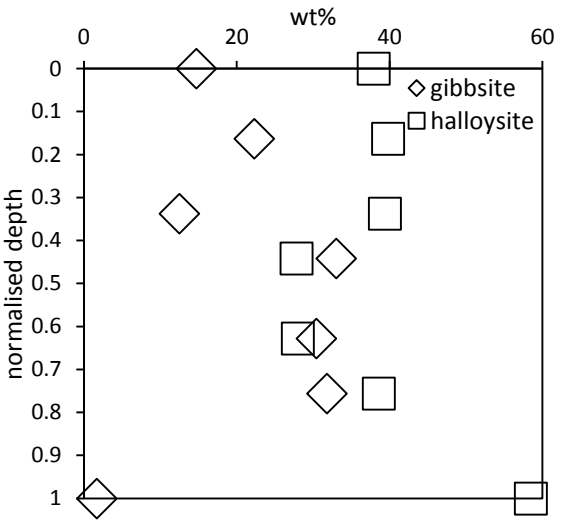

***Figure 79**: The concentrations of gibbsite and halloysite in the 2 Ma profile determined by XRD as a function of normalized soil depth.*

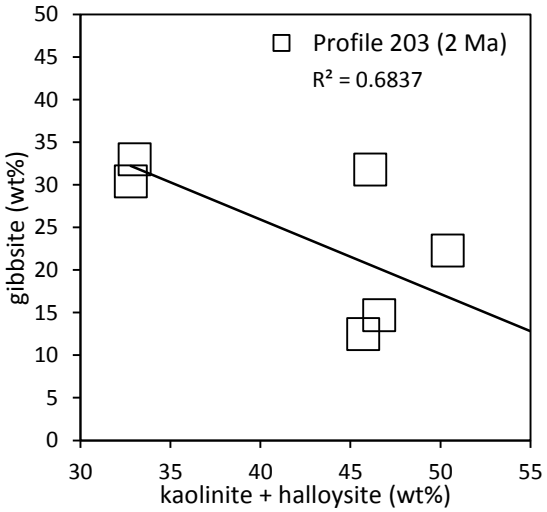

***Figure 80**: Least-squares analysis for the concentration of kaolinite and halloysite and the concentration of gibbsite in all samples of the 2 Ma profile.*

Throughout the 2 Ma profile, the vertical distribution of halloysite is fairly uniform, even extending well into the upper A horizon. When the regression analysis is performed, the inverse relationship between the concentration of halloysite and gibbsite may suggest a genetic relationship. This is similar with findings from soils in Costa Rica (Kleber *et al.* 2007). Kleber postulated that biological activity is responsible for the conservation of Si by pumping dissolved silica throughout the upper soil profile by plants. This results in concentrations of Si high enough to form alumina-silicates such as kaolin and halloysite. Although Si concentrations were not quantified in this project, if the kaolin group can be used as a proxy, then such a process could be occurring at Reunion.

6.3 Atmospheric addition

Once released by the dissolution of primary minerals, the mobility and fate of the alkali and alkaline earths are mainly determined by the ionic potential of the element, i.e. the ratio between ionic charge and ionic radius (Buggle *et al.* 2011; Ryan 2014). For elements that have relative large radii per unit charge (i.e. a low density surface charge), they can exist in solution as soluble cations. The alkali and alkaline earths show this behaviour (Figure 81). Consequently, unless adsorbed onto the surfaces of clays or charged colloids, these elements will be flushed out with water.

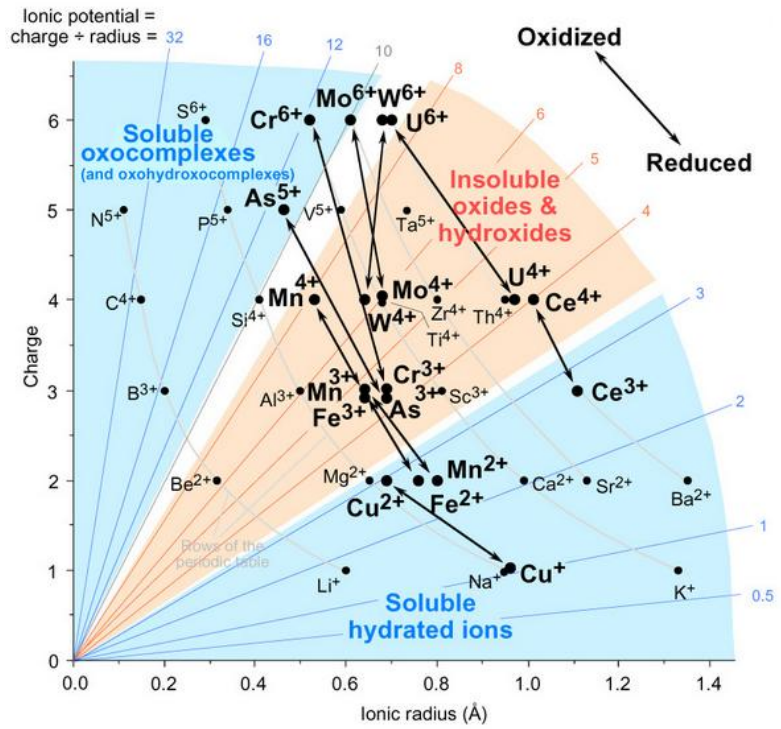

***Figure 81**: Ionic potential of common ions. From Railsback (2006).*

The high solubility of Na, Mg, Rb and Sr is clear in the soils of Reunion Island, whereby after 2 Ma, more than 99% of these cations are removed from the soil. The high rainfall regime of Reunion permits such a scenario. Interestingly, relatively high concentrations of Ba and Cs remain in the soil even after 2 Ma, despite sharing similar geochemical behaviour to their leached group members. In the case of Cs, the average soil profile composition is actually enriched by 70% compared to the unaltered bedrock in the 2 Ma soil. Similarly, although Na, Sr and Rb remain depleted in the upper half of the 70 ka profile, there is a relative gain on approach to the surface. That addition of Na, Sr, Rb, and Ba in the upper soil horizons in the 70 ka profile has occurred, but not in the 20 ka or 2 Ma profiles suggests the process responsible is operating at a rate that is only observable over at least 70 ka. By 2 Ma this addition has been lost, presumably from leaching. The extent of addition for a given element can be made in comparison to its most depleted concentration in the soil (relative enrichment), or to its concentration in the parent material (absolute enrichment). In order of least to most enriched (on both a relative and absolute basis), Mg < Na < Ba < Sr < Rb < Cs (Table 12 and Figure 85).

***Table 12**: Extent of addition for the alkali and alkaline earths in the 70 ka profile.*

Element	Relative enrichment (%)	Absolute enrichment (%)	Average crust (ppm)
Mg	6	-90	28 000
Na	14	-86	23 000
Ba	23	-75	620
Sr	28	-71	320
Rb	94	-30	49
Cs	320	+250	4.9

Relative enrichment is defined as the difference between the highest and lowest mass transfer coefficient in the top 50% of the 70 ka profile. Absolute enrichment is the difference between bedrock composition (mass transfer coefficient = 0) and the most positive mass transfer coefficient. Average crustal concentrations are a proxy for dust composition. Average crust data compiled from Rudnick and Gao (2003).

Enrichment of Cs is much greater than the other alkalis, both in an absolute and relative sense, and instead of total depletion after 2 Ma, the added Cs remains in the soil. There are two possible explanations for this input of alkali and alkaline earths – addition via sea spray, or dust. Addition via sea spray could account for the surficial addition of alkali and alkaline earth elements since seawater is relatively enriched in these elements and the majority of them have high affinity for clays, Fe oxides and organic matter and could be adsorbed on contact with the soil. Although atmospheric inputs of the alkali and alkaline earths have not been quantified, it would not be unreasonable to assume that over timescales greater than 20 ka, the relative proportion of cations derived from the atmosphere becomes larger as bedrock weathering rates decline and soluble cations are leached from the soil (e.g. Chadwick *et al.* 1999). Additionally, it appears that if dust deposition is the principal input of alkali and alkaline earth elements after 20 ka, then it is the rate of input rather than the abundance of clays and Fe-oxides that controls the upper element profile. This is because by 20 ka, goethite, kaolinite and halloysite already make up a third of the mineral mass present in the upper horizons (Figures 36-37). If dust were to contribute to the alkali and alkaline budget during such a short timescale, it should have been detected in the 20 ka element profiles (Figures 44-50). However, the corresponding increases in expected atmospheric derived cations has not occurred until 70 ka (Figures 44-50 and 82-84). Therefore, if dust deposition does enrich the upper horizons of the soil in alkali and alkaline earths, then it must take longer than 20 ka.

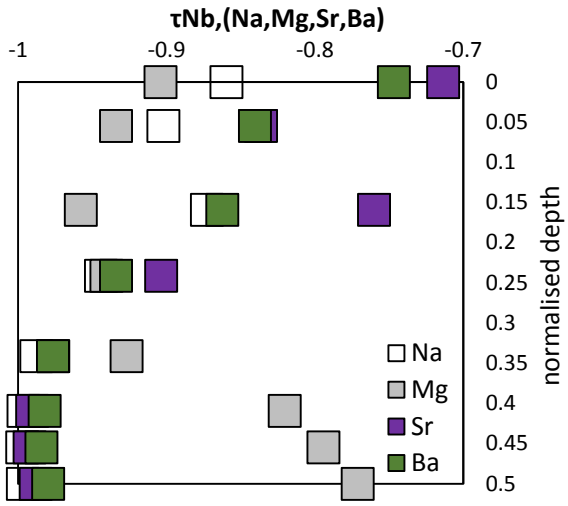

***Figure 82**: Upper half of the 70 ka profile showing the relative enrichment of Na, Mg, Sr and Ba. In order of greatest to least enriched (relative to its minimum tau value), Sr > Ba > Na > Mg.*

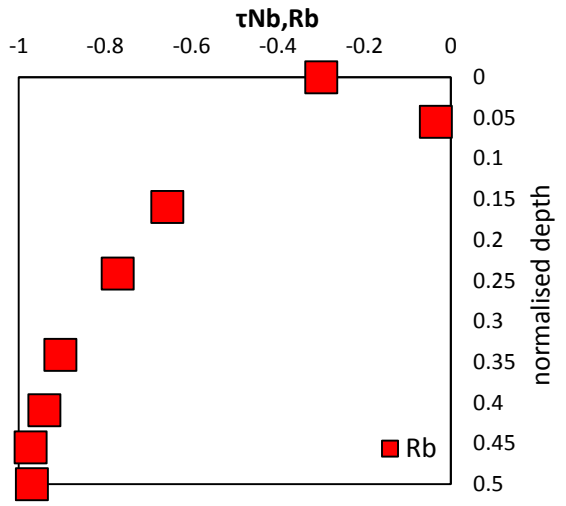

***Figure 83**: Upper half of 70 ka profile showing the relative enrichment of Rb. Rubidium is enriched by 94% relative to its maximum depletion value.*

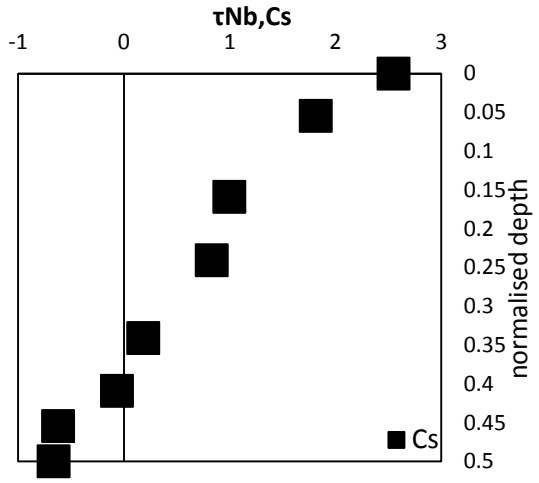

***Figure 84**: Upper half of the 70 ka profile showing the relative enrichment of Cs. Cs is enriched the most on both a relative and absolute basis, with 320 and 250% respectively.*

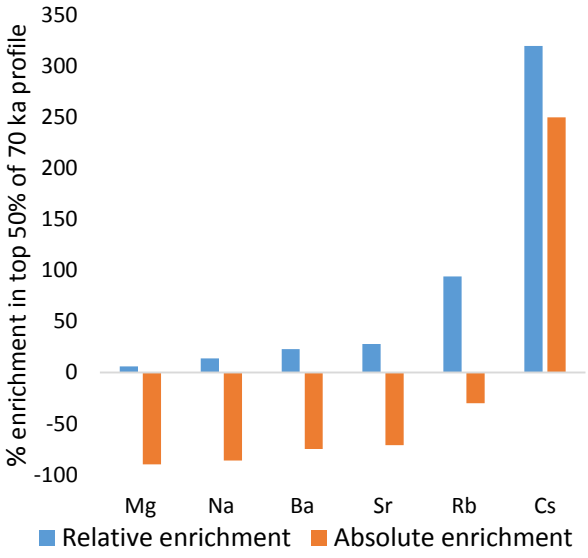

***Figure 85**: Graphical representation of Table 12.*

Relative to their points of greatest depletion, Mg is only enriched by 5% and Cs by 300% on approach to the surface. This is surprising for two reasons. Firstly, of the group 1 and 2 elements analysed, Cs is the least abundant in both the ocean and in soils and yet is the most enriched in the upper regolith. Conversely, Na and Mg, two of the most abundant elements in the lithosphere, are the two elements the least enriched. If sea spray or dust is the process that adds alkali and alkaline earths to the upper 70 ka profile, then there must be a process occurring in the soil that is enriching the heavier alkalis like Cs at the expense of the others. One process that can explain this behaviour is cation exchange on the surfaces of clays.

Since the surfaces of clays are negatively charged (a result of charge imbalance caused by isomorphic substitution (Ryan 2014)), they have the ability to adsorb certain cations. However, depending on the clay (especially 2:1 clays like illite), some cations are preferentially adsorbed over others. This preference is caused by the hydration energy of the ions, i.e. the amount of energy that is released on hydration of a cation. The lower this energy is, the more likely the cation will adsorb onto clays (Sawhney 1971). Since Cs has the lowest hydration energy of all the alkali and alkaline earth elements (Table 13), clays will exchange any other cation with a higher hydration energy for Cs. This occurs because the force of attraction to a clay surface will be higher for Cs than for any other element. In the case of the alkali and alkaline earths, hydration energies decrease with increasing ionic radius and with decreasing charge (Smith 1977).

Therefore, from highest to lowest selectivity/fixation ability, for the alkalis tested, Cs > Rb > Na and for the alkaline earths Ba > Sr > Mg. If these cations are fixed onto clays on the basis of their hydration energies, then their degree of enrichment should follow this trend. This model fits almost perfectly with what is observed in the top half of the regolith in the 70 ka profile, except that Sr seems to have been slightly favoured over Ba during clay fixation (Figure 82). After 2 Ma however, nearly all the Na, Mg, Rb and Sr cations are completely lost from the soil, while Cs remains enriched relative to original bedrock composition (Figures 84-85).

Table 13: *Hydration enthalpies for the alkali, alkaline earths and REE (Smith 1977).*

Group	Element	Hydration Enthalpies (-kJ mol^{-1})
Alkalis	Na	410
	Rb	300
	Cs	270
Alkaline Earths	Mg	1920
	Sr	1460
	Ba	1320
Light REE	La	3280
	Ce	3360
Mid to Heavy REE	Nd	3420
	Sm	3490
	Eu	3520
	Yb	3700

The REE are also fixed to the upper regolith in the 70 ka profile. In the top 15% of the 20 ka and 70 ka profiles, the average mid and heavy REE mass transfer coefficient increases by 25% from 95% depletion to 70% depletion. Atmospheric addition to weathering profiles of the REE-associated minerals such as apatite ($Ca_5(PO_4)_3(F,Cl,OH)$) has been quantified previously. For example, in isolated islands like Hawaii, atmospheric deposition is a non-negligible contributor to the soil REE budget, especially over timescales of Ma (e.g. Chadwick *et al.* 1999). At Reunion Island, Nd, Sm, Eu and Yb are enriched towards the surface in the 70 ka profile relative to the 20 ka profile, but after 2 Ma, this addition has been almost completely lost (Figures 62-65). This implies that the rate of dust deposition is slower than the rate of mineral dissolution because the elements that are added by dust are being leached faster than they are being deposited.

Unlike Nd, Sm, Eu and Eb, the lightest REE, La is progressively added to the top 40% of the 70 ka profile (Figure 86):

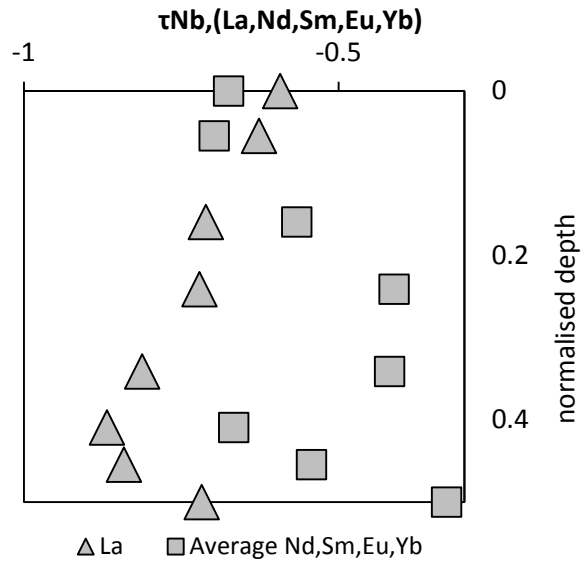

Figure 86*: Mass transfer coefficients for La and averaged Nd, Sm, Eu and Yb coefficients in in the upper 50% of the 70 ka profile.*

The La element profile is similar to those of the alkali and alkaline earths and may suggest that La is added to the soil via atmospheric dust and then subsequently fixed onto the surfaces of clays. Similar to the alkalis and alkaline earths, La is preferentially retained on clay surfaces because of its low hydration enthalpy. The hydration energy model, which successfully explains the progressive enrichment of the alkali and alkaline earths with larger ionic radii in the upper regolith, fails to account for the enrichment of the mid and heavy REE over La. As hydration enthalpies increase across the periodic table from left to right, La should be preferentially adsorbed onto clays over the heavier REE. The fact that this does not happen in the upper 70 ka profile may suggest that clays have diminishing fixation ability for the mid and heavy REE. Instead, other compounds capable of adsorbing REE, such as organic acids and Fe oxyhydroxides may play a greater role in their fixation. For example, Tyler and Olsson (2002) found that up to 74% of the REE extracted from the soil solution of a Swedish Cambisol were associated with dissolved organic carbon. Additionally, it was determined that the stability of both organic and Fe complexes is higher for the mid and heavy REE than for the light REE. At Reunion Island, the fractionation of the REE by organic and inorganic ligands may account for the enrichment of Nd, Sm, Eu and Yb over La in the upper 70 ka profile.

Likewise, U is progressively enriched throughout the chronosequence. This addition of U has probably come from atmospheric sources, particularly wind-blown accessory minerals such as zircon, apatite and monazite, which are the main carriers of U. Previous studies investigating U addition in basaltic soils have determined that the majority of leached dust derived U binds preferentially to amorphous Fe oxyhydroxides (e.g. Pett-Ridge *et al.* 2007). Unlike alkali, alkaline earths and REE, clays do not have a strong affinity for U and therefore does not participate in ion-exchange reactions. Therefore, the main control in retarding U loss in regolith is likely to be the presence of Fe oxides and hydroxides because of their high sorption capacity for U, high surface area and abundance as coatings on mineral grains (Manceau *et al.* 1992). At Reunion, there is little change in U mass transfer coefficients with depth throughout the 20 ka profile, but by 70 ka the average U concentration is enriched by 20% and by 2 Ma 40%, with one sample enriched by 150% compared to the parent material (Figures 67-68).

In conclusion, the addition of elements in the Reunion soils peaks by 70 ka, which suggests that over geological time, the rate of addition is not high enough to overcome the effects of element leaching. Wind-blown dust and sea spray are the likely sources of added alkali, alkaline earths, REE, uranium and thorium to the surface horizons in the 70 ka profile. No attempt has been made to quantify the contribution of elements from each source, but it is conceivable that refractory REE-rich minerals such as apatite are responsible for the addition of heavier elements while sea spray is responsible for the lighter alkalis and alkaline earths. The importance of silicate clays to fix these added elements becomes apparent only after 70 ka, especially for Cs and La, and that this fixation seems to increase as a function of decreasing hydration energy.

6.3.1 The origin of dust at Reunion Island

Oceanic islands regularly come into contact with dust, despite the fact they can be thousands of kilometres away from the nearest continental land mass (e.g. Chadwick *et al.* 1999; Pett-Ridge *et al.* 2007). At Reunion Island, there is systematic and unambiguous addition of trace elements for at least the first 70 ka of soil development. Where does this dust come from, and how much of it is contributing to the trace element budget at Reunion Island? There are several geochemical tools that can be used, but all of them require that we compare the average concentration of an immobile element or isotope in the crust to that of the soil. If a large enough differential exists, two end-members can be established: elements derived from parent material, and elements derived from crustal dust. Thorium/Hf ratios have been used to reliably measure the contribution of dust to soils (e.g. Chadwick *et al.* 1999). However, Hf was not analysed during the project. Since the accuracy of this mass balance relies on the elements being immobile, Nb is used instead. The equation to solve for dust contribution is as follows:

$$f_{dust}^{Th} = \frac{[Nb]_s \cdot (\frac{Th}{Nb})_s - [Nb]_p \cdot (\frac{Th}{Nb})_p}{[Nb]_d \cdot (\frac{Th}{Nb})_d - [Nb]_p \cdot (\frac{Th}{Nb})_p} \qquad \textit{Equation 9}$$

where *[Nb]* is the concentration of Nb in the soil (*s*), parent material (*p*) or dust (*d*) and *Th/Nb* is the ratio in each source.

Since negative contributions are impossible, both the numerator and denominator must be greater than zero for the result to be valid. For Reunion Island, only the 70 ka profile meets this requirement and so will be the only one discussed. Average crustal Th and Nb concentrations were derived from Rudnick and Gao (2003) at 10.5 ppm and 12 ppm respectively and are used as proxies for dust. Following the calculations above, up to 93% of the Th in Profile 201 can be attributed to aeolian dust. The results using Th/Nb were also compared to results derived from Th/Zr as a check and yielded identical values (Table 14).

***Table 14**: Proportion of Th derived from dust in the 70 ka profile.*

Sample	% Th derived from dust using Th/Nb ratio	% Th derived from dust using Th/Zr ratio
201L	39	39
201K	54	54
201J	93	93
201I	76	76
201H	61	61
201G	32	32
201F	26	26
201E	22	22
201D	33	33
201C	4	4
201B	0	0
Average	**40**	**40**

Knowing the average mass fraction of dust derived Th (f_{dust}^{Th},), the flux of Th from dust can be calculated. The flux is the total amount of Th that has been deposited by dust during the lifetime of the soil profile, and is calculated by integrating (f_{dust}^{Th},) over the depth of the profile (*z*) using the average Th concentration in the profile $[Th]_{av}$ and the dry soil bulk density (*p*):

$$Th_{dust}^{tot} = [Th]_{av} \,.\, f_{dust}^{Th} \,.\, p \,.\, z \qquad \textit{Equation 10}$$

$$Th_{dust}^{tot} = 5600\ mg\ Th\ m^{-2}$$

where the dry bulk density is averaged to 1300 kg m^{-3} (Schaetzl and Thompson 2015) and soil profile depth is 2.2 m. To obtain an actual Th deposition rate, the average Th flux is divided by the soil age:

$$Th_{dust} = \frac{5600\ mg\ Th\ m^{-2}}{70\ 000\ years}$$

$$Th_{dust} = 0.080\ mg\ Th\ m^{-2}\ yr^{-1}$$

If the assumptions are correct, 0.08 milligrams of Th per square meter per year has, on average, been deposited during the last 70 ka of soil development. If elemental ratios of this dust is known, fluxes for other elements, such as the essential plant nutrient phosphorous (P) can be calculated. For example, Chadwick *et al.* (1999) used the average P/Th dust ratio to derive fluxes for P deposition in Hawaii from calculated Th/Hf fluxes. Chadwick *et al.* (1999) found that dust-derived P became the main source of P in soils older than 2 Ma because rock-derived P was completely leached from the soil by this time. If the aeolian dust at Reunion Island has a P/Th ratio identical to that of the continental crust, a like-for-like comparison between the rate of dust deposition at Hawaii and Reunion Island can be made:

$$P_{dust} = Th_{dust} \cdot \left(\frac{P}{Th}\right)_{dust} \qquad \textit{Equation 11}$$

$$P_{dust} = 5.0\ mg\ P\ m^{-2}\ yr^{-1}$$

where $\left(\frac{P}{Th}\right)_{dust}$ is the average P/Th ratio of the continental crust, derived from Rudnick and Gao (2003).

The results indicate that both Hawaii and Reunion Island experience dust deposition within the same order of magnitude (Table 15). However, the computed fluxes here assume that Th and Nb remain perfectly immobile in the soil and that aeolian dust has identical composition

as the continental crust. As a consequence, these results can only be used as a first order approximation for dust deposition at Reunion Island and more rigorous estimates would require accurate determination of the elemental composition of this dust.

***Table 15**: Calculated P addition rates for Reunion Island (this study) and Hawaii (Chadwick et al. 1999).*

Location	Tracer	Amount of P delivered in dust (mg m^{-2} yr^{-1})
Reunion Island	Th/Nb	5.0
Hawaii	Th/Hf	1.2

The source of the dust is probably from Australia (Figure 87), given its massive area, large deserts and south-easterly winds that blow into the southern Indian Ocean. However, there is little in the literature to support this thesis; most studies have investigated dust fluxes from Australia only in Tasman Sea sediments and Antarctica (e.g. Hesse 1992; Li *et al.* 2008). Furthermore, atmospheric sampling has not been performed in the southern Indian Ocean and so rates and composition of dust deposition is poorly constrained (Chester *et al.* 1991).

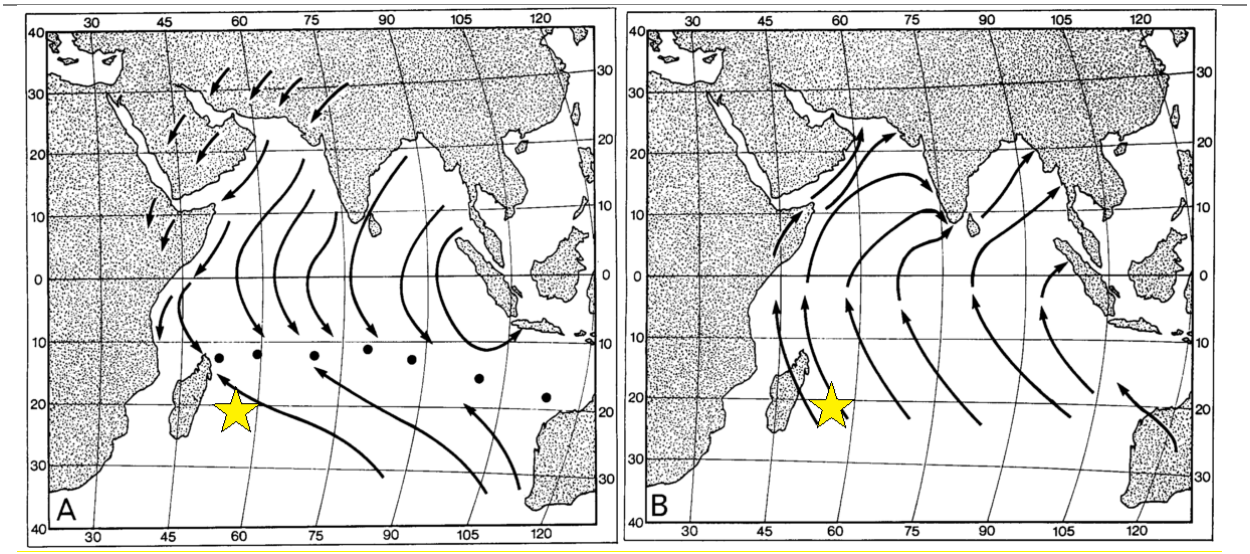

***Figure 87**: Mean wind flow directions over the Indian Ocean during (A) the northeast monsoon and (B) the southwest monsoon. The Inter Tropical Convergence Zone is represented by the dots. Stars indicate location of Reunion Island. Modified from Chester et al. (1991).*

6.4 Soil redox and pH at Reunion Island

Transition metals and REE provide an opportunity to trace changes in soil pH and redox because they can exist in several oxidation states. Of the elements analysed for this project, Ce is the most useful for tracing changes in redox (e.g. Braun *et al.* 1990). Its usefulness as a geochemical tracer stems from its two oxidation states that can occur within the range of most soil pH (5 – 9) and so unlike for Mn and Cu, the confounding effect of soil pH on Ce as a redox tracer is minimised (Laveuf *et al.* 2009).

The REE typically display a 3+ oxidation state, except for Ce which can be oxidised to 4+, and Eu which exists as Eu^{2+}. In its 3+ state, Ce is relatively mobile and like the other REE can be leached from primary phases during mineral dissolution. Upon oxidation to the tetravalent state however, Ce precipitates as cerianite (CeO_2) and is preferentially incorporated into Mn and Fe oxides over the other REE. If the same soil becomes reduced, the Mn and Fe oxides will dissolve and release the adsorbed REE, but Ce as cerianite will persist in the soil since it is insoluble even in reducing conditions. This process enriches Ce at the expense of the other REE, and so creates a positive cerium anomaly during this change from oxidising to reducing conditions. The larger the anomaly, the more frequent or intense these redox cycles (Laveuf *et al.* 2009). In order to calculate the cerium anomaly, the concentration of Ce in a soil sample is compared against the concentration of REE of neighbouring atomic masses e.g. La and Nd. Formally, the Ce anomaly is defined as:

$$\mathrm{Ce/Ce^*} = \frac{\frac{3Ce}{Ce_{ch}}}{\frac{2La}{La_{ch}} + \frac{Nd}{Nd_{ch}}} \qquad \textit{Equation 12}$$

where the subscript *ch* denotes the concentration of the REE in chondrites (Nakamura 1973). While there is no upper limit for the cerium anomaly, values < 1 reflect a negative anomaly and indicate that oxidation of Ce^{3+} has not occurred, while values > 1 indicate positive anomalies and suggest that changes in redox have occurred (Braun *et al.* 1990). By calculating the Ce anomaly for every sample from Reunion Island, changes in soil redox over

time can be inferred. The results from the chronosequence suggests that only the 70 ka and 2 Ma profiles have experienced frequent redox events (Figure 88).

The 70 ka profile shows a maximum cerium anomaly halfway down the profile while the 2 Ma profile has a very large Ce anomaly at the top of the profile. Additionally, anomalies are positive (i.e. > 1) throughout all three profiles suggesting Ce has been conserved relative to the other REE and therefore redox cycles have occurred in all soils. Maximum anomalies are seen in the B2 horizon in the 70 ka profile and in the upper A horizon in the 2 Ma profile.

These results could suggest that the frequency, or intensity of redox events are too low to be observed in soils younger than 20 ka at Reunion. In the 70 ka and 2 Ma soils maximum cerium anomalies are observed in the middle and surface of the profiles respectively, suggesting that redox cycles peak at a certain soil depth. Processes that could account for these anomalies include the transport of Ce-adsorbed Mn and Fe oxides via eluviation-illuviation or Ce^{4+} enriched dust deposition. Eluviation occurs when colloids, clays and oxides are removed, typically via solution, from upper to lower soil horizons. Since water is involved, it can affect the redox of the soil, particularly if a horizon remains saturated, generating the reducing conditions required for the mobilisation of Mn and Fe. The high Ce anomaly (> 9) at the surface of the 2 Ma soil suggests the A horizon has experienced several redox cycles that have preferentially enriched Ce^{4+} over Ce^{3+}. It is conceivable this has occurred from repeated wet and dry periods, particularly for the 2 Ma profile considering its high clay content and ability to remain saturated. For the 70 ka profile, these redox cycles have occurred about halfway down the profile, in the upper B2 horizon. The maximum goethite concentration also occurs at the same depth in the profile and suggest that the accumulation of Fe oxides could be associated with the mobilisation of Ce^{4+} during a change in soil redox.

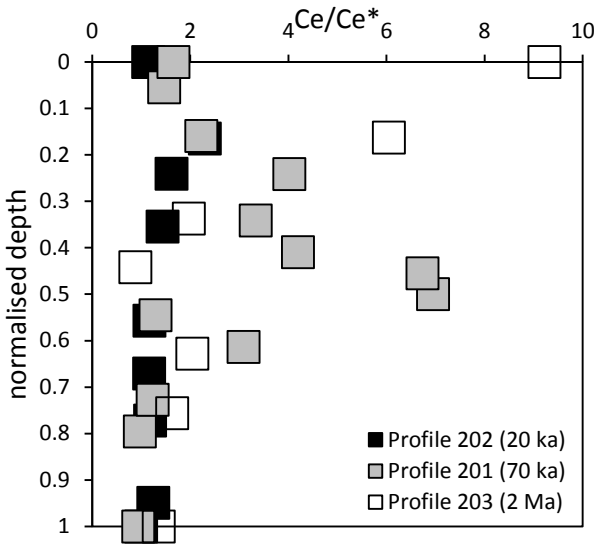

***Figure 88**: Cerium anomalies as a function of normalised soil depth.*

Caution must be used when interpreting the Ce anomaly because unrelated processes, such as dust deposition, could also explain increases in Ce^{4+} concentration relative to other REE. For example, Ce^{4+} can substitute for Zr^{4+} in zircon since both have identical charges and similar ionic radii (Thomas et al, 2003). If zircon is a major constituent of dust, then it is possible for the Ce anomaly to be completely explained by dust deposition rather than changes in soil redox. However, if this were the case at Reunion then the systematic depletion of Zr in the 70 ka and 2 Ma profiles should not have occurred. Additionally, even though there is probable dust input responsible for the increase in REE in the top 20% of the 70 ka and 2 Ma profiles, this dust is unlikely to be a major carrier of Ce^{4+} given its incompatibility with most REE minerals (Thomas *et al.* 2003).

The other transition elements analysed at Reunion, Mn and Cu, can similarly be used as proxies for changes in soil pH/Eh. Unlike Ce though, Cu and Mn cannot reliably quantify changes in soil redox because the mobility of both metals are also sensitive to changes in pH. Isolating the effects of redox and pH for these metals in the Reunion soils is therefore difficult, although possible if certain assumptions are made. Soils generally have a narrow range of pH, but this can vary markedly within the profile, particularly if there is acid-producing organic matter at the surface. Basaltic soils in high rainfall regions generally lie within a pH of 5 – 7 (Schaetzl and Thompson 2015), and this can be generalized for the soils

at Reunion Island. Doing this allows us to constrain the evolution of the soil when looking at the related Eh-pH diagrams.

Both Cu and Mn can be oxidised to their 2+ state under moderately oxidising conditions; for Mn, it can exist as a cation even under basic conditions, while Cu will correspondingly form insoluble hydroxides (Ryan 2014). At Reunion Island, Cu is depleted in the top half and enriched in bottom half of all three profiles (Figure 57), while Mn is progressively lost from the top to the bottom of the profiles, with loss increasing with soil age (Figure 56). The loss of Mn and Cu at the surface can be explained by the presence of organic acids. The subsequent enrichment of Cu at the bottom of all three profiles imply a change in pH or Eh such that the Cu^{2+} ion becomes immobilised, either by reduction to Cu(s) or precipitated as $Cu(OH)_2$ via an increase in pH. The simultaneous decrease in Mn, systematically throughout the profiles suggests that the soil profiles tend to become increasingly anoxic and/or acidic over time.

Another redox sensitive element that was analysed at Reunion Island is U. Uranium forms soluble U^{6+} under oxidising conditions and U^{4+} under reducing conditions. In soils with relatively oxic conditions U will form soluble UO_2^{2+}, and will precipitate as UO_2 under reducing conditions. In the 20 ka profile, U is lost in the upper A horizon, presumably as a result of acids produced from organic matter, and is then enriched in the upper B2 horizon (Figure 68). The effects of atmospheric addition of U are seen progressively as soil age increases, and the lack of U depletion suggests soil conditions are conducive to U accumulation, which only occurs if the soil is anoxic. However, U usually exists in most soils as UO_2^{2+} which has an extremely strong affinity for hydrous iron oxides and organic matter (e.g. Manceau *et al.* 1992), so explaining accumulation of U on a soil pH/Eh basis may not be required. Given that goethite, and other hydrated Fe oxides such as $Fe(OH)_3$ can exist in soil as long as the Eh/pH conditions are relatively mild (as are assumed to be for Reunion Island), then this hypothesis may account for the systematic accumulation of U added to the soil via dust deposition.

Distinguishing the proportion of U that is adsorbed onto Fe oxides versus clays or organic matter would require performing sequential extraction, a procedure that was not attempted. However, of the total soil U budget, generally less than 1% of the U in exists as exchangeable cations, with the majority found associated with amorphous Fe-oxide content (Pett-Ridge *et al.* 2007). Pett-Ridge et al (2007) observed that the adsorption of U onto amorphous Fe oxides in Hawaiian soils was found to peak in the intermediate aged soils (20 – 150 ka), which also reflected the greatest proportion of Fe-oxide content, suggesting that U adsorption on these oxide phases is the main control on the U budget in intermediate aged soils. Given that Hawaii and Reunion Island share similar climates and geology, it is not unreasonable to hypothesize that the majority of the U that is added via dust into the Reunion chronosequence is subsequently fixed onto Fe oxy-hydroxides.

6.4.1 Estimation of Eh/pH conditions at Reunion Island

The possible Eh-pH pathways the chronosequence has evolved through can be estimated from the gains and losses of the transition metals and REE. Such an estimate is not rigorous because no quantitative relationship linking mass transfer coefficients to Eh/pH have been determined, and confounding factors that can affect metal mobility (e.g. complexation with organic and inorganic ligands) can skew the modelled effects of redox and acidity on element mobility. Therefore, this approximation can only be viewed as one possible pathway the soils on Reunion have experienced.

There are essentially five variables that must combined in order to form a single evolutionary Eh/pH pathway:

1. The loss of REE (except Ce) with decreasing depth and increasing soil age.
2. The gain of Ce over time.
3. The loss of Mn with decreasing depth and increasing soil age.
4. The loss of Cu at the surface and gain of Cu in the bottom of all three profiles, with decreasing Cu over time.
5. The loss of U at the surface, and progressive enrichment at depth over time.

By integrating these five variables into a single Eh-pH diagram, a common pathway can be that to account for these gains and losses on the basis of changes in soil Eh and pH.

The assumptions made for this model are as follow:

1. Soil pH fluctuates between 5 – 8 (Schaetzl and Thompson 2015), both within each profile and across time.
2. The positive Ce anomaly is caused by the precipitation of CeO_2 and its residual enrichment over other REE, rather than from atmospheric dust.
3. Since isolating the effects of pH and Eh on element mobility has not been made quantitatively, it is assumed both have changed throughout the profiles and over time. Therefore, the modelled pathway is a product of both the Eh and pH component.

Manganese and Cu are all lost over time in the soils at Reunion Island (Figures 58) and imply they exist in their mobile, divalent species. Trivalent Ce is lost over time relative to Ce^{4+} (Figure 88) and imply a reduction in soil Eh. Uranium is enriched over time (Figure 69), and the most likely cause of its fixation in soil is its binding to Fe oxides as the UO_2^{2+} ion (Pett-Ridge *et al.* 2007). By combining these results, the Eh-pH conditions that the soils at Reunion Island have experienced can be constrained (Figure 89).

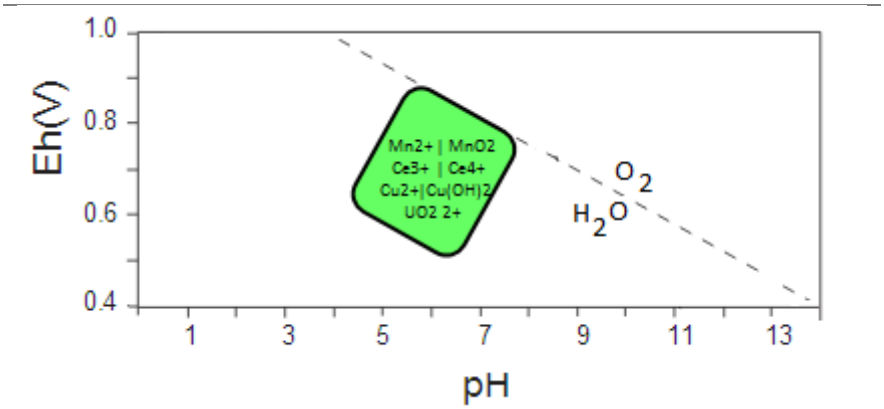

***Figure 89**: Eh-pH diagram showing the conditions likely present in the soils at Reunion Island. The green square covers an area such that it accounts for all suspected ionic species, based on their Eh-pH stability boundaries and the mobilities observed in the element profiles (Eh-pH information from Takeno, 2005).*

Chapter 7: Conclusion

The mineralogy and major and trace elements of three soil chronosequences from Reunion Island were analysed with the purpose of quantifying the effect of time on soil development. By constructing a series of element profiles, it was revealed that the soils from Reunion Island evolved through three stages. First, an initial period of rapid chemical weathering, causing most elements in the upper regolith to mobilise and be lost via leaching; a second period of dust-derived element addition and subsequent fixation into the upper regolith; and a final stage of total element depletion. The competing processes of element addition and loss defines the long-term nutrient budget of soils at Reunion Island. This is especially true for Cu and Mn, essential plant micronutrients that were progressively leached but were not added back into the soil by dust deposition. In this case, dust-derived elements become an important source of nutrients and may control the long-term fertility of rapidly weathered soils such as those on Reunion Island. Further research is needed to characterise the origin and composition of atmospherically-derived dust at Reunion Island to quantify the long-term sustainability of these soils.

In summary:

1. The rate of primary mineral loss is logarithmic and therefore fastest between the 20 and 70 ka soils, with plagioclase experiencing a 70% loss by mass. The abundance of secondary minerals correspondingly increases logarithmically, and by 2 Ma, halloysite forms nearly 40% of the soil by mass. The preferential formation of halloysite over gibbsite is at odds with the subtropical climate of Reunion Island and suggests Si is being conserved, possibly by biogenic processes.

2. The alkali and alkaline earth elements approach 50% depletion by 20 ka and > 99% depletion by 2 Ma. However, by 70 ka, most of these cations become enriched towards the surface by at least 5% (relative to the most depleted mass transfer coefficient in the upper half of the profile), and is hypothesised to occur as a result of atmospheric addition (from marine aerosol and dust) and subsequent fixation by clay

sorption. Enrichment of the soluble cations in the upper 70 ka profile follows the trend: (alkalis) Cs > Rb > Na, (alkaline earths) Sr > Ba > Mg, and (lanthanides) Heavy REE > Light REE. Cations with high hydration enthalpies are replaced with cations of lower hydration enthalpies on clays during ion-exchange, and explains why Cs is enriched at the expense of other soluble cations. For the REE, this model fails to explain the enrichment of the HREE over the LREE in the 70 ka profile. Instead, the formation of stable HREE complexes that can fractionate the REE such that the LREE are leached more readily, is a possible explanation.

3. A dust deposition rate of 0.08 mg Th m^{-2} yr^{-1} was calculated for the 70 ka profile using the Th/Nb ratio as a geochemical tracer, and is of a similar order of magnitude to dust deposition rates calculated for Hawaiian soils. By 2 Ma, most of the added alkali and alkaline earths have been leached completely, while the REE largely remain fixed in the soil, possibly because they form stable inorganic and organic complexes. Dust-deposited U and Th remain essentially immobile in all soils, likely as a result of fixation onto Fe oxyhydroxides and organic matter. The source of this dust is not known but is likely to be from Australia.

4. Leaching of transition metals and REE in the upper horizons is rapid and occurs within the first 20 ka of soil development, but is generally limited to the O and A horizons. The metals that do accumulate at the bottom of the profiles – Cu and Mn - are progressively lost over 2 Ma, probably because there is a decrease in soil pH and/or Eh which aids leaching. However, the lack of total depletion of Cu and Mn in the lower half of all profiles, even after 2 Ma, suggests that these elements either form immobile complexes, or changes in Eh and pH are such that it effectively immobilises them. Large cerium anomalies in the mid and upper 70 ka and 2 Ma profiles suggest redox cycles are limited to the upper C horizon in the 70 ka profile and to the A horizon in the 2 Ma profile, but this may be an artefact of Ce^{4+} addition via zircon laden dust.

References

Ahnert, F., 1967. The role of the equilibrium concept in the interpretation of landforms of fluvial erosion and deposition.

Aide, M.T. and Aide, C., 2012. Rare earth elements: their importance in understanding soil genesis. *ISRN Soil Science*, *2012*.

Albarède, F., Luais, B., Fitton, G., Semet, M., Kaminski, E., Upton, B.G.J., Bachelery, P. and Cheminée, J.L., 1997. The geochemical regimes of Piton de la Fournaise volcano (Réunion) during the last 530 000 years. *Journal of Petrology*, *38*(2), pp.171-201.

Ampe, C. and Langohr, R., 1993. Distribution and dynamics of shrub roots in recent coastal dune valley ecosystems of Belgium. *Geoderma*, *56*(1-4), pp.37-55.

Amundson, R., Richter, D.D., Humphreys, G.S., Jobbágy, E.G. and Gaillardet, J., 2007. Coupling between biota and earth materials in the critical zone. *Elements*, *3*(5), pp.327-332.

Anderson, S.P., Dietrich, W.E. and Brimhall, G.H., 2002. Weathering profiles, mass-balance analysis, and rates of solute loss: Linkages between weathering and erosion in a small, steep catchment. *Geological Society of America Bulletin*, *114*(9), pp.1143-1158.

Anderson, S.P., von Blanckenburg, F. and White, A.F., 2007. Physical and chemical controls on the critical zone. *Elements*, *3*(5), pp.315-319.

Bain, D.C., Mellor, A., Robertson-Rintoul, M.S.E. and Buckland, S.T., 1993. Variations in weathering processes and rates with time in a chronosequence of soils from Glen Feshie, Scotland. *Geoderma*, *57*(3), pp.275-293.

Brantley, S.L., 2008. Kinetics of mineral dissolution. In *Kinetics of water-rock interaction* (pp. 151-210). Springer New York.

Brantley, S.L., Goldhaber, M.B. and Ragnarsdottir, K.V., 2007. Crossing disciplines and scales to understand the critical zone. *Elements*, *3*(5), pp.307-314.

Braun, J.J., Pagel, M., Muller, J.P., Bilong, P., Michard, A. and Guillet, B., 1990. Cerium anomalies in lateritic profiles. *Geochimica et Cosmochimica Acta*, *54*(3), pp.781-795.

Brimhall, G.H. and Dietrich, W.E., 1987. Constitutive mass balance relations between chemical composition, volume, density, porosity, and strain in metasomatic hydrochemical systems: results on weathering and pedogenesis. *Geochimica et Cosmochimica Acta*, *51*(3), pp.567-587.

Buggle, B., Glaser, B., Hambach, U., Gerasimenko, N. and Marković, S., 2011. An evaluation of geochemical weathering indices in loess–paleosol studies. *Quaternary International*, *240*(1), pp.12-21.

Burkins, D.L., Blum, J.D., Brown, K., Reynolds, R.C. and Erel, Y., 1999. Chemistry and mineralogy of a granitic, glacial soil chronosequence, Sierra Nevada Mountains, California. *Chemical Geology*, *162*(1), pp.1-14.

Chabaux, F., Granet, M., Pelt, E., France-Lanord, C. and Galy, V., 2006. 238 U–234 U–230 Th disequilibria and timescale of sedimentary transfers in rivers: clues from the Gangetic plain rivers. *Journal of Geochemical Exploration*, *88*(1), pp.373-375.

Chadwick, O.A., Derry, L.A., Vitousek, P.M., Huebert, B.J. and Hedin, L.O., 1999. Changing sources of nutrients during four million years of ecosystem development. *Nature*, *397*(6719), pp.491-497.

Chester, R., Berry, A.S. and Murphy, K.J.T., 1991. The distributions of particulate atmospheric trace metals and mineral aerosols over the Indian Ocean. *Marine Chemistry*, *34*(3), pp.261-290.

Chevallier, L. and Bachèlery, P., 1981. Evolution structurale du volcan actif du Piton de la Fournaise, Ile de la Réunion—Océan indien occidental. *Bulletin volcanologique*, *44*(4), pp.723-741.

Chou, L.E.I., Garrels, R.M. and Wollast, R., 1989. Comparative study of the kinetics and mechanisms of dissolution of carbonate minerals. *Chemical Geology*, *78*(3), pp.269-282.

Coppin, F., Berger, G., Bauer, A., Castet, S. and Loubet, M., 2002. Sorption of lanthanides on smectite and kaolinite. *Chemical Geology*, *182*(1), pp.57-68.

Cornu, S., Lucas, Y., Lebon, E., Ambrosi, J.P., Luizão, F., Rouiller, J., Bonnay, M. and Neal, C., 1999. Evidence of titanium mobility in soil profiles, Manaus, central Amazonia. *Geoderma*, *91*(3), pp.281-295.

Crews, T.E., Kitayama, K., Fownes, J.H., Riley, R.H., Herbert, D.A., Mueller-Dombois, D. and Vitousek, P.M., 1995. Changes in soil phosphorus fractions and ecosystem dynamics across a long chronosequence in Hawaii. *Ecology*, *76*(5), pp.1407-1424.

Dessert, C., Dupré, B., Gaillardet, J., François, L.M. and Allegre, C.J., 2003. Basalt weathering laws and the impact of basalt weathering on the global carbon cycle. *Chemical Geology*, *202*(3), pp.257-273.

Dosseto, A., Buss, H.L. and Suresh, P.O., 2012. Rapid regolith formation over volcanic bedrock and implications for landscape evolution. *Earth and Planetary Science Letters*, *337*, pp.47-55.

Fisk, M.R., Upton, B.G.J., Ford, C.E. and White, W.M., 1988. Geochemical and experimental study of the genesis of magmas of Reunion Island, Indian Ocean. *Journal of Geophysical Research: Solid Earth*, *93*(B5), pp.4933-4950.

Goldich, S.S., 1938. A study in rock-weathering. *The Journal of Geology*, pp.17-58.

Heier, K.S., 1960. *Petrology and geochemistry of high-grade metamorphic and igneous rocks on Langøy, Northern Norway* (No. 207). I kommisjon hos Aschehoug.

Heimsath, A.M., Dietrich, W.E., Nishiizumi, K. and Finkel, R.C., 1997. The soil production function and landscape equilibrium. *Nature*, *388*(6640), pp.358-361.

Hesse, P.P., 1994. The record of continental dust from Australia in Tasman Sea sediments. *Quaternary Science Reviews*, *13*(3), pp.257-272.

Huang, C., Gong, Z. and He, Y., 2004. Elemental geochemistry of a soil chronosequence on basalt on northern Hainan Island, China. *CHINESE JOURNAL OF GEOCHEMISTRY-ENGLISH LANGUAGE EDITION-*, *23*(3), pp.245-254.

Huggett, R.J., 1998. Soil chronosequences, soil development, and soil evolution: a critical review. *Catena*, *32*(3), pp.155-172.

Humphreys, G.S. and Wilkinson, M.T., 2007. The soil production function: a brief history and its rediscovery. *Geoderma*, *139*(1), pp.73-78.

Jenny, H., 1941 *Factors of soil formation: a system of quantitative pedology*. Courier Corporation.

Join, J.L., Folio, J.L. and Robineau, B., 2005. Aquifers and groundwater within active shield volcanoes. Evolution of conceptual models in the Piton de la Fournaise volcano. *Journal of Volcanology and Geothermal Research*, *147*(1), pp.187-201.

Jongmans, A.G., Nieuwenhuyse, A., Buurman, P., van Doesburg, J.D.J., van Oort, F. and Jaunet, A.M., 1994. Inheritance of 2: 1 phyllosilicates in Costa Rican andisols. *Soil Science Society of America Journal*, *58*(2), pp.494-501.

Kleber, M., Schwendenmann, L., Veldkamp, E., Rößner, J. and Jahn, R., 2007. Halloysite versus gibbsite: silicon cycling as a pedogenetic process in two lowland neotropical rain forest soils of La Selva, Costa Rica. *Geoderma*, *138*(1), pp.1-11.

Kurtz, A.C., Derry, L.A., Chadwick, O.A. and Alfano, M.J., 2000. Refractory element mobility in volcanic soils. *Geology*, *28*(8), pp.683-686.

Laveuf, C. and Cornu, S., 2009. A review on the potentiality of rare earth elements to trace pedogenetic processes. *Geoderma*, *154*(1), pp.1-12.

Li, F., Ginoux, P. and Ramaswamy, V., 2008. Distribution, transport, and deposition of mineral dust in the Southern Ocean and Antarctica: Contribution of major sources. *Journal of Geophysical Research: Atmospheres*, *113*(D10).

Louvat, P. and Allègre, C.J., 1997. Present denudation rates on the island of Reunion determined by river geochemistry: basalt weathering and mass budget between chemical and mechanical erosions. *Geochimica et Cosmochimica Acta*, *61*(17), pp.3645-3669.

Lyell, C., 1837. Principles of geology: Being an inquiry how far the former changes of the Earth's surface are referable to causes now in operation (Vol. 1). J. Kay, jun. & brother.

Manceau, A., Charlet, L., Boisset, M.C., Didier, B. and Spadini, L., 1992. Sorption and speciation of heavy metals on hydrous Fe and Mn oxides. From microscopic to macroscopic. *Applied Clay Science*, *7*(1-3), pp.201-223.

Masuda, A., Nakamura, N. and Tanaka, T., 1973. Fine structures of mutually normalized rare-earth patterns of chondrites. *Geochimica et Cosmochimica Acta*, *37*(2), pp.239-248.

McDougall, I. and Compston, W., 1965. Strontium isotope composition and potassium-rubidium ratios in some rocks from Reunion and Rodriguez, Indian Ocean. *Nature*, *207*, pp.252-253.

McDougall, I., 1971. The geochronology and evolution of the young volcanic island of Réunion, Indian Ocean. *Geochimica et Cosmochimica Acta*, *35*(3), pp.261-288.

McDougall, I., Upton, B.G.J. and Wadsworth, W.J., 1965. A geological reconnaissance of Rodriguez island, Indian ocean.

Middelburg, J.J., van der Weijden, C.H. and Woittiez, J.R., 1988. Chemical processes affecting the mobility of major, minor and trace elements during weathering of granitic rocks. *Chemical Geology*, *68*(3-4), pp.253-273.

Minasny, B., McBratney, A.B. and Salvador-Blanes, S., 2008. Quantitative models for pedogenesis—A review. *Geoderma*, *144*(1), pp.140-157.

Montgomery, D.R., 2007. Soil erosion and agricultural sustainability. *Proceedings of the National Academy of Sciences*, *104*(33), pp.13268-13272.

Morgan, W.J., 1981. 13. Hotspot tracks and the opening of the Atlantic and Indian Oceans. *The oceanic lithosphere*, *7*, p.443.

Navarre-Sitchler, A. and Brantley, S., 2007. Basalt weathering across scales. *Earth and Planetary Science Letters*, *261*(1), pp.321-334.

Nesbitt, H.W., 1979. Mobility and fractionation of rare earth elements during weathering of a granodiorite.

Nesbitt, H.W. and Markovics, G., 1980. Chemical processes affecting alkalis and alkaline earths during continental weathering. Geochimica et Cosmochimica Acta, 44(11), pp.1659-1666.

Oehler, J.F., Labazuy, P. and Lénat, J.F., 2003, April. Debris avalanche deposits on the submarine flanks of Reunion Island. Implications on its evolution model. In *EGS-AGU-EUG Joint Assembly* (Vol. 1, p. 6258).

Pearce, J.A., 2008. Geochemical fingerprinting of oceanic basalts with applications to ophiolite classification and the search for Archean oceanic crust. *Lithos*, *100*(1), pp.14-48.
Pett-Ridge, J.C., Monastra, V.M., Derry, L.A. and Chadwick, O.A., 2007. Importance of atmospheric inputs and Fe-oxides in controlling soil uranium budgets and behavior along a Hawaiian chronosequence. *Chemical Geology*, *244*(3), pp.691-707.
Piccolo, M.C., Neill, C. and Cerri, C.C., 1994. Natural abundance of 15N in soils along forest-to-pasture chronosequences in the western Brazilian Amazon Basin. *Oecologia*, *99*(1-2), pp.112-117.
Pope, G.A., Meierding, T.C. and Paradise, T.R., 2002. Geomorphology's role in the study of weathering of cultural stone. *Geomorphology*, *47*(2), pp.211-225.
Porder, S., Hilley, G.E. and Chadwick, O.A., 2007. Chemical weathering, mass loss, and dust inputs across a climate by time matrix in the Hawaiian Islands. Earth and Planetary Science Letters, 258(3), pp.414-427.
Rad, S.D., Allègre, C.J. and Louvat, P., 2007. Hidden erosion on volcanic islands. *Earth and Planetary Science Letters*, *262*(1), pp.109-124.
Railsback, L.B., 2006. Some fundamentals of mineralogy and geochemistry. *On-line book, quoted from: www.gly.uga.edu/railsback.*
Regan, E.J., 1977. *The natural energy basis for soils and urban growth in Florida*.
Reheis, M.C., 1990. Influence of climate and eolian dust on the major-element chemistry and clay mineralogy of soils in the northern Bighorn Basin, USA. *Catena*, *17*(3), pp.219-248.
Runge, E.C.A., 1973. Soil development sequences and energy models. *Soil Science*, *115*(3), pp.183-193.
Rudnick R.L. and S. Gao, 3.01 - Composition of the Continental Crust, In Treatise on Geochemistry, edited by Heinrich D. Holland and Karl K. Turekian, Pergamon, Oxford, 2003, Pages 1-64
Ryan, P., 2014. *Environmental and low temperature geochemistry*. John Wiley & Sons.
Sawhney, B.L. and Norrish, K., 1971. pH dependent cation exchange capacity: minerals and soils of tropical regions. *Soil Science*, *112*(3), pp.213-215.
Schaetzl, R.J. and Thompson, M.L., 2015. *Soils*. Cambridge University Press.
Schwertmann, U. and Murad, E., 1983. Effect of pH on the formation of goethite and hematite from ferrihydrite. *Clays and Clay Minerals*, *31*(4), pp.277-284.
Simonson, R.W., 1995. Airborne dust and its significance to soils. *Geoderma*, *65*(1), pp.1-43.
Smeck, N.E., Runge, E.C.A. and Mackintosh, E.E., 1983. Dynamics and genetic modelling of soil systems. *Developments in Soil Science*, *11*, pp.51-81.
Smith, D.W., 1977. Ionic hydration enthalpies. *J. Chem. Educ*, *54*(9), p.540.
Takeno, N., 2005. Atlas of Eh-pH diagrams. Geological survey of Japan open file report, 419, p.102.
Taylor, A. and Blum, J.D., 1995. Relation between soil age and silicate weathering rates determined from the chemical evolution of a glacial chronosequence. *Geology*, *23*(11), pp.979-982.
Tegen, I. and Lacis, A.A., 1996. Modeling of particle size distribution and its influence on the radiative properties of mineral dust aerosol. *JOURNAL OF GEOPHYSICAL RESEARCH-ALL SERIES-*, *101*, pp.19-237.
Thomas, J.B., Bodnar, R.J., Shimizu, N. and Chesner, C.A., 2003. Melt inclusions in zircon. *Reviews in mineralogy and geochemistry*, *53*(1), pp.63-87.
Tyler, G. and Olsson, T., 2002. Conditions related to solubility of rare and minor elements in forest soils. *Journal of Plant Nutrition and Soil Science*, *165*(5), pp.594-601.

Van Dooremolen, W.A., Wielemaker, W.G., Van Breemen, N., Meijer, E.M. and van REEWIJK, L.P., 1990. Chemistry and mineralogy of andosols of various age in a soil chronosequence on andesitic lahars in Costa Rica. *Chemical Geology*, *84*(1-4), pp.139-141.

Velbel, M.A., 1993. Formation of protective surface layers during silicate-mineral weathering under well-leached, oxidizing conditions. *American Mineralogist*, *78*, pp.405-405.

Vitousek, P.M. and Farrington, H., 1997. Nutrient limitation and soil development: experimental test of a biogeochemical theory. *Biogeochemistry*, *37*(1), pp.63-75.

Volobuev, V.R. and Ponomarev, D.G., 1977. Some thermodynamic characteristics of soil mineral associations. *Pochvovedenie*.

VR Volobuev., 1965. Ecology of Soils.. Translated from the Russian edition (1963) by A. Gourevich. Israel Program for Scientific Translations, Jerusalem; Davey, New York, 1964. iv+ 260 pp. Illus. American Association for the Advancement of Science.

White, A.F., Blum, A.E., Schulz, M.S., Bullen, T.D., Harden, J.W. and Peterson, M.L., 1996. Chemical weathering rates of a soil chronosequence on granitic alluvium: I. Quantification of mineralogical and surface area changes and calculation of primary silicate reaction rates. *Geochimica et Cosmochimica Acta*, *60*(14), pp.2533-2550.

White, A.F. and Brantley, S.L., 1995. Chemical weathering rates of silicate minerals: an overview. *Chemical Weathering Rates of Silicate Minerals*, *31*, pp.1-22.

White, A.F. and Brantley, S.L., 2003. The effect of time on the weathering of silicate minerals: why do weathering rates differ in the laboratory and field?. Chemical Geology, 202(3), pp.479-506.

Zielinski, R.A., 1975. Trace element evaluation of a suite of rocks from Reunion Island, Indian Ocean. *Geochimica et Cosmochimica Acta*, *39*(5), pp.713-734.

Appendices

Appendix A: Reunion Island basalt Th/Yb Nb/Yb data

Reunion Island basalts analysed by Albarede *et al.* (1997)

Sample	Nb (ppm)	Yb (ppm)	Th (ppm)	Th/Yb	Nb/Yb
R1301	28.0	1.97	2.05	1.04	14.2
O2201	9.6	1.12	1.23	1.10	8.57
R1201	24.2	1.83	2.06	1.13	13.2
O1301	24.8	2.04	2.05	1.00	12.1
S1901	28.2	2.13	2.49	1.17	13.2
S1401	31.1	2.10	2.40	1.14	14.8
T1902	12.7	1.10	0.96	0.87	11.5
T2101	13.1	1.08	1.03	0.95	12.1
T1602	13.1	0.97	0.93	0.96	13.5
L2001	24.0	2.22	2.68	1.21	10.8
P1601	15.0	1.16	1.10	0.95	12.9
P1601	12.9	1.33	1.40	1.05	9.70
P1401	22.6	1.97	2.25	1.14	11.4
N2201	21.8	2.16	2.35	1.09	10.0
O2202	22.6	2.15	2.34	1.09	10.5
M1701	21.8	2.21	2.48	1.12	9.86
RP27	41.5	2.27	3.14	1.38	18.2
RP28	66.4	2.87	4.98	1.74	23.1
RP29	44.1	2.75	3.26	1.19	16.0
RP30	41.9	2.34	3.03	1.29	17.9
RP31	26.5	1.76	1.95	1.11	15.0
RP32	30.1	1.90	2.25	1.18	15.8
RP33	31.5	2.20	2.80	1.27	14.3

Appendix B: Element concentrations & Mass-transfer coefficients (tElement)

PROFILE 201 – ALKALIS

SAMPLE	Na (ppm)	2σ	tNa	Rb (ppm)	2σ	tRb	Cs (ppm)	2σ	tCs
201A	6309	33.9	0.00	1.63	0.20	0.00	0.017	0.005	0.00
201B	2737	86	-0.48	2.00	0.13	0.48	0.059	0.006	3.29
201C	1246	24	-0.81	0.47	0.055	-0.73	0.048	0.007	1.71
201D	932	23	-0.94	0.91	0.054	-0.77	0.075	0.002	0.87
201DBIS	2862	37	-0.60	2.31	0.043	0.25	0.050	0.002	1.69
201E	36	0.27	-1.00	0.09	0.007	-0.97	0.010	0.002	-0.67
201F	35	0.36	-1.00	0.10	0.014	-0.97	0.013	0.004	-0.62
201G	59	0.34	-1.00	0.25	0.018	-0.94	0.040	0.002	-0.07
201H	289	0.45	-0.99	0.59	0.027	-0.90	0.073	0.003	0.18
201I	1450	184	-0.94	1.53	0.046	-0.77	0.124	0.003	0.83
201J	4048	535	-0.87	2.82	0.032	-0.66	0.166	0.016	1.00
201K	2645	156	-0.90	6.74	0.166	-0.03	0.199	0.010	1.81
201L	3089	226	-0.86	3.97	0.085	-0.30	0.204	0.005	2.55

PROFILE 202 – ALKALIS

SAMPLE	Na (ppm)	2σ	tNa	Rb (ppm)	2σ	tRb	Cs (ppm)	2σ	tCs
202B	30491	180.76	0.00	35.75	0.189	0.00	0.262	0.008	0.00
202C	25060	195.27	-0.08	31.34	2.062	-0.02	0.243	0.004	0.04
202D	27055	200.79	-0.07	30.44	0.917	-0.11	0.240	0.014	-0.04
202E	22811	14.40	-0.16	26.74	4.153	-0.16	0.239	0.043	0.02
202F	21788	50.89	-0.12	26.37	0.706	-0.09	0.205	0.007	-0.04
202G	15607	20.96	-0.44	24.13	1.434	-0.19	0.216	0.012	-0.10
202H	3048	176.46	-0.92	8.69	0.138	-0.40	0.195	0.011	-0.39
202I	1078	1574.58	-0.99	1.37	0.071	-0.77	0.120	0.010	-0.85
202J	2315	64.65	-0.98	4.87	0.195	-0.95	0.150	0.003	-0.89

PROFILE 203 – ALKALIS

SAMPLE	Na (ppm)	2σ	tNa	Rb (ppm)	2σ	tRb	Cs (ppm)	2σ	tCs
203A	569.6	330.14	-0.96	0.362	0.007	-0.91	0.047	0.004	0.12
203B	340.1	4.27	-0.98	0.366	0.003	-0.93	0.033	0.002	-0.35
203C	149.1	5.22	-0.99	0.260	0.009	-0.95	0.028	0.002	-0.45
203D	83.0	0.70	-1.00	0.773	0.031	-0.84	0.102	0.007	1.08
203E	138.5	0.51	-0.99	1.015	0.004	-0.76	0.156	0.005	2.69
203F	80.2	0.21	-1.00	0.792	0.032	-0.87	0.107	0.004	0.67
203G	281.6	3.48	-0.99	2.286	0.086	-0.76	0.213	0.007	1.21

PROFILE 201 – ALKALINE EARTHS

SAMPLE	Mg (ppm)	2σ	tMg	Sr (ppm)	2σ	tSr	Ba (ppm)	2σ	tBa
201A	87285	2651	0.00	97.0	11.20	0.00	63.4	7.87	0.00
201B	66972	1053	-0.07	53.4	2.74	-0.34	28.4	1.48	-0.46
201C	85830	1209	-0.08	27.5	2.02	-0.73	10.0	0.79	-0.85
201D	32290	934	-0.85	21.6	0.88	-0.91	11.4	0.36	-0.93
201DBIS	51146	1674	-0.48	50.2	1.30	-0.54	31.3	0.37	-0.57
201E	37513	1979	-0.77	2.1	0.11	-0.99	2.4	0.13	-0.98
201F	38506	962	-0.79	1.6	0.06	-0.99	2.1	0.04	-0.98
201G	40123	819	-0.82	2.3	0.05	-0.99	2.9	0.01	-0.98
201H	23909	387	-0.93	8.6	0.20	-0.98	5.6	0.00	-0.98
201I	21393	1239	-0.94	38.5	0.88	-0.90	17.2	0.74	-0.93
201J	18546	379	-0.96	117.3	2.72	-0.76	44.0	1.01	-0.86
201K	24660	184	-0.93	68.0	1.19	-0.84	43.4	0.91	-0.84
201L	29198	305	-0.90	96.9	0.43	-0.71	55.9	0.62	-0.75

PROFILE 202 – ALKALINE EARTHS

SAMPLE	Mg (ppm)	2σ	tMg	Sr (ppm)	2σ	tSr	Ba (ppm)	2σ	tBa
202B	27685	289	0.00	500.8	10.48	0.00	392.7	10.18	0.00
202C	30882	421	0.25	348.5	20.76	-0.22	458.1	30.67	0.30
202D	34912	784	0.32	414.4	7.62	-0.13	255.3	8.04	-0.32
202E	35607	1045	0.45	373.7	55.19	-0.16	244.4	41.18	-0.30
202F	35133	608	0.56	349.1	7.60	-0.14	231.6	7.41	-0.27
202G	41633	1290	0.64	203.9	11.19	-0.56	189.7	11.29	-0.47
202H	21795	320	-0.35	36.3	0.36	-0.94	138.2	2.21	-0.71
202I	13399	204	-0.84	9.4	0.41	-0.99	116.2	3.63	-0.90
202J	10827	333	-0.92	37.7	1.92	-0.98	36.7	1.49	-0.98

PROFILE 203 – ALKALINE EARTHS

SAMPLE	Mg (ppm)	2σ	tMg	Sr (ppm)	2σ	tSr	Ba (ppm)	2σ	tBa
203A	11567	209	-0.95	3.98	0.06	-0.98	565.8	18.08	2.50
203B	9330	168	-0.97	6.43	0.15	-0.98	151.4	5.45	-0.24
203C	11828	120	-0.96	2.37	0.07	-0.99	178.4	6.22	-0.07
203D	11070	148	-0.96	2.95	0.13	-0.99	86.4	3.81	-0.54
203E	11307	150	-0.95	11.74	0.40	-0.95	29.8	0.85	-0.82
203F	12008	94	-0.96	2.75	0.06	-0.99	22.9	0.48	-0.91
203G	11118	207	-0.98	6.65	0.28	-0.99	35.6	1.57	-0.90

PROFILE 201 – TRANSITION METALS

SAMPLE	Ti (ppm)	2σ	tTi	Zr (ppm)	2σ	tZr	Ta (ppm)	2σ	tTa
201A	13939	343	0.00	168	21.9	0.00	0.99	0.137	0.00
201B	12147	308	0.05	138	7.5	-0.01	1.00	0.048	0.22
201C	15737	262	0.06	179	11.6	0.00	1.22	0.045	0.16
201D	28935	337	-0.15	351	13.2	-0.14	2.56	0.087	0.07
201DBIS	15175	297	-0.04	184	5.1	-0.04	1.19	0.027	0.06
201E	29201	1830	0.12	324	14.5	0.03	2.02	0.065	0.09
201F	27604	186	-0.08	363	19.3	0.01	2.49	0.308	0.17
201G	31915	578	-0.11	389	9.2	-0.10	2.73	0.050	0.08
201H	37795	250	-0.28	538	11.4	-0.15	3.89	0.165	0.05
201I	34908	216	-0.39	572	13.2	-0.18	4.36	0.151	0.07
201J	26125	283	-0.63	623	16.9	-0.27	4.68	0.075	-0.06
201K	43739	776	-0.27	487	10.8	-0.32	4.39	0.051	0.04
201L	35412	591	-0.27	392	4.0	-0.33	3.56	0.175	0.03

PROFILE 201 – TRANSITION METALS (CONT'D)

SAMPLE	Mn (ppm)	2σ	tMn	Cu (ppm)	2σ	tCu	Nb (ppm)	2σ
201A	1392	34.8	0.00	50.0	6.22	0.00	14.8	1.71
201B	1216	27.2	0.05	69.0	4.34	0.66	12.3	0.75
201C	1545	28.6	0.04	95.4	6.03	0.79	15.8	1.21
201D	1464	24.1	-0.57	105.8	2.77	-0.13	36.0	1.27
201DBIS	1342	30.5	-0.15	94.6	2.56	0.67	16.8	0.46
201E	2535	130.8	-0.03	174.0	8.68	0.85	27.7	1.38
201F	1852	19.1	-0.38	195.6	8.37	0.83	31.7	1.32
201G	1128	24.0	-0.68	161.9	3.35	0.26	37.8	0.82
201H	607	6.1	-0.88	68.8	0.65	-0.63	55.4	0.97
201I	972	19.8	-0.83	74.0	2.58	-0.64	60.8	1.70
201J	1051	4.7	-0.85	76.3	1.12	-0.70	74.5	6.46
201K	1222	13.4	-0.80	93.2	2.47	-0.57	63.4	2.16
201L	1132	14.0	-0.77	94.8	2.04	-0.46	51.5	0.99

PROFILE 202 – TRANSITION METALS

SAMPLE	Ti (ppm)	2σ	tTi	Zr (ppm)	2σ	tZr	Ta (ppm)	2σ	tTa
202B	16046	323.7	0.00	312.3	3.52	0.00	2.576	0.027	0.00
202C	14429	207.9	0.00	283.2	17.09	0.01	2.384	0.100	0.03
202D	16075	358.5	0.05	314.2	4.89	0.06	2.594	0.034	0.06
202E	17120	306.8	0.20	282.2	46.30	0.02	2.302	0.324	0.01
202F	15863	210.7	0.22	263.0	7.73	0.04	2.105	0.133	0.00
202G	18994	316.4	0.29	290.9	13.48	0.01	2.388	0.142	0.01
202H	22055	427.6	0.13	392.7	11.95	0.03	3.066	0.113	-0.02
202I	26503	405.8	-0.44	974.5	37.75	0.05	6.044	0.149	-0.21
202J	51792	1272.0	-0.35	718.0	27.78	-0.54	10.037	0.191	-0.22

PROFILE 202 – TRANSITION METALS (CONT'D)

SAMPLE	Mn (ppm)	2σ	tMn	Cu (ppm)	2σ	tCu	Nb (ppm)	2σ
202B	2018.3	27.60	0.00	10.39	0.146	0.00	40.51	0.770
202C	2373.2	40.05	0.31	16.15	0.951	0.74	36.28	2.407
202D	1944.9	33.65	0.01	21.30	0.699	1.15	38.58	1.033
202E	1909.2	29.60	0.06	26.18	4.157	1.84	36.01	5.931
202F	1984.6	33.56	0.21	19.33	0.694	1.29	32.94	1.094
202G	2300.7	75.65	0.24	28.56	1.026	1.99	37.20	2.049
202H	1324.8	8.32	-0.46	38.25	1.064	2.02	49.43	1.607
202I	378.5	5.15	-0.94	18.07	0.806	-0.41	120.08	4.895
202J	492.2	12.67	-0.95	18.64	0.679	-0.64	201.41	8.367

PROFILE 203 – TRANSITION METALS

SAMPLE	Ti (ppm)	2σ	tTi	Zr (ppm)	2σ	tZr	Ta (ppm)	2σ	tTa
203A	28315	412.7	-0.20	368.1	4.24	-0.14	2.395	0.048	-0.05
203B	32469	184.7	-0.26	461.1	13.61	-0.12	2.998	0.110	-0.03
203C	30800	312.2	-0.27	447.3	14.91	-0.12	3.022	0.162	0.01
203D	30901	590.7	-0.25	441.9	18.59	-0.11	3.006	0.058	0.03
203E	28472	458.0	-0.20	375.8	7.27	-0.13	2.573	0.118	0.02
203F	23287	371.1	-0.57	554.8	5.78	-0.15	3.737	0.067	-0.02
203G	27236	697.2	-0.66	651.3	26.67	-0.33	4.781	0.148	-0.17

PROFILE 203 – TRANSITION METALS (CONT'D)

SAMPLE	Mn (ppm)	2σ	tMn	Cu (ppm)	2σ	tCu	Nb (ppm)	2σ
203A	1535.2	24.88	-0.57	138.45	1.865	0.09	37.71	0.66
203B	1603.7	24.10	-0.63	180.22	3.904	0.15	46.21	1.05
203C	1153.5	11.79	-0.73	168.74	6.806	0.12	44.56	1.18
203D	639.9	6.22	-0.84	140.58	5.370	-0.05	43.74	2.12
203E	889.5	11.58	-0.75	150.60	4.196	0.18	37.78	1.07
203F	630.7	10.70	-0.88	85.51	2.486	-0.56	57.34	0.84
203G	800.4	8.31	-0.90	75.55	2.106	-0.74	85.87	3.06

PROFILE 201 – LANTHANIDES

SAMPLE	La (ppm)	2σ	tLa	Ce (ppm)	2σ	tCe	Nd (ppm)	2σ	tNd
201A	13.96	1.93	0.00	31.8	4.69	0.00	20.3	2.90	0.00
201B	11.48	0.58	-0.01	27.4	1.19	0.04	17.4	0.89	0.03
201C	9.76	0.43	-0.34	32.6	1.34	-0.04	20.1	0.96	-0.07
201D	10.84	0.55	-0.68	98.9	6.19	0.28	28.4	1.34	-0.42
201DBIS	13.60	0.21	-0.14	43.8	0.08	0.21	22.1	0.40	-0.04
201E	7.40	0.20	-0.72	150.7	5.73	1.52	19.0	0.75	-0.50
201F	4.75	0.74	-0.84	107.8	14.93	0.58	16.8	2.39	-0.61
201G	4.71	0.17	-0.87	68.0	1.56	-0.16	17.3	0.05	-0.67
201H	9.84	0.38	-0.81	111.8	3.45	-0.06	35.5	0.68	-0.53
201I	16.02	0.51	-0.72	187.3	5.04	0.43	40.3	0.75	-0.52
201J	20.37	0.32	-0.71	126.0	2.30	-0.21	45.7	1.80	-0.55
201K	22.36	0.69	-0.63	76.6	0.91	-0.44	28.3	0.61	-0.67
201L	19.80	0.60	-0.59	76.1	2.00	-0.31	24.6	0.91	-0.65

PROFILE 201 – LANTHANIDES (CONT'D)

SAMPLE	Sm (ppm)	2σ	tSm	Eu (ppm)	2σ	tEu	Yb (ppm)	2σ	tYb
201A	5.32	0.81	0.00	1.81	0.22	0.00	2.02	0.29	0.00
201B	4.54	0.22	0.03	1.52	0.06	0.01	1.74	0.13	0.04
201C	5.67	0.21	0.00	1.89	0.05	-0.02	2.38	0.06	0.11
201D	9.14	0.50	-0.30	2.95	0.14	-0.33	3.45	0.17	-0.30
201DBIS	5.89	0.13	-0.03	2.03	0.03	-0.01	2.21	0.04	-0.03
201E	6.69	0.13	-0.33	2.26	0.08	-0.33	3.22	0.09	-0.15
201F	5.56	0.80	-0.51	1.79	0.28	-0.54	2.13	0.28	-0.51
201G	5.10	0.09	-0.63	1.55	0.01	-0.67	1.50	0.05	-0.71
201H	13.49	0.64	-0.32	4.03	0.11	-0.41	4.43	0.15	-0.41
201I	13.43	0.52	-0.39	4.50	0.23	-0.40	5.41	0.17	-0.35
201J	12.06	0.15	-0.55	4.13	0.06	-0.55	3.92	0.15	-0.62
201K	7.13	0.14	-0.69	2.48	0.10	-0.68	2.17	0.01	-0.75
201L	6.18	0.21	-0.67	2.13	0.07	-0.66	1.97	0.05	-0.72

PROFILE 202 – LANTHANIDES

SAMPLE	La (ppm)	2σ	tLa	Ce (ppm)	2σ	tCe	Nd (ppm)	2σ	tNd
202B	50.26	1.074	0.00	114.9	1.45	0.00	58.44	0.916	0.00
202C	45.30	2.199	0.01	128.0	7.02	0.24	50.48	2.219	-0.04
202D	40.08	0.820	-0.16	112.4	3.73	0.03	53.69	1.112	-0.04
202E	33.51	4.857	-0.25	94.1	14.29	-0.08	48.63	7.210	-0.06
202F	34.49	2.073	-0.16	96.5	6.21	0.03	47.98	2.557	0.01
202G	35.77	2.305	-0.23	123.8	6.85	0.17	51.43	2.846	-0.04
202H	37.39	0.922	-0.39	143.9	6.64	0.03	50.85	1.603	-0.29
202I	3.84	0.184	-0.97	29.0	0.97	-0.91	12.84	0.648	-0.93
202J	9.33	0.300	-0.96	23.2	0.63	-0.96	8.64	0.454	-0.97

PROFILE 202 – LANTHANIDES (CONT'D)

SAMPLE	Sm (ppm)	2σ	tSm	Eu (ppm)	2σ	tEu	Yb (ppm)	2σ	tYb
202B	13.17	0.238	0.00	4.536	0.090	0.00	3.456	0.043	0.00
202C	11.30	0.527	-0.04	4.052	0.250	0.00	3.188	0.177	0.03
202D	12.58	0.208	0.00	4.170	0.106	-0.03	3.295	0.122	0.00
202E	11.12	1.605	-0.05	3.933	0.691	-0.02	3.018	0.389	-0.02
202F	10.93	0.842	0.02	3.806	0.274	0.03	2.905	0.151	0.03
202G	12.23	0.543	0.01	4.163	0.264	0.00	3.307	0.224	0.04
202H	12.75	0.380	-0.21	4.236	0.072	-0.23	3.703	0.110	-0.12
202I	4.08	0.220	-0.90	1.295	0.015	-0.90	1.710	0.058	-0.83
202J	2.05	0.075	-0.97	0.699	0.042	-0.97	0.936	0.051	-0.95

PROFILE 203 – LANTHANIDES

SAMPLE	La (ppm)	2σ	tLa	Ce (ppm)	2σ	tCe	Nd (ppm)	2σ	tNd
203A	36.78	0.576	0.03	119.7	3.49	0.48	51.40	0.732	-0.01
203B	35.71	1.522	-0.18	132.1	6.73	0.33	39.60	1.791	-0.37
203C	24.97	1.299	-0.41	119.0	6.66	0.24	31.76	1.352	-0.48
203D	13.05	0.325	-0.68	27.7	0.98	-0.71	18.70	1.135	-0.69
203E	18.69	0.990	-0.48	88.4	5.02	0.09	26.19	0.739	-0.49
203F	9.36	0.337	-0.83	139.3	3.68	0.13	14.50	0.768	-0.82
203G	7.23	0.206	-0.91	157.5	5.43	-0.15	9.66	0.463	-0.92

PROFILE 203 – LANTHANIDES (CONT'D)

SAMPLE	Sm (ppm)	2σ	tSm	Eu (ppm)	2σ	tEu	Yb (ppm)	2σ	tYb
203A	12.45	0.69	-0.08	4.058	0.067	-0.12	4.171	0.097	-0.19
203B	9.85	0.48	-0.41	3.230	0.220	-0.43	3.506	0.235	-0.44
203C	8.06	0.17	-0.50	2.621	0.183	-0.52	2.922	0.131	-0.52
203D	5.07	0.22	-0.68	1.655	0.102	-0.69	1.976	0.085	-0.67
203E	6.96	0.34	-0.49	2.141	0.119	-0.54	2.442	0.174	-0.53
203F	3.87	0.08	-0.81	1.194	0.007	-0.83	1.423	0.053	-0.82
203G	2.57	0.10	-0.92	0.818	0.029	-0.92	1.097	0.039	-0.91

PROFILE 201 – ACTINIDES

SAMPLE	Th (ppm)	2σ	tTh	U (ppm)	2σ	tU
201A	1.64	0.20	0.00	0.40	0.05	0.00
201B	1.62	0.09	0.19	0.39	0.03	0.18
201C	2.01	0.13	0.15	0.44	0.02	0.02
201D	4.55	0.13	0.14	1.34	0.06	0.37
201DBIS	1.73	0.04	-0.07	0.52	0.01	0.15
201E	3.63	0.12	0.18	1.00	0.05	0.33
201F	3.92	0.14	0.11	1.07	0.06	0.25
201G	4.46	0.07	0.06	1.34	0.02	0.31
201H	7.03	0.15	0.14	1.97	0.09	0.31
201I	8.38	0.32	0.24	2.67	0.07	0.62
201J	9.92	0.13	0.20	2.45	0.06	0.21
201K	6.43	0.04	-0.09	1.81	0.04	0.06
201L	5.09	0.15	-0.11	1.40	0.04	0.00

PROFILE 202– ACTINIDES

SAMPLE	Th (ppm)	2σ	tTh	U (ppm)	2σ	tU
202B	4.223	0.126	0.00	1.018	0.017	0.00
202C	3.810	0.251	0.01	0.827	0.063	-0.09
202D	4.126	0.149	0.03	0.916	0.020	-0.06
202E	3.710	0.615	-0.01	0.872	0.149	-0.04
202F	3.349	0.093	-0.02	0.800	0.042	-0.03
202G	3.826	0.199	-0.01	0.908	0.046	-0.03
202H	4.374	0.178	-0.15	1.144	0.027	-0.08
202I	10.776	0.346	-0.14	4.329	0.173	0.43
202J	9.343	0.255	-0.56	2.812	0.140	-0.44

PROFILE 203– ACTINIDES

SAMPLE	Th (ppm)	2σ	tTh	U (ppm)	2σ	tU
203A	4.203	0.181	0.00	0.792	0.032	-0.22
203B	5.446	0.205	0.06	1.489	0.019	0.19
203C	5.408	0.159	0.09	1.372	0.006	0.14
203D	5.022	0.220	0.03	2.689	0.120	1.27
203E	4.431	0.158	0.05	2.517	0.069	1.46
203F	6.945	0.246	0.09	1.881	0.039	0.21
203G	8.415	0.175	-0.12	2.161	0.085	-0.07

Appendix C: Mineralogy determined by XRD

XRD Results – Profile 201

Sample	% wt olivine	% wt pyroxene	% wt plagioclase	% wt K-feldspar	% wt gibbsite	% wt halloysite	% wt goethite	% wt illite + kaolinite	% wt ilmenite
201A	11	51	18	3.7	0.3	2	0	1	0
201B	22	37	14	1.4	4.8	1	0.5	2.7	4.8
201C	20	35	7.3	3.7	9.6	0.3	0.3	5.9	6.9
201D	12	7	6.3	0	46	6.8	4.3	3	0
201Dbis	18	37.1	15	0.9	11	1.5	1.1	2.7	4.8
201E	7.9	7.5	1.6	0	53	0.2	3.8	2.6	6.9
201F	4.4	5.3	1.7	0	64	0.2	2	2.2	6.7
201G	13	4.4	1.7	2.1	43	0.3	4	1	10
201H	15	4.5	4.5	6.9	20	1.4	4	15	3.9
201I	10	2.6	1.4	3.5	28	6.2	4.7	7.4	3.1
201J	1.3	8.2	31	2.6	24	11	1.5	0.3	0
201K	12	9.5	13	8.5	16	11	4.9	7.5	9.2
201L	6.7	8.8	11	5.5	15	4	6.7	6	5.3
average	12	16.9	9.9	3.0	26	3.6	2.9	4.5	5.6

XRD Results – Profile 202

Sample	% wt olivine	% wt pyroxene	% wt plagioclase	% wt K-feldspar	% wt gibbsite	% wt halloysite	% wt goethite	% wt illite + kaolinite	% wt ilmenite
202B	3.4	20	55	7	0	0.2	0	1.6	1.2
202C	5.3	20	47	10	0.2	5.1	0	1.8	2.2
202D	5.2	20	46	10	0	6.4	0.5	1.8	1.9
202E	5	24	48	4.9	0	2.2	0	2.1	2.2
202F	9.1	28	53	0	0.8	0.3	0.3	4.5	2.8
202G	9.4	28	33	6.6	0.5	1.7	1.1	4	3.2
202H	8.3	33	9.4	7.8	3.2	14.	4.7	5.5	5.3
202I	0.9	0.1	1.9	1.4	68	0.9	6	6.7	3.3
202J	1	0.3	16	12.4	9.7	24	6.3	11	7.3
average	5.3	19.7	34	6.7	9.2	6.2	2.1	4.3	3.3

XRD Results – Profile 203

Sample	% wt olivine	% wt pyroxene	% wt plagioclase	% wt K-feldspar	% wt gibbsite	% wt halloysite	% wt goethite	% wt illite + kaolinite	% wt ilmenite
203A	0.9	3.8	1.3	0	1.7	58	2.8	7.1	8.5
203B	6.5	4.8	0.9	0	31	38	4.6	7.5	5.1
203C	2.6	3.4	1.3	0	30	28	5.8	4.8	4
203D	5.5	4.9	2.2	0	33	27	7.2	5.2	5.4
203E	3.6	1.9	0.6	0.5	12	39	7.9	6.3	2.5
203F	4.4	1.8	1.7	0	22	39	8.4	10	4
203G	3.1	3.7	1.6	0	14	37	8.7	8.7	2.7
average	3.8	3.5	1.4	0.1	20	38	6.5	7.2	4.6

Appendix D: Dust-derived Th data

% Dust contribution – Profile 201

Sample	Th (ppm)	Nb (ppm)	Th/Nb	$f(Th_{dust})$ (%)	Sample	Th (ppm)	Zr (ppm)	Th/Zr	$f(Th_{dust})$ (%)
Average dust	**10.5**	**12**	**0.875**	n/a	**Average dust**	10.5	193	0.054	n/a
201A	1.643	14.77	0.111	n/a	**201A**	1.643	168.3	0.010	n/a
201B	1.623	12.25	0.132	**0**	**201B**	1.623	137.7	0.012	**0**
201C	2.010	15.75	0.128	**4.1**	**201C**	2.010	179.0	0.011	**4.1**
201D	4.549	36.03	0.126	**32.8**	**201D**	4.549	351.1	0.013	**32.8**
201Dbis	1.732	16.77	0.103	**1.0**	**201Dbis**	1.732	183.9	0.009	**1.0**
201E	3.633	27.74	0.131	**22.5**	**201E**	3.633	324.5	0.011	**22.5**
201F	3.924	31.68	0.124	**25.8**	**201F**	3.924	362.8	0.011	**25.8**
201G	4.459	37.82	0.118	**31.8**	**201G**	4.459	389.0	0.011	**31.8**
201H	7.033	55.38	0.127	**60.9**	**201H**	7.033	537.9	0.013	**60.9**
201I	8.377	60.82	0.138	**76.0**	**201I**	8.377	571.6	0.015	**76.0**
201J	9.918	74.52	0.133	**93.4**	**201J**	9.918	623.2	0.016	**93.4**
201K	6.429	63.35	0.101	**54.0**	**201K**	6.429	487.3	0.013	**54.0**
201L	5.091	51.50	0.099	**38.9**	**201L**	5.091	391.6	0.013	**38.9**

Appendix E: Cerium anomaly data

Cerium anomaly – Profile 201

Sample	Ce (ppm)	Nd (ppm)	La (ppm)	Ce/Ce*
Chondrite (Nakamura 1973)	0.87	0.63	0.33	n/a
201A	31.8	20.3	14.0	0.94
201B	27.4	17.4	11.5	0.98
201C	32.6	20.1	9.8	1.24
201D	98.9	28.4	10.8	3.09
201Dbis	43.8	22.1	13.6	1.29
201E	150.7	19.0	7.4	6.95
201F	107.8	16.8	4.8	6.73
201G	68.0	17.3	4.7	4.20
201H	111.8	35.5	9.8	3.34
201I	187.3	40.3	16.0	4.02
201J	126.0	45.7	20.4	2.22
201K	76.6	28.3	22.4	1.47
201L	76.1	24.6	19.8	1.66

Cerium anomaly – Profile 202

Sample	Ce (ppm)	Nd (ppm)	La (ppm)	Ce/Ce*
Chondrite (Nakamura 1973)	0.87	0.63	0.33	n/a
202B	114.9	58.4	50.3	1.00
202C	128.0	50.5	45.3	1.25
202D	112.4	53.7	40.1	1.19
202E	94.1	48.6	33.5	1.16
202F	96.5	48.0	34.5	1.17
202G	123.8	51.4	35.8	1.44
202H	143.9	50.9	37.4	1.62
202I	29.0	12.8	3.8	2.30
202J	23.2	8.6	9.3	1.14

Cerium anomaly – Profile 203

Sample	Ce (ppm)	Nd (ppm)	La (ppm)	Ce/Ce*
Chondrite (Nakamura 1973)	0.87	0.63	0.33	n/a
203A	119.7	51.4	36.8	1.36
203B	132.1	39.6	35.7	1.64
203C	119.0	31.8	25.0	2.04
203D	27.7	18.7	13.1	0.88
203E	88.4	26.2	18.7	1.97
203F	139.3	14.5	9.4	6.05
203G	157.5	9.7	7.2	9.22